Multiwavelength Polarimetry of Astrophysical Sources

A thesis submitted in partial fulfilment of

the requirements for the degree of

Doctor of Philosophy

by

Aarthy E

(Roll No. 15330005)

Under the guidance of

Prof. Santosh V. Vadawale

Astronomy and Astrophysics Division

Physical Research Laboratory, Ahmedabad, India.

DEPARTMENT OF PHYSICS

INDIAN INSTITUTE OF TECHNOLOGY GANDHINAGAR

2020

to

My Family and Friends

Declaration

I, Aarthy E, declare that this written submission represents my ideas in my own words and where others' ideas or words have been included, I have adequately cited and referenced the original sources. I also declare that I have adhered to all principles of academic honesty and integrity and have not misrepresented or fabricated or falsified any idea/data/fact/source in my submission. I understand that any violation of the above can cause disciplinary action by the institute and can also evoke penal action from the sources which have thus not been properly cited or from whom proper permission has not been taken when needed.

(Signature)

(Name: Aarthy E)

(Roll No: 15330005)

Date:

Department of Physics
Indian Institute of Technology Gandhinagar
Gandhinagar, Gujarat-382355

Certificate

It is certified that the work contained in the thesis entitled “Multiwavelength Polarimetry of Astrophysical Sources” by Ms. Aarthy E (Roll no 15330005), has been carried out under my supervision and that this work has not been submitted elsewhere for any degree or diploma

(Santosh V Vadawale)
Thesis Supervisor
Professor
Astronomy & Astrophysics Division
Physical Research Laboratory
Unit of Department of Space, Govt of India
Ahmedabad-380009, Gujarat, India.

Acknowledgments

My five years long PhD journey is coming to an end and I feel overwhelmed to comprise my hard work in this dissertation. I remember the words from my supervisor, that he told me five years back "PhD is not just a degree.. its a process.. over this process you grow.. as a researcher and as a person.." I am happy to take this space to thank the people with out whom successful completion of this thesis wouldn't be possible.

First and foremost I express my deepest sense of gratitude to my thesis supervisor Prof. Santosh V. Vadawale for his constant guidance throughout my PhD journey. Santosh, you truly are a source of inspiration for me and over the past years you have been a pillar of support. The support I received from you is invaluable and I can't thank you enough for your open minded guidance which led me to explore a wide range of problems in my PhD. My special thanks to you for constantly encouraging me every single time when I lost confidence in myself. I sincerely thank my Doctoral Studies Committee members, Prof. K. S. Baliyan (former Chairman, A&A) and Dr. Shashikiran Ganesh for constantly monitoring my progress every semester. Baliyanji, your constant encouragement and valuable inputs were driving forces during my hardships. Your friendly nature and care were of great backing and my heartfelt thanks to you for being constantly supportive. Apart from being a DSC member, Dr. Shashikiran Ganesh rendered his valuable time in guiding me throughout the infrared part of my thesis work. Shashi, I always look up to you for your level of patience and persistence. Right from making the instrument, through all observation nights, till we reported the results you were available round the clock. Your passion towards the work with extremely calm nature have always amazed me. I will treasure all of those Mt Abu memories where I got to learn the sky and the instruments from you. I sincerely thank you for being such a great mentor.

I take this opportunity to thank the great amount help I received from PRL. I am thankful to the Department Of Space, Govt. of India for providing me the research grant during my tenure at PRL. I thank the current director Prof. Anil Bharadwaj and former directors Prof. Utpal Sarkar, Shri. Tapan Mishra for their support in rendering the best research facilities. I would like to thank Prof. Pallamraju, Dean PRL and Prof. Janardhan, former Dean PRL for their support in my thesis work. I express my sincere thanks to Prof. Ramachandran, former Academic committee Chairman, and all the former and current members of the Academic committee for their help and guidance in my thesis work. I thank Prof. S. V. S. Murthy, former Chairman of PLANEX for providing me the first opportunity to join as a Project Associate at PRL and sowed the seed for my research interest. I thank Prof. Abhijit Chakraborty, Chairman of A&A for his support in carrying out my research work in the division. My sincere thanks to all the current and former faculties of the A&A division: Prof. N. M. Ashok, Prof. A. K. Singhal, Prof. Sachindra Naik, Dr. Mudit Srivastava, Dr. Aveek Sarkar, Dr. Manash Samal, Dr. Veeresh Singh, Dr. Lokesh Dewangan, Dr. Arvind Rajpurohit, Dr. Vishal Joshi and Dr. Venkatraman for all technical discussions and valuable inputs. I sincerely thank all the former and current students of A&A division: Dr. Tanmoy, Dr. Priyanka, Dr. Shweta, Dr. Anjali, Dr. Gaurav, Dr. Navpreet, Dr. Kumar, Dr. Prahlad, Dr. Nilkant, Archita, Shivangi, Sandeep, Somdutta, Biswa, Aravind, Shanwlee, Neeraj, Vipin, Abhijit, Abhay, Sushant, Akanksha, Namita, Naval for all the scientific interactions and student discussions that helped in my thesis work.

I feel privileged to receive great technical support from both PRL and TIFR. I thank all the staffs at the Mt. Abu Infrared Observatory, PRL: Mathurji, Rajeshji, Patwalji, Jainji, Nafees bhaiya and all the other technical staffs and Engineers who work tremendously hard for the smooth functioning of the observatory. I am so grateful to the telescope operational trainees, Prashanth and Mukesh for their enthusiasm and sincerity during all observations. I thank Shri. Jigar Raval for his support in using the Vikram-100 HPC facility where all the simulations included in the thesis are performed. I thank Dr. Nishtha and all other library staffs and trainees for their helpful and approachable nature in procuring books and other facilities from the PRL Library. My special thanks to Dr. Alam and Pragya for their very positive, supportive, and friendly encouragement. I thank Mr. A. P. K. Kutty, Hingarji, Patilji, Dediaji from TIFR for providing all necessary equipment to successfully perform experiments at TIFR. I thank the employees of both PRL and TIFR workshops for their invaluable help in making necessary parts for my experiments.

I am sincerely thankful to the entire CZTI team for providing me the opportunity to work on one of the prestigious projects. I had the privilege to work with one of the coolest team ever, where the second generation is super quick and efficient and we had extreme fun working together under our first generation experts. I thank Prof. A. R. Rao, TIFR for being a god father and who guides many of us with enthusiasm. Prof. Rao, your energy and passion are so contagious. I will forever remember the days I spent at TIFR performing experiments with CZTI, which would not have been possible without you taking a chance and having hope on me. You are one of the reasons I could pursue research and I would always count on you as a mentor professionally and personally. There are occasions when I did not get an accommodation at TIFR guest house and you never hesitated to provide accommodation at your house. Thank you for being such a strong base that holds the entire CZTI team. I thank Prof. Dipankar

Bhattacharya, IUCAA and Dr. Varun Bhalerao, IITB for their constant support and guidance. I thank my senior Dr. Tanmoy Chattopadhyay, who created a way in which I could easily walk. Tanmoy, you are one of the brilliant minds I have ever seen. You were such a fantastic guide, and in a short time you could transfer your knowledge to me before you left PRL. Working with you is genuinely the best part of my PhD and it is not an exaggeration if I say, whatever I would do in my thesis you laid the foundation for those in my first year of PhD. I thank my dear colleague N. P. S. Mithun for being the smartest and quickest person to work with. Mithun, we might have worked and grown together but I am the one who got a lot more benefited by learning so much from you. Your knowledge and support are invaluable. Nilam, Sudip, Sujay, Ajay Ratheesh, Ajay Vibhuthe, Vidushi I will cherish the fun we had during all the projects we worked together.

The people and friendship I acquired here became family over time. I thank two special people Archita and Subir for being the best friends one could ever get and were there for me and with me in thick and thin. I will always carry those good life discussions we had and memories we shared. You both play a major role for me being sane till now. I thank the crazy batch of JRF 2015: Rahul, Randeep, Nidhi, Shefali, Varun, Shivangi, Kaustav, Richa, Akanksha, Balbeer, Ashish, Harsh Oza, Harsh Raj, Naman, Arvind. I thank each one of you for all the happiness and fun. I thank my seniors: Arko, Monojit, Deepak, Dipti, Bhavya, Ikshu, Kuldeep, Satish, Jabir, Rupa, Rukmani, Ali, Chandan, Vishnu, Nijil, Anil, Niharika, Kiran for being very supportive and encouraging. Over the course of time in PRL, hostel became our home. I thank Mrs. Richa Prashant Kumar for providing the best hostel facility and all the canteen staffs who took care of our health by serving healthy meals. I thank my juniors: Deepika, Nisha, Sushree, Harish, Priyank, Abdur, Ayan, Surendra, Anshika, Ritu, Shivani, Hrushi, Ankit, Alka, Sana, Partha, Subith, Satya, Madhu who made my life at thaltej hostel more lively. There are few special people who provided home away from home: Shweta di, Prof. Gautam Samantha & Ms. Moumita, Dr. Arvind Singh & Pallavi bhabhi, Dr. Rajesh & Nisha bhabhi, Shreya, Abi mam, Gayatri, Nilam mam, Devyani, Arohi, I thank you all for being so warm and welcoming. I thank all my bros: Prasad, JK, Neeraj, Chandan, Rishi, Aaditya, Kapil, Mohan, Prashanth, Srirag, Shekar, Prabodh, Amogh, Nishant, Anil for being great partners in crime and available for plans made at anytime. I also thank my friends Utkarsh, Vaibhav, Sonam, Sanjeev, Deekshya, Ankita, Vaishnav, Prachi, and Nandita. I thank my friends since my PAship Ami, Indhu, Mani Teja, Arpit bhaiya, Shyamal, Ragav, Balaji for all the good times spent together.

Pursuing and completing a PhD would not have been possible without a family as a backbone. I thank my parents Esakkiappan and Bagavathy for believing in me, and encouraging me to achieve from behind the stage. Amma, appa I can not thank you enough for the amazing life you have given me and I am forever indebted to both of you. I thank my brother Dr. Somasundaram who is my role model to pursue PhD. Anna I admired you all my life and having an inspiration like you closer, played a major role for me to take up research. You were there for me in hardships and I will always be thankful to you. I thank my brother Gomesh, who was there for me at any situation. You are one of the people who is so proud of me no matter what, and I cant even attempt to thank you for the support you give me. I thank my lovely cousins Dhivya, Anu, Pooja, Chithraa, Akshaya, Karthik, Vivek who were so supportive during my PhD. More than cousins you guys were siblings and best friends. I thank my forever best friend Ida for rendering her shoulders even before she knew my problems. Subha anna and Joel anna thank you so much for being so supportive all these years. Thank

you Robin and Kalai for being my younger brothers more than my college juniors. I am so thankful to my to be parents in laws, Mama and Athai you welcomed me at a very critical point in my life and have been supportive and encouraging at every step. Varun, Divya, Priya, Ramya you guys have showered me with love and care and my special thanks to you guys for being so supportive. Last but not the least I would like to thank you *Arun*, for being a ray of hope in dark times and for being there with me throughout the time when I wrote this thesis.

At last, I would like to thank each and everyone who helped me and supported me through this five years long PhD journey.

Abstract

Polarization measurements of astrophysical sources could help in understanding phenomena that can not be distinguished only through imaging, timing and, spectroscopy. Measuring polarization of the source over various regimes of the electromagnetic spectrum could address the nature of source geometry, emission mechanism behind the origin of photons, and magnetic field. Since polarization is not a directly measurable quantity, special components/techniques are needed to the measure polarization of any astrophysical source. In general, polarization measurement requires a large number of source photons. This makes measurement of polarization highly challenging, particularly in X-ray regime since X-ray instruments are space-borne. Polarization measurements in X-rays are achieved by measuring the modulation amplitude, which is the histogram of detected counts at various azimuthal scattering angles.

The importance of polarimetry was realized in the early stages of X-ray astronomy and there were several attempts to perform polarimetry through rocket-based experiments. The first dedicated space-based polarimeter is a Bragg polarimeter onboard OSO-8 which reported the first reliable polarization measurement of Crab in soft X-ray band. Since then, over the past five decades, there has been no dedicated space-based X-ray polarimeter. Though there have been attempts to measure polarization through balloon-borne instruments, they have a disadvantage in limited exposure time. In the absence of dedicated polarimeters, there have been constant attempts to use the polarization capability of spectroscopic instruments. The modulation amplitude which gives the polarization fraction is a positive definite quantity. Hence, in case of low signal to noise, there are chances to measure definite polarization fraction even if the incident radiation is unpolarized. Hence it is important to experimentally verify the performance

of a polarimeter with unpolarized X-rays. Major problems with utilizing imaging/spectroscopic instruments to do polarimetry is that they were not optimized experimentally for polarization measurements. Due to this reason, there are apprehensions in the scientific community to accept the results obtained from those instruments.

Cadmium Zinc Telluride Imager (CZTI), which is one of the payloads onboard India's first multiwavelength astronomical satellite AstroSat is one such imaging & spectroscopic instrument that could be optimized to perform polarimetry. Primary objective of CZTI is to perform imaging and spectroscopy over an energy range of 20 – 150 keV. The instrument employs pixelated CZT detectors that could be used to measure polarization. A major advantage of CZTI is that its polarimetric capability was experimentally demonstrated before launch using both unpolarized and polarized X-rays.

AstroSat was launched in September 2015, and post-launch CZTI was used to measure hard X-ray polarization of Crab pulsar and nebula, which is a standard candle in X-ray astronomy. While the hard X-ray (/soft gamma-ray) polarization of Crab was reported earlier (by INTEGRAL), the major advancement provided by CZTI is that it could measure polarization as a function of the pulse phase. Using Crab data obtained by CZTI over one year its operation, Vadawale et al 2018 (V18) showed a clear swing in polarization in the off-pulse region and the polarization properties are found to be different at two peaks of Crab. In addition to the data used in V18, CZTI has acquired Crab data over multiple observations. Here, we use this data to confirm the phase dependent signatures and also carry energy resolved phase dependent polarization analysis. Over the past 4 years of operation, Crab has been observed for $\sim 1800ks$ over multiple observations by CZTI out of which the results of $\sim 800ks$ data was reported in V18. Following up the work of V18, we perform phase resolved polarization analysis over 100 – 380 keV using ∼1800 ks of CZTI Crab data observed over 4 years. The phase integrated and phase resolved polarization results over 100 – 380 keV are consistent with those reported by V18 with a better statistical significance. We obtain PF, PA of 33.4±4.1%, 143.6±1.7° at 8.1σ for Crab and 35.2±7.4%, 144.2±3.0° at 4.7σ for the off-pulse region. It is to be noted that, so far these are the results with the best statistical significance. Further, we extended the work by analyzing polarization over multiple energy ranges. A method of dynamic binning in energy, dividing the total energy range 100 – 380 keV into bins of 70 keV with a sliding window of 10 keV is performed for the first time. We obtained interesting results which show energy dependence in the polarization at both the peaks, bridge, and off-pulse region.

The polarization measurement of Crab in hard X-rays using CZTI prompted two branches of possibilities. First is to use CZTI to the measure polarization of other hard X-ray bright sources. The second is to probe the possibility of performing multiwavelength polarimetry of Crab.

Besides observing persistent sources like Crab, CZTI is also a prolific Gamma-Ray Burst (GRB) detector. This provides an opportunity to utilize CZTI to perform polarization of GRBs in hard X-ray regime. One advantage of GRB polarization using CZTI compared to Crab is the high signal to noise ratio, resulting in better sensitivity. However, a drawback is that GRBs are randomly distributed in space and time and they last for a very short time (fractions of seconds to few seconds). Hence in general Monte Carlo simulations are essential in GRB polarization analysis. We developed the AstroSat Mass model using Geant4 to perform required simulations for CZTI GRB polarimetry. CZTI detected 47 GRBs between October 2015 to October 2016 out of which we report polarization of 11 bright GRBs.

A statistical study on GRB polarization could help in understanding the emission mechanism behind GRB prompt emission and the nature of the magnetic field along the jet. This demands precise polarization measurement of a large number of GRBs. Hence, CZTI, which measured polarization of 11 GRBs detected over a year is of great importance to the GRB polarimetry community. However, one caveat is that the polarimetric capability of CZTI for off-axis sources is not experimentally demonstrated. Experimental confirmation of CZTI to be used to perform polarimetry in case of pointed observations is the factor that makes CZTI unique from other non-optimized polarimeters. However, experimental confirmation for such capability is not available for non-dedicated GRB polarimeters including CZTI. In this context, we performed controlled experiments using CZT detector and complemented the experimental results with extensive Geant4 simulations. Our results show that CZTI can be used to measure the polarization of bright GRBs up to the off-axis angle of $\sim 60^{o}$.

With firm polarization measurements of Crab in X-rays, we explored the possibility of measuring Crab polarization in other wavebands. Although polarization reports of Crab are available in radio, optical, X-rays/Gamma-rays, interestingly no such report of polarization exists in the infrared regime. The Mount Abu Infrared Observatory (MIRO), is one of the facilities of Physical Research Laboratory (PRL) that has a 1.2 m Cassegrain f/13 telescope and various optical and infrared back end instruments. The Near Infrared Camera and Spectrograph (NICS) is a workhorse instrument which is capable of doing imaging and spectroscopy in the near IR regime. The accessibility of MIRO and NICS provided the motivation to explore the possibility of measuring the near IR polarization of Crab. We added imaging polarimetric capability to NICS (NICSPol) by mounting a rotating wire grid polarizer between the telescope optics and NICS. NICSPol covers a wavelength range of 0.8 to 2.5 μm over H, J and Ks bands. We verified the performance of NICSPol by observing a set of polarized and unpolarized standards. The results show that NICSPol can constrain polarization within $\sim$1% for sources brighter than $\sim$16 magnitude in JHKs bands. NICSPol is the only imaging IR polarimeter in India and would provide a fantastic opportunity to do simultaneous polarimetry of various astrophysical objects over a wide range of EM spectrum.

In a nutshell, we performed energy dependent polarization of Crab using AstroSat CZTI data with respect to the pulse phase. We obtained Crab polarization results with the best statistical significance so far in the hard X-ray regime. Apart from persistent sources like Crab, CZTI also serves as a good GRB detector. Hence we performed polarimetry of GRBs detected by CZTI over a year and obtained polarization of 11 bright GRBs with good statistical significance. The GRB polarization results using CZTI are promising, but to enhance the credibility of these measurements we carried out controlled experiments and simulations with polarized and unpolarized incident X-rays to validate the off-axis polarimetric capability of CZT detectors. This ensures that pixelated CZT detectors could be used to perform GRB polarimetry. These works which comprise the thesis have resulted in significant advancement in the field of astrophysical polarimetry. By achieving the hard X-ray polarization of Crab we explored the possibility to measure polarization of Crab in the infrared regime by developing NICSPol, as an add-on to NICS at MIRO, PRL. Currently, NICSPol is the only imaging infrared polarimeter in India.

Keywords: X-ray polarimetry, Cadmium Zinc Telluride Imager (CZTI), Crab, Gamma-ray bursts (GRB), infrared polarimetry, Geant4, instrumentation.

Contents

List of Figures

List of Tables

Chapter 1

Introduction

The field of observational astronomy involves the collection of electromagnetic radiation from various astrophysical sources. The analysis of the acquired photons could be performed using three most popular and commonly used techniques: 1) Spectroscopic analysis - radiation in the energy (or wavelength) domain 2) Timing analysis - radiation in time domain 3) Imaging analysis - radiation in the space domain. There is a fourth comparatively less explored but important tool: polarimetry. Polarization is an inherent property of electromagnetic radiation which indicates the dominant orientation of the electric (& magnetic) field vector. Polarimetry gives two additional parameters: polarization angle (PA) and degree of polarization (DoP/polarization fraction PF). PF is the fraction at which the incident radiation from the source is polarized, that is, the fraction of polarized intensity in the total intensity. When the source exhibits a finite polarization fraction, then the preferred orientation of the plane in which the electric vector oscillates, as it propagates, with respect to a reference direction (in sky plane typically with respect to celestial north) is the polarization angle. In general, astronomical sources are expected to be unpolarized unless there exists some asymmetry and/or anisotropy either in terms of matter or field, in the source or along the path of propagation of the photons. Hence measuring polarization helps in studying the magnetic field and geometry of various astrophysical sources and their surrounding medium. Despite these obvious advantages, polarimetry is relatively less popular compared to spectroscopy and imaging due to certain inherent complexities. The prime reason is that most of the sources possess very low polarization (a few %) and hence longer exposure times are needed compared to spectroscopy.

The origin of polarization differs over different parts of the electromagnetic spectrum. In radio regime polarization is due to synchrotron radiation. Polarization in UV, optical and IR arise due to scattering by dust grains and magnetic field that orients the dust grains. Non-thermal radiation from different sources is also polarized. Optical polarization in various astrophysical sources could also partly arise due to the synchrotron process. In X-ray regime depending on the photon energy, geometry, and magnetic field, polarization could arise due to scattering (Rayleigh, inverse Compton), cyclotron, synchrotron, [1] or due to more exotic physical processes like vacuum polarization and birefringence through extreme magnetic fields [2, 3]. Assuming the initial radiation from the internal structure of the source to be unpolarized, measuring polarization could help in understanding the point of interactions which polarizes it. The study of polarization induced by scattering is a powerful technique to understand the intervening matter and field distribution, when the original radiation is expected to be unpolarized (e.g. thermal radiation).

The work done in the thesis involves instrumentation, detailed simulations, experimental validation of polarimetric efficiency, and polarization measurement of astrophysical targets: 1) the Crab pulsar and Nebula and 2) Gamma-Ray Bursts. In section 1.1 the two astrophysical sources of interest in the thesis are discussed briefly. Section 1.2 describes the basics of X-ray polarimetry briefing the techniques involved at different energy ranges. Section 1.3 discusses about Cadmium Zinc Telluride Imager (CZTI), a hard X-ray polarimeter onboard AstroSat followed by an overview 1.4 of the thesis.

1.1 Astrophysical targets

In this section, we provide a brief introduction of two types of sources: Pulsar and pulsar wind nebula (in particular Crab) and Gamma-ray bursts for which polarization studies are performed in the thesis. These sources are extensively studied over decades, however, there are many open-ended questions that need further theoretical and observational developments. Few of these unsolved issues for which measurement of polarization (particularly in the X-ray regime) could give more insights are described in the following subsections.

1.1.1 Crab Pulsar and Nebula

The Crab pulsar and its nebula (Crab in general) is the remnant of the popular supernova event that happened in 1054 A.D. Crab, which is a Pulsar Wind Nebula (PWN) is the first source that was listed in Charles Messier's catalog (M1). Review articles by Hester 2008 [4] and B*ü*hler and Blandford 2014 [5] are excellent sources that cover the existing knowledge of Crab. The Crab nebula is roughly an ellipsoidal volume with a major axis of 4.4 pc and a minor axis of 2.9 pc and is ∼2 kpc beyond the solar system. The Crab could be broadly divided into four components: 1) An isolated ∼10 km radius rotation powered pulsar, which has a pulse period of ∼33 ms and a spin-down luminosity of 5×10^{38} erg s^{-1}, 2) The synchrotron nebula with features like wisps and knot, 3) thermal gas with features called filaments, and 4) freely expanding supernova remnant. Figure 1.1a shows the composite of images obtained in radio, optical, and X-ray regimes from Chandra X-ray telescope, Hubble Space Telescope (HST), and Very Large Array (VLA) respectively. The pulsar emission is bright in X-rays, the synchrotron emission could be seen both in X-rays and in optical, the thermal gas is bright in optical and infrared, while the faintly expanding supernova remnant could be seen in radio regime. The pulse profile of Crab is a double peak structure that is termed as the main pulse and the intermediate pulse. The pulse phases are aligned throughout the electromagnetic spectrum, while from figure 1.1b it could be seen that the amplitude of peaks varies with respect to the energy of incident photons.

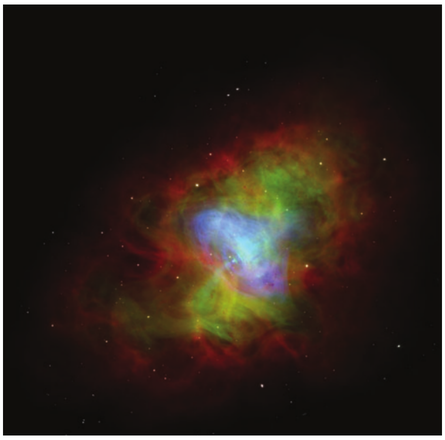

(a)

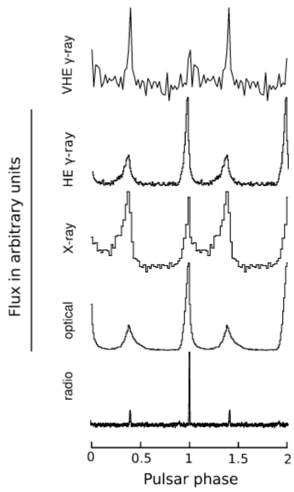

(b)

Figure 1.1: (a) A false color composite image of Crab using data from Chandra (X-ray) in blue, HST (optical) in green, and VLA (radio) in red. Credits: Hester 2008 [4] and (b) Pulse profiles for radio (1.4 GHz), optical (1.5 – 3.5 eV), X-ray (100 – 200 keV), HE gamma-ray (100 – 300 MeV) and VHE (50 – 400 GeV) gamma-ray energies. Credits: B*ü*hler and Blandford 2014 [5].

The Crab has been studied observationally over the entire electromagnetic spectrum and is one of the few X-ray bright sources. The flux of Crab is constant over a specific energy range and the intensity of X-ray sources are commonly measured in terms of Crab units. [1] The spectral and timing properties of Crab are quite steady and being a standard candle, observations of Crab are used to perform onboard calibration of X-ray instruments. Crab was the first pulsar for which imaging photometry and imaging polarimetry were reported in optical wavelengths. The first-ever X-ray polarization measurement was reported for Crab by Weisskopf et al 1978 [6] using a Bragg polarimeter onboard Orbiting Solar Observatory - 8 (OSO-8). However, over the past years, there has been no dedicated space-based X-ray polarimeters. There have been various attempts to measure the polarization of Crab in X-rays using instruments onboard INTEGRAL, RHESSI, PoGO+ and the results obtained are discussed in section 2.1.

Even after 50 years of pulsar observations, with improvements in imaging, timing, spectroscopy, the point of origin and the emission mechanism(s) behind the gamma photons itself are not known yet. There are various models such as: polar cap [7, 8], outer gap [9], slot gap [10], two-pole caustic [11], and stripped wind [12, 13] predict the origin of the high energy photons from rotation powered pulsars. A major disadvantage is that multiple models are compatible with the observed Crab pulse profile and spectra. The polar cap, outer gap, and slot gap models predict the origin of emission inside the light cylinder while the stripped wind model predicts the emission to originate outside the light cylinder. The intrinsic polarization predictions depend on the emission mechanism responsible for the origin of the photons. One distinguishing feature of these models which could provide additional information is their phase-dependent polarization signa-

[1] A Crab unit is 2.4×10^{-8} erg cm^{-2} s^{-1} over 2 – 10 keV.

ture. All of these models involve unknown parameters such as the viewing angle, inclination angle, pitch angle, and light cylinder radius. Figure 1.2 shows the polarization predictions with respect to pulse phase for optical and gamma-ray regimes obtained for two different light cylinder radii: r = 0.7 – 1.3 R_{LC} and 1.3 – 2.0 R_{LC} each for three cases inclination angles: α = 45°, 60°, 75°. The viewing angle in all the cases is assumed to be ζ = 70° and the particle pitch angle is assumed to be ψ = 0.01 . From this figure it could be seen that even a minor change in one of the various parameters in the models would result in different polarization predictions [14].

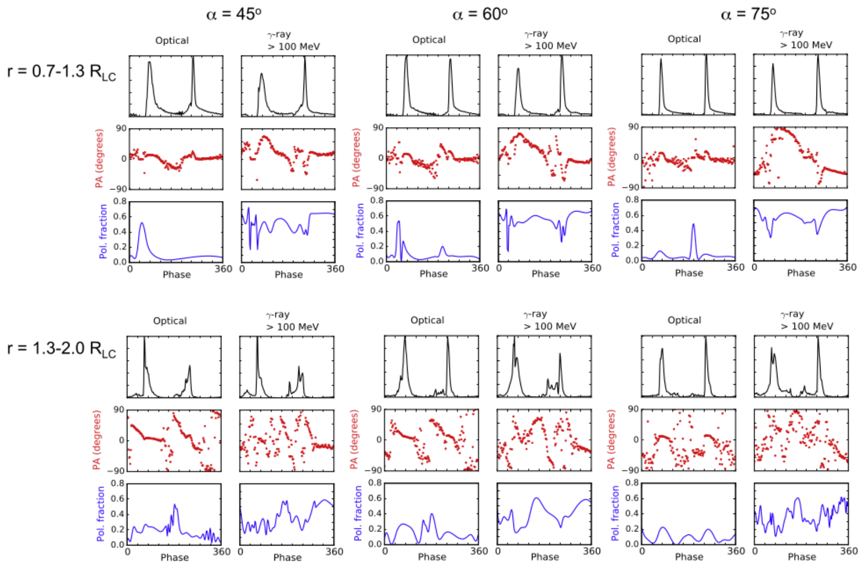

Figure 1.2: The figure shows the pulse profile with the predicted polarization fraction and polarization angle over optical and gamma-ray regime for inclination angles: α = 45°, 60°, 75° each for two different light cylinder radii: r = 0.7 – 1.3 R_{LC} and 1.3 – 2.0 R_{LC}. The viewing angle in all the cases is assumed to be ζ = 70° and the particle pitch angle is assumed to be ψ = 0.01. Credits: Harding et al 2017 [14].

Measurements of Crab polarization from optical to gamma have been reported by various ground and space-based instruments [6, 15, 16, 17, 18, 19]. Slowikowska et al 2009 [20] reported phase resolved polarization of Crab in the optical regime using data from Optical Pulsar Timing Analyzer (OPTIMA) mounted at 2.56 m

Nordic Optical Telescope. This report leads to development in theoretical predictions of phase resolved polarization [12, 13] based on the above mentioned models. Though stripped wind and slot gap models matched the trend of optical observation, the predictions did not consider energy dependence. Harding et al 2017 [14] is the only report in which phase resolved polarization of rotation powered pulsars are predicted from optical to gamma regimes. The development of theoretical models based on observed results emphasize the need for more accurate phase resolved polarization measurements over a wide range of the electromagnetic spectrum. Apart from the optical report [20], there were no other reports on phase resolved polarization till Vadawale et al 2018 (V18) [21]. V18, for the first time, not only reported phase resolved polarization in X-rays but also showed significantly strong variation in PF and PA in the off pulse region. They showed that the phase resolved polarization behavior for the main pulse in hard X-rays are similar to the optical polarization results [20], but for the intermediate peak, the results show an opposite trend in comparison with the optical regime. These imply the importance to develop energy dependent theoretical models along with a more accurate phase resolved polarization measurements over the entire electromagnetic spectrum.

1.1.2 Gamma-Ray Bursts

Gamma-ray bursts (GRBs in general) are the most powerful events observed in the universe, releasing energy in the order of $\sim 10^{53}$ erg in the gamma regime. GRBs were accidentally discovered during the early 1970s by Vela satellites which carried gamma-ray, X-ray, and neutron detectors and were meant to monitor whether any nuclear weapon test was carried out in outer space. Since its discovery, between 1973 – 1991 hundreds of theories were developed to explain the origin of GRBs. In the year 1991, Compton Gamma Ray Observatory (CGRO) was launched which carried the Burst And Transient Source Experiment (BATSE) as one of the payloads [22]. BATSE detected ∼2700 GRBs along with localizing their positions in the sky through which the GRBs were found to be isotropically distributed in the sky 1.3a. Hence BATSE ruled out the galactic origin of GRBs and proved its cosmological origin.

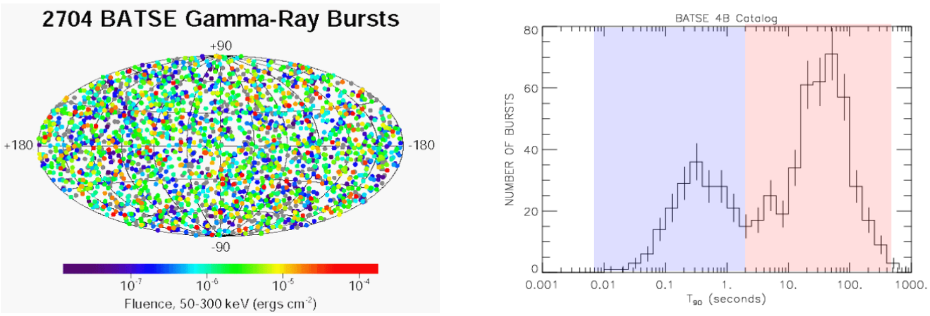

(a) (b)

Figure 1.3: (a) Isotropic distribution of BATSE GRBs in sky co ordinates Credits: G. Fishman et al., BATSE, CGRO, NASA (b) Histogram of T_{90} of BATSE GRBs with a minimum ∼2 s clearly distinguishing short and long GRBs. Credits: Kouveliotou et al 1993 [23].

The duration over which the GRB occurs is defined by the term T_{90} which is the time interval over which 90% of the source counts are observed. The histogram of T_{90} of BATSE GRBs shown in figure 1.3b represents two types based on the GRB duration: short (T_{90}<2s) and long (T_{90}>2s) GRBs. The progenitors of the short and long GRBs are different. It is now known that short GRBs occur when two compact stellar binaries merge [25, 26] and long GRBs occur during the core collapse of massive stars [27, 28, 29]. In both the cases, a black hole with an accretion disk is formed with oppositely directed jets launched from the proximity of black hole. GRB emission occurs in two distinct phases: the prompt emission and the afterglow. The initial burst of high-energy emission or the prompt emission is widely believed to originate from a jet close to the black hole, while the long-lasting multi-wavelength afterglow emission is generated far

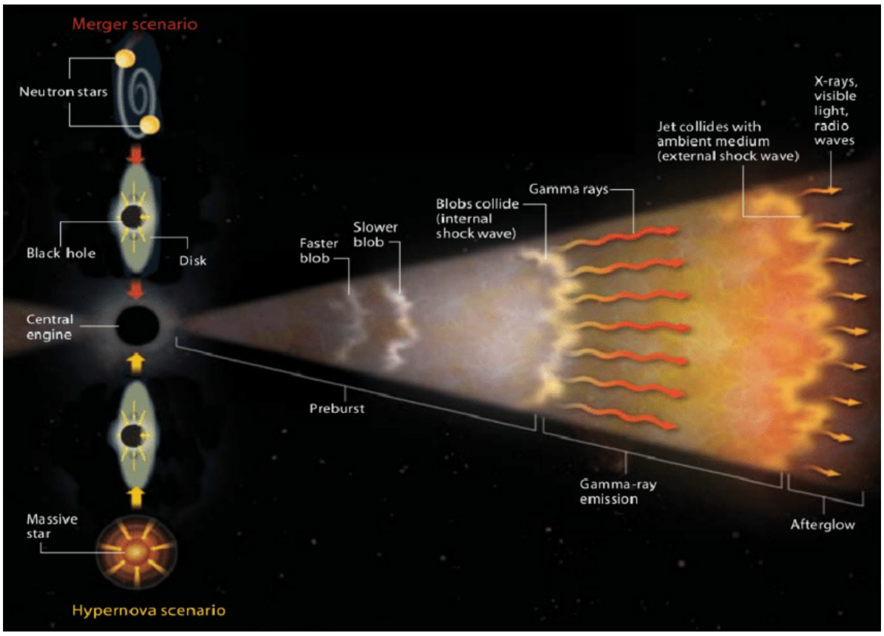

Figure 1.4: The figure represents the fireball model that explains both the merger and collapse scenario. The jet launched closer to the black hole emits high energy photons (gamma/hard X-rays) during prompt emission which interacts with the ambient medium for the afterglow emission from soft X-rays to radio. Credits: Gehrels et al 2002 [24].

from the compact object by the interaction of the GRB jet with the circumstellar medium [30, 31]. Figure 1.4 represents the widely accepted fireball model that explains the prompt emission due to internal shocks and afterglow emission due to external shocks when jet collides with the ambient medium.

Over the past 4 decades, observational study of GRBs has grown tremendously with the advent of several missions like CGRO/BATSE, Neil Gehrels Swift Observatory, Fermi, etc and other ground-based observatories. The afterglow phase of GRBs is well studied by timing and spectroscopy. Despite observing a large number of GRBs with sensitive detectors onboard Swift [32, 33] and Fermi [34] missions, the mechanism of the prompt emission has not yet been well understood [35] owing to the diversity, extreme variability, and very short duration of this prompt phase [36, 37]. The prompt emission is believed to be generated either by synchrotron process [38, 39] or through inverse Compton scattering [40, 41, 42].

Besides, a few cases display the evidence of a thermal black body component, presumably of photospheric origin [43, 44, 45, 46]. One way of distinguishing between these emission processes would be through their unique polarization signatures. Toma et al 2008 [47] simulated around 10,000 GRBs and reported that the degeneracies in geometry and the radiation process could be critically constrained by measuring the polarization of a large number of GRBs and statistically studying the measured polarization fraction with respect to the ratio between the number of GRBs with polarization measurement to the total number of GRBs detected [47]. This emphasizes that the measurement of X-ray and Gamma-ray polarization is of great importance in the study of GRB prompt emission [48, 49].

1.2 X-ray Polarimetry

Uhuru, the first X-ray astronomical satellite was launched in 1970. Since then X-ray astronomy has grown tremendously over the past five decades, with improvements in imaging, spectroscopy, and timing sensitivities comparable to those at other wavelengths. Along with these three techniques, the importance of X-ray polarimetry was realized decades back and there were attempts for rocket-borne or early satellite-borne polarization experiments. Performing polarization in X-rays is highly challenging because it requires a large number of photons which ends up in poor detector sensitivity. Over time the improvement in sensitivity for spectroscopy and imaging was significant and hence those techniques were given more prominence. Hence, the field of X-ray polarimetry is still largely unexplored due to the inherent complexities in measuring X-ray polarization [50]. Despite the scientific importance of X-ray polarimetry [51], there have been very a few dedicated X-ray polarimeters since the first reliable measurement of the X-ray polarization of the Crab nebula at 2.6 and 5.2 keV by OSO-8 [6]. Apart from the balloon-borne dedicated polarimeters like X-Calibur [52], POGOlite [53] and POGO+ [54], there have been attempts to use the polarization capability of spectroscopic instruments such as RHESSI, IBIS and SPI onboard INTEGRAL, CZTI onboard AstroSat to measure the polarization of hard X-ray bright sources like Crab [18, 21] and Cygnus X-1 [55]. A major reason for the lack of progress in X-ray polarimetry is that the X-ray polarization measurements are highly prone to systematics and require a large number of photons. However, X-ray polarimetry is expected to get an impetus in the near future with the launch of two dedicated missions - IXPE [56] and XPoSat [57, 58]. IXPE is expected to provide two orders of magnitude improvement in sensitivity within the energy range of 2 – 8 keV [59] over the earlier OSO-8 measurements, whereas the XPoSat mission is likely to provide ten times better sensitivity while extending the energy range to 8 – 30 keV.

X-ray polarization can be measured mainly by three different techniques which involve the principles of scattering, photoelectric effect, and Bragg reflection. Bragg reflection works only in discrete energies and hence has low sensitivity despite a high modulation factor. Photoelectric based polarimeters work on soft X-ray regime. In the hard X-ray or soft gamma regime, the dominant processes are Rayleigh/Compton scattering. Hence scattering based polarimeters are used to detect hard X-ray polarization. These three methods to measure polarization from soft to hard X-ray regime are described briefly in the following subsections.

1.2.1 Bragg Reflection Polarimetry

For the Bragg reflection technique, the incoming photons undergo constructive interference during reflection off the crystal at the glancing angle. The maximum reflectivity occurs for photons which have their electric vectors parallel to the crystal planes and zero reflectivity if the direction of electric vectors is normal. The Bragg crystal method, although highly efficient, can suffer from a narrow energy range strictly selected by the Bragg law.

1.2.2 Photo-Electric Polarimetry

Photoelectric polarimetry is based on the photoelectric effect where a k-shell photo- electron is emitted in the polarization direction. The cross-section depends on the azimuthal angle between the photon electric vector and the direction of the electron emission. Polarimeters based on the photo-electric effect utilize high Z materials (cross-section proportional to Z^5) as detectors and work in the energy range where the photoabsorption cross-section is the highest (soft X-ray regime).

1.2.3 Scattering Polarimetry

Scattering based polarimetry could be either Compton or Rayleigh/Thomson scattering. In Compton scattering, the incident photon gets in-elastic scattered and knocks off an electron, which takes away a part of the energy. In Rayleigh/Thomson the photon gets scattered elastically with the same incident energy. The differential cross-section for Compton scattering of a polarized X-ray beam is given by Klein-Nishina formula [60],

$$\frac{d\sigma}{d\Omega} = (\frac{{r_o}^2}{2})(\frac{v^{'2}}{{v_o}^2})(\frac{v^{'}}{v_o} + \frac{v_o}{v^{'}} - 2sin^2\theta cos^2\phi) \tag{1.1}$$

$$\frac{v^{'2}}{{v_o}^2} = \frac{1}{1 + (\frac{hv_o}{m_e c^2})(1 - cos\theta)} \tag{1.2}$$

where r_o is classical electron radius, m_e is electron mass, θ is the polar scattering angle and ϕ is the azimuthal scattering angle which is the angle between the electric vector of the incident photon and the scattering plane. Hence the

$\cos^2\phi$ term results in a polarization dependent cross-section which in turn results in an increased probability for photons to get scattered perpendicular to the polarization vector. Scattering based polarimeters have a scatterer surrounded by detectors to detect the scattered photons. In case of Compton, detection of scattered electron confirms a true Compton event. Hence Compton scattering has low background compared to Rayleigh. The advantage of Rayleigh is that, unlike Compton, it has better sensitivity at lower energies.

1.3 CZTI: A Hard X-ray Polarimeter onboard AstroSat

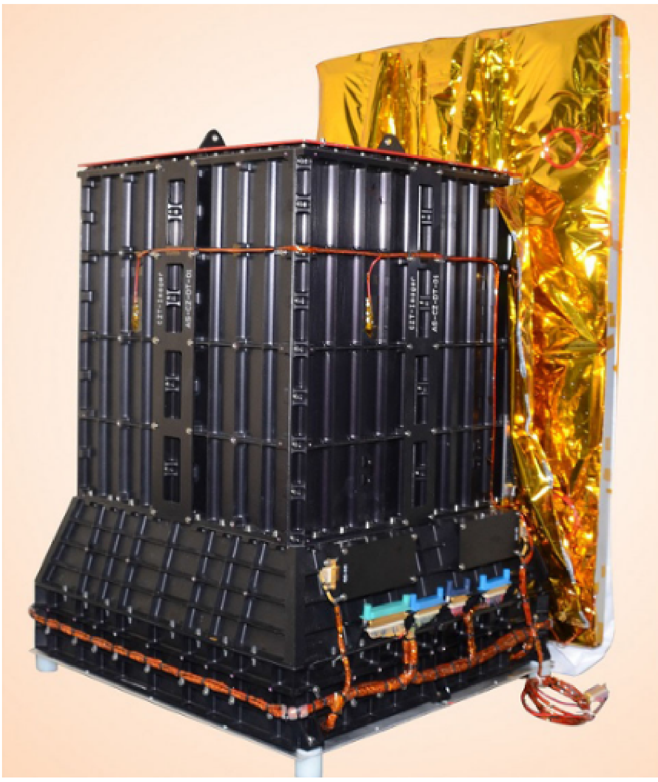

Figure 1.5: Cadmium Zinc Telluride Imager, one of the payloads onboard AstroSat. Credits: Bhalerao et al 2017 [61].

An ideal hard X-ray polarimeter is a focal plane instrument which consists of a scatterer (active/passive) in the middle surrounded by detectors [62, 57]. But the development of a hard X-ray telescope itself is a highly challenging task (NuStar is the only hard X-ray telescope till now) and there has been no dedicated focal plane polarimeter flown so far. In the absence of dedicated polarimeters, over the years there were constant attempts to perform polarimetry using open FOV detectors which were meant to do timing and/or spectroscopy. A detailed summary of these non-optimized polarimeters are discussed by McConnell 2016 [49]. BATSE onboard CGRO was a GRB all-sky monitor [22]. BATSE carried NaI(Tl) scintillators in eight detector assemblies, one at every corner of CGRO spacecraft. The detectors were meant to perform spectroscopy, however by measuring the distribution of albedo flux of photons scattered by Earth atmosphere, BATSE coarsely reported polarization of GRBs. The Reuven Ramaty High Energy Solar Spectroscopic Imager (RHESSI) was launched by NASA as a part of its Small Explorer missions in 2002. RHESSI was primarily meant to study solar flares and particle acceleration in flares through imaging and spectroscopy covering an energy range of 3 keV – 17 MeV [63]. RHESSI carried 9 Germanium detectors and a Beryllium scatterer and it measured polarization of bright X-ray sources by measuring the distribution of photons scattered between the Ge detectors. The International Gamma-Ray Astrophysics Laboratory (INTEGRAL) carried two sets of instruments: IBIS (15 keV – 10 MeV) [16] and SPI (20 keV – 8 MeV) [64] primarily meant to perform imaging and spectroscopy respectively. IBIS consists of Cadmium Telluride detectors, SPI carried Germanium detectors and both the instruments are attempted to perform polarimetry. These non-optimized polarimeters reported polarization of bright X-ray sources Crab, Cygnus X-1, and GRBs. But these instruments were not tested and verified to perform polarization on ground before launch. Hence there are complexities in the X-ray polarization community towards the results obtained from these instruments.

AstroSat is India's first multiwavelength astronomical satellite with five scientific payloads: Ultra Violet Imaging Telescope (UVIT), Soft X-ray Telescope (SXT), Scanning Sky Monitor (SSM), Large Area X-ray Proportional Counters (LAXPC), and Cadmium Zinc Telluride Imager (CZTI). AstroSat was launched in September 2015 and one highlighted feature of AstroSat is that it can simultaneously observe the celestial source of interest from ultraviolet to hard X-ray bands. CZTI is primarily meant to perform imaging and spectroscopy over an energy range of 20 – 150 keV. Figure 1.5 shows the final assembled CZTI flight model payload. CZTI consists of an array of 64 CZT modules where each detector is 5 mm thick and the detector module is further pixelated into 256 pixels (with a nominal pixel size of 2.5 mm × 2.5 mm). A 0.5 mm thick Tantalum coded mask provides imaging capability to the instrument in 20 – 150 keV energy range. Collimators made of Tantalum and Aluminium are placed above the detector housing to provide a restricted field of view of 4.6° × 4.6°.

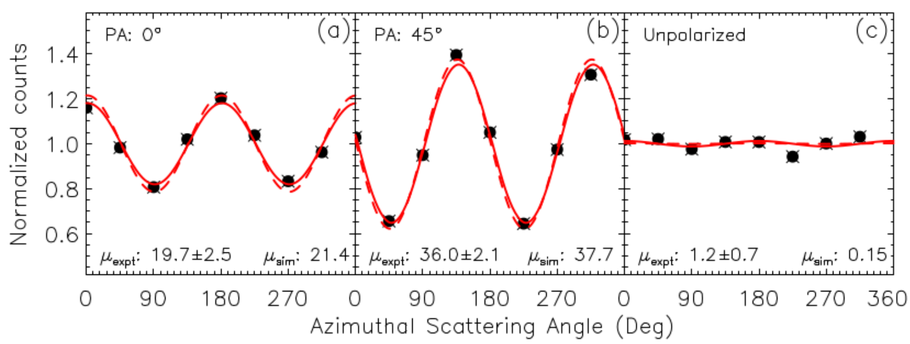

Figure 1.6: The figure shows the verification of on-axis polarimetric capability of CZT detectors. The modulation curves are obtained for unpolarized and polarized beam (polarization angles 0° and 45°). The solid curve shows the experimental modulation and dotted curve is obtained from the Geant4 simulations of the experimental setup. Credits: Vadawale et al 2015 [65].

CZTI also has the advantage of working in a photon tagging mode with a time resolution of 20 μs, that is any two events occurring within 20 μs will have the same timestamp (double events). The photons that are Compton scattered from a pixel and absorbed in any neighboring pixels could be detected from the double events. Equation 1.1 implies that the direction of the Compton scattered photon depends on the polarization of the incident photon. The combination of the significant Compton scattering cross-section of CZT detectors at energies beyond 100 keV and the availability of continuous time-tagged events makes CZTI a sensitive Compton polarimeter over 100 – 400 keV for bright X-ray sources [65, 66]. The scattering and absorbing pixels are identified by the ratio of energies deposited by the photon (pixel with lower energy is scatterer and higher energy is absorber). The direction of center of scatterer to absorber gives the azimuthal scattering angle, the histogram of which gives the raw azimuthal distribution of Compton scattered events. This raw azimuthal distribution should be corrected for a geometric effect that occurs due to the unequal solid angles subtended by the edge and corner pixels. This effect could be corrected by using the azimuthal distribution corresponding to unpolarized radiation that is obtained through Geant4 simulations (in detail in section 2.2.4).

The polarimetric capability of CZTI for pointed on-axis observations is verified through experiments and simulations pre-launch by Vadawale et al 2015 [65]. The experiments are performed for both polarized and unpolarized incident radiation and the results are complemented by the Geant4 simulations of the experimental setup. Figure 1.6 shows the modulation curves obtained for both experiments and simulations corresponding to two polarization angles. With this validation, V18 [21] performed polarization analysis of the Crab. V18 for the first time reported the phase resolved polarization of Crab over 100 – 380 keV. They found the polarization properties to be different at two peaks of Crab and also for the first time showed a clear swing in polarization across the off-pulse region.

1.4 Aim and Overview of the thesis

The major objective of the thesis is to develop techniques, required instrumentation, experiments, and simulations to carry out polarimetry over X-ray and infrared wavelengths with the Crab Nebula and GRBs as specific science targets.

1.4.1 Crab polarimetry using AstroSat-CZTI

CZTI onboard AstroSat is designed primarily for hard X-ray imaging and spectroscopy up to 100 keV. The polarization measurement capability of CZTI for on-axis sources over an energy rage of 100 – 400 keV was experimentally confirmed before the launch of AstroSat [65] and CZTI provided very interesting results on the phase dependent polarization measurements for the Crab pulsar. V18 showed how polarization changes during both the peaks as well as in the off-pulse region. Over the past 4 years of operation, Crab has been observed for $\sim 1800ks$ over multiple observations out of which the results of $\sim 800ks$ data was reported in V18. Following up on the work of V18, we perform phase resolved polarization analysis over 100 – 380 keV using ∼1800 ks of CZTI Crab data. The analysis is carried out independently following the analysis technique reported in V18. The results are consistent with those reported by V18 with a better statistical significance. We also perform energy dependent phase resolved analysis both over independent and dynamic bins.

1.4.2 GRB polarimetry using AstroSat-CZTI

CZTI is a hard X-ray polarimeter over an energy range of 100 – 400 keV. But apart from observing persistent sources like Crab, CZTI is also a prolific Gamma-ray burst (GRB) detector [67]. The collimators, coded mask, other payloads, and satellite structure become increasingly transparent at energies above 100 keV. On its very first day of operation, CZTI detected a GRB, GRB151006. By using this unique opportunity, the timing, spectral, and polarimetric analysis of GRB151006 were reported in Rao et al 2016 [67]. The polarization results of GRB151006 provided motivation to pursue GRB polarization analysis using CZTI. CZTI detected 47 GRBs from October 2015 to October 2016 out of which a sample of 11 bright GRBs were chosen for polarimetric analysis over an energy range of 100 – 350 keV. We selected GRBs with fluence higher than 10^{-5} erg cm^{-2} so that the number of Compton events are sufficient (∼400 Compton events) to attempt polarization measurements. Table 3.5 shows the polarization results obtained for the 11 bright CZTI GRBs. Detailed data analysis and the resulting polarization estimates for these 11 GRBs are reported.

1.4.3 Experimental verification of off-axis polarimetry of CZT detectors

CZTI turns out to be a very capable GRB polarimeter and is likely to provide polarization of a large sample of GRBs over its years of operation. Polarization measurements of off-axis sources like GRBs are challenging and they significantly depend on simulations. Geant4 [68] simulations are used to obtain the geometric corrections based on the simulation for unpolarized photons as well as to estimate the polarization fraction based on the simulation for 100% polarized photons, both incident from the direction of the GRB. Heavy reliance on Geant4 simulations to estimate GRB polarization may lead to some apprehensions. Hence, it is vital to ensure experimentally that CZTI is sensitive to measure the polarization of X-rays incident from a direction off-axis to the detector. Experimental confirmation for such capability are not available for non-dedicated GRB polarimeters including CZTI. Further, the report of polarization of 11 bright GRBs detected over a year shows the potential of CZTI as a GRB polarimeter and emphasizes the need for experimental confirmation. We report the experimental verification of off-axis polarization capability of CZT detectors, the results of which are complimented by Geant4 simulations.

1.4.4 NICSPol: A near-infrared imaging polarimeter

Having hard X-ray polarization measurement of Crab using CZTI and with the availability of an optical polarimeter at the 50 cm telescope of Physical Research Laboratory (PRL) [69], we explored the possibility to achieve multiwavelength polarization measurement of the Crab pulsar and Nebula. Radio, Optical, soft X-ray and hard X-ray/Gamma-ray polarization of Crab have been reported several times over the past decades. Despite these reports over multiple wavelength regimes, the infrared polarization of Crab has not been reported so far. In order to achieve this, we made use of the Near Infrared Camera and Spectrograph (NICS) which is one of the back end instruments for the 1.2 m Cassegrain f/13 telescope located at the Mount Abut Infrared Observatory of PRL[70]. We added polarimetric capability to the existing NICS, making NICSPol the first imaging IR polarimeter in India. NICSPol would provide a fantastic opportunity for simultaneous polarimetry of various astrophysical objects over a wide range of EM spectrum.

The thesis has been organized into seven chapters. Chapter 1 discusses the importance of polarization measurement and introduces the science targets of the thesis along with briefly describing the outline of the thesis. Chapter 2 discusses the energy dependent phase resolved polarization results of Crab in hard X-ray regime. Chapter 3 details the GRB polarization results using CZTI with a detailed description on the analysis procedure. Chapter 4 describes the experimental verification of the off-axis polarimetric capability of CZTI. Chapter 5 discusses the instrument design of NICSPol and its calibration results for IR polarimetric standards. The thesis is concluded in chapter 6 by summarizing the results, the implications based on the conclusions of the results along with the future prospects.

Chapter 2

Energy dependent phase resolved Crab polarimetry using AstroSat-CZTI

An ideal Compton scattering based hard X-ray polarimeter is a focal plane instrument that consists of an active scatterer, surrounded by detectors. But no dedicated focal plane polarimeter has been flown so far. As mentioned in section 1.2 in the absence of dedicated polarimeters, over the years there were constant attempts to perform polarimetry using open FOV detectors which were meant to do timing and/or spectroscopy. But these instruments were not tested and verified to perform polarization on ground before launch. Hence there were major controversies in the results obtained from those instruments. Unlike other instruments, CZTI was experimentally verified to perform polarization in hard X-ray regime before launch.

Having CZTI as a hard X-ray polarimeter one obvious choice of source to study is the constantly hard X-ray bright Crab pulsar and nebula. Crab has been studied observationally over the entire electromagnetic spectrum, but still the point of origin and the emission mechanism(s) behind the high energy photons remain unknown. Phase resolved polarization measurement of Crab could constrain theoretical models which predicts the geometry and nature of emission mechanism.

2.1 Polarization of Crab before AstroSat-CZTI

Polarization of Crab from optical to gamma regime have been reported by various ground and space-based instruments. Slowikowska et al 2019 [20] reported phase resolved and nebula subtracted phase resolved polarization of Crab in the optical regime using data from Optical Pulsar Timing Analyzer (OPTIMA) mounted at 2.56 m Nordic Optical Telescope. They reported a phase averaged polarization fraction (PF) and polarization angle (PA) of 9.8±0.1% and 109.5±0.1°. The first-ever reliable measurement of Crab polarization was made by Weisskopf et al 1978 [6] using a Bragg polarimeter onboard OSO-8. At energies 2.6 keV and 5.2 keV they reported PF, PA of 19.2±1.0%, 156.4±1.4° and 19.5±2.8%, 152.6±4.0°. PoGO+ reported a polarization of 20.9±5.0%, 124.0±0.1° for phase averaged Crab and $17.4^{+8.6}_{-9.3}$%, 137.0±15.0° for off-pulse region over the energy range 20 – 160 keV [71]. There have been multiple reports of Crab polarization using IBIS and SPI onboard INTEGRAL. Forot et al 2008 [18] and Dean et al 2008 [17] reported phase averaged polarization of 47.0^{+19}_{-13}%, 100.0±11.0° and 47.0±10%, 124.0±0.1° using IBIS and SPI respectively. Chauvin et al 2013 [72] used INTEGRAL SPI data over 130 keV – 8 MeV and found no significant change in PF with energy. Comparing optical data from Hubble Space Telescope with INTEGRAL IBIS Moran et al 2013 [19] showed the change in polarization from 2005 to 2012. In optical the polarization changed from 7.7±0.1%, 109.5±0.7° to 9.6±0.5%, 85.3±1.4° while in gamma it changed from 96±34.0%, 115.0±11.0° to

98.0±37.0%, 80.0±12.0°. Jourdian et al 2019 [73] used 16 years of INTEGRAL SPI data observed between 2003 – 2018 and reported a phase averaged polarization of 24±4.0%, 120.0±6.0°. PolarLight is a gas pixel detector onboard a cubesat that works in the soft X-ray range 3 – 4.5 keV and measures polarization based on electron track. PolarLight observed Crab during a glitch that happened on 23 July 2019 and reported a change in polarization before and after the glitch [74]. For the phase averaged Crab the PF, PA changed from 24.3±5.7%, 144.5±6.7° before the glitch to $11.3^{+3.7}_{-3.8}$%, 146.9±9.6° after the glitch. Similarly, in the on-pulse region, the polarization changed from $28.8^{+7.1}_{-7.3}$%, 142.7±7.2° to $10.1^{+4.7}_{-5.1}$%, 153.0±14.4° after the glitch [74].

Slowikowska et al 2009 [20] for the first time reported very precise measurement of phase resolved optical polarization of Crab. This report lead to development in theoretical predictions of phase resolved polarization [12, 13] based on the above mentioned models. Though stripped wind and slot gap models matched the trend of optical observation, the predictions neither took energy dependence nor polarization properties in the off-pulse region into consideration. Harding et al 2017 [14] predicted phase resolved polarization of rotation powered pulsars for optical and X-ray regimes. Apart from the optical report [20], there were no other reports on phase resolved polarization till Vadawale et al 2018 (V18). V18, for the first time, not only reported phase resolved polarization of Crab in X-rays but also showed significantly strong variation in the PF and PA in the off-pulse region. In the present work, we independently perform phase resolved polarization analysis over multiple energy ranges within 100 – 380 keV using Crab data observed using CZTI over 4 years.

We perform phase resolved polarization analysis over 100 – 380 keV using ∼1800 ks of CZTI Crab data. The analysis is carried out independently following the analysis technique reported in V18. The results are consistent with those reported by V18 with a better statistical significance. We obtain PF, PA of 33.4±4.1%, 143.6±1.7° at 8.1σ for phase averaged Crab and 35.2±7.4%, 144.2±3.0° at 4.7σ for off-pulse region respectively. We also perform energy dependent phase resolved analysis both over independent and dynamic bins. Section 2.2 describes the analysis procedure including the details of Crab and background data 2.2.2, calculating the pulse phase 2.2.3 and polarization estimation 2.2.4. Section 2.3 discusses the results of phase averaged 2.3.1, phase resolved polarization 2.3.2 and monthly averaged polarization of Crab over 4 years of observation 2.3.3. Section 2.3.4 discusses the results of the energy dependent phase resolved polarization followed by discussion in 2.4.

2.2 Data and Reduction

Crab has been observed multiple times by CZTI between 2015 – 2019. V18 used data observed until 2017 corresponding to a net exposure of ∼800 ks. In the current work, we use data with a total exposure of ∼1800 ks obtained over 32 observations. A critical step in Crab polarimetry is background subtraction, which varies over both space and time. Dedicated background observations are proposed for a specific region of the sky (RA:183.4796°, Dec:22.8°) which is closer to Crab and doesn't have any other hard X-ray bright sources in the field of view. We use 4 such background observations for the analysis.

2.2.1 Preliminary processing

CZTI data are saved in the form of event files with the position, time, and energy information of each event. The processing of data obtained after onboard bunch clean is done by cztpipeline [1]. A new form of the pipeline with better cosmic and Compton noise reduction is found to give identical results as given by the existing pipeline. The new noise clean procedure would provide better signal to noise in single event spectroscopy. Hence the well-established default cztpipeline is used for the processing of data.

All the instruments onboard AstroSat are switched off while the satellite is crossing the South Atlantic Anomaly (SAA) region. Though, the effect of high particle density affects the data that are observed closer to the SAA region. Using the latitude-longitude information, part of data observed during the region closer to SAA are automatically excluded and the user-defined Good Time Intervals (GTI) are saved. Further processing is carried out for only the data corresponding to the user-defined GTI. Along with the default event file (evt) cztipipeline provides double event (dblevt) files having information of two simultaneous events occurring within 20 μs, that is any two events occurring within 20 μs will bear the same timestamp. Barycentric correction is applied on the photon arrival times in evt and dblevt files using as1bary which is a part of cztipipeline

CZTI polarimetry is based on the principle of Compton scattering. Hence the first step in performing CZTI polarimetry of any source is to identify the Compton events in data. The selection criteria of the Compton events have been discussed in detail in Chattopadhyay et al 2014 [66]. The event file lists the pixel and detector ID, the PHA channel of detection, veto, and alpha coincidence flags.

[1] `http://astrosat.iucaa.in/czti/?q=node/7`

The Compton scattered events are normally expected to be captured within the 20 μs time window. However, since the readout in CZTI is done for one module at a time, if two events are registered in two different pixels in the same module, there is a certain probability that the two events would get different timestamps. Therefore, we select all the double pixel events happening within a coincidence window of 40 μs, as polarization information of the radiation is embedded in these double pixel events [66]. In the case of these double pixel events, the pixel with the lower energy deposition is considered to be the scattering pixel and the higher energy pixel as the absorbing pixel. Compton events are filtered out by applying the criteria: 1) spatial proximity of the pixels (immediate neighboring pixels) and 2) sum and the ratio of the deposited energies must be consistent with those expected for true Compton events for the scattering geometry of CZTI. Also, all events from noisy and spectroscopically bad pixels are excluded.

Table 2.1: List of CZTI observations of Crab constituting ∼1800 ks.

Observation ID	Exposure (s)
20151008_P01_120T01_9000000006_level2[a]	14329.2357091
20151010_P01_120T01_9000000016_level2[a]	13781.8771444
20151025_P01_161T01_9000000068_level2[a]	11357.9941288
20151112_P01_141T01_9000000096_level2[a]	41158.7088796
20151114_P01_141T01_9000000100_level2[a]	16776.8075317
20151114_P01_141T01_9000000104_level2[a]	21652.9024102
20151123_P01_156T01_9000000114_level2[a]	7803.35018265
20151124_P01_156T01_9000000118_level2[a]	22698.5394551
20151125_P01_156T01_9000000122_level2[a]	10426.0962708
20160107_G02_010T01_9000000252_level2[a]	59908.0474353
20160201_T01_052T01_9000000308_level2[a]	49407.9182373
20160203_T01_052T01_9000000312_level2[a]	60798.3042001
20160207_T01_052T01_9000000316_level2[a]	50706.4245581
20160331_T01_112T01_9000000406_level2[b]	114318.833294
20160822_G05_237T01_9000000620_level2[b]	84907.5504283
20161108_A02_090T01_9000000778_level2[c]	61376.6964276
20170114_G06_029T01_9000000964_level2[c]	78601.1994742
20170118_A02_090T01_9000000970_level2[c]	123064.920924
20170927_A03_086T01_9000001568_level2[d]	119575.38527
20180115_A04_174T01_9000001850_level2[d]	193845.410647
20180129_A04_174T01_9000001876_level2[d]	234120.659159
20180313_T02_013T01_9000001976_level2[d]	41939.0758255
20180408_T02_039T01_9000002026_level2[d]	10995.4488653
20180830_T02_058T01_9000002338_level2[d]	14958.5503704
20180912_T02_090T01_9000002360_level2[d]	17309.1050884
20180913_T02_090T01_9000002364_level2[d]	27794.7409702
20180914_T02_091T01_9000002368_level2[d]	49013.0857505
20181005_C04_007T01_9000002408_level2[d]	11738.9371462
20181014_C04_007T03_9000002436_level2[d]	13953.2354801
20181014_C04_008T01_9000002434_level2[d]	23080.1374907
20181029_T03_024T01_9000002472_level2[d]	74827.0796239
20190126_A05_159T01_9000002678_level2[d]	130825.117405

The details of all 32 observations along with the exposure times are listed here. The total exposure time is 1807 ks.
[a]20160116_G02_052T02_9000000276_level2, [b]20160604_G05_182T01_9000000484_level2, [c]20170122_G06_029T02_9000000974_level2, [d]20170412_G07_029T01_9000001158_level2 are the four corresponding background observations.

2.2.2 Background selection

The number of photons emitted from an astrophysical source decreases with respect to the photon energy. Also, the source photons are highly dominated by background emission. There are various factors like cosmic microwave, Earth albedo constitute background. On an average the Compton background rate is $\sim 12 - 14$ counts/s over an energy range $100 - 380$ keV whereas the Crab Compton rate over the same energy range is ~ 0.7 counts/s. This implies that the background subtraction is a critical step. The 32 observations of Crab are listed in Table 2.1 marked with the corresponding backgrounds used for each observation ID. For each Crab observation, depending on the time of observation a suitable background is chosen. Similar to Crab observations, filtering of user GTI and selection of Compton events are performed for background observations. Still, a major problem is the Compton rate of background is either slightly lesser or higher than Crab data. This is due to various reasons including the fact that the background rate changes with the orbits of observation. Hence we scale the background with a factor such that the background subtracted Compton count rate of Crab is 0.7 counts/s. The scaling factors for all the observations ranging from $0.9 - 1.2$ are plotted in figure 2.1.

2.2.3 Pulse profile

The pulse profile of Crab is a double pulse structure while the amplitude of the pulses varies over the electromagnetic spectrum. In the hard X-ray range, the amplitude of the first pulse which is the Main Pulse (MP) is higher than that of the second pulse that is the Intermediate Pulse (IP). In order to get the pulse profile, the light curve of Crab should be folded using an accurate pulse period. The single event files are used to obtain a precise pulse period for each Crab

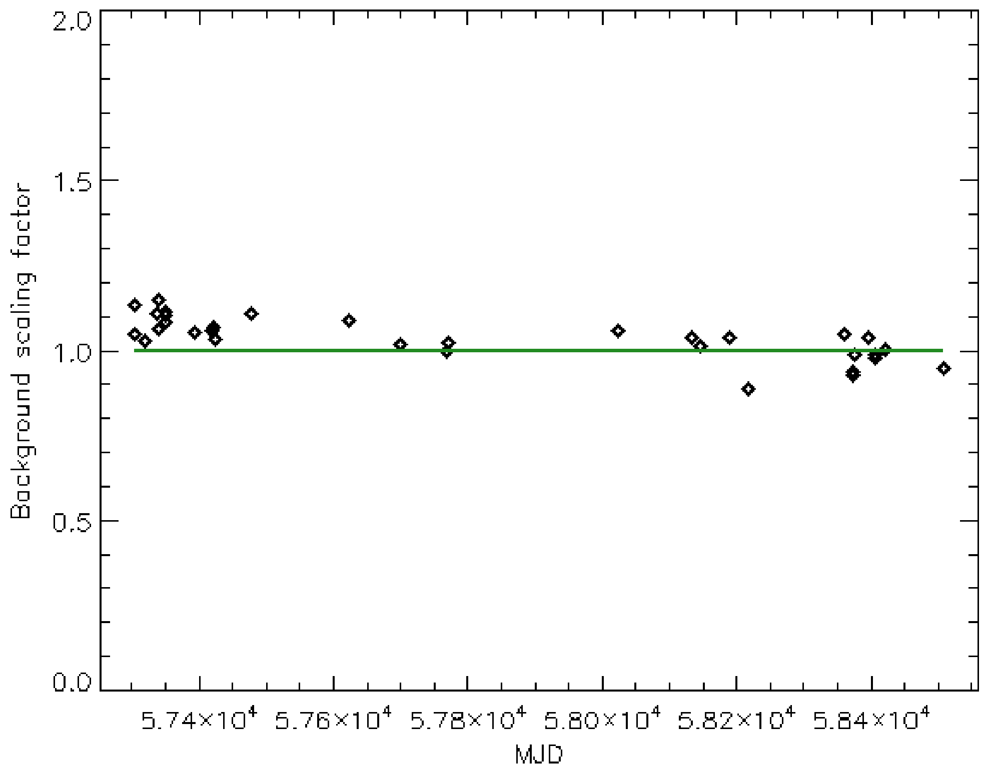

Figure 2.1: Background scaling factors used for all observations. The scaling factors applied for all 32 observations lie within 0.9 – 1.2.

observation. Since the Crab pulsar is slowing down at nanoseconds over a day, pulse period for individual observation at picosecond precision is needed. Initial guess values of pulse period and the first derivative of barycentric frequency $\dot{\nu}$ are obtained from the Jordell bank monthly ephemeris [2]. For each observation, the pulse period with picoseconds precision corresponding to maximum χ^2 value between a constant value and the pulse amplitude are obtained. In each case, the arrival time of the first event is used as respective epoch value. Hence the position of MP and IP would be at different phase values over all the observations. In order to add multiple observations, pulse profiles of all observations should be aligned at identical pulse phase values. We fit the MP with a Lorentz profile

[2]`http://www.jb.man.ac.uk/pulsar/crab/crab2.txt`

and calculate the epoch value, corresponding to which the MP could be shifted and aligned at pulse phase value 0.3. For each Crab observation, the single event pulse profile is folded using the calculated epoch, pulse period, and $\dot{\nu}$ values and the pulse profiles are co-added over all the observations. Figure 2.2 shows the single event pulse profile in blue obtained by adding 32 Crab observations. The Compton events filtered for each observation are folded with the pulse periods, $\dot{\nu}$, and epoch values obtained for respective observation using single events. The phase value of each Compton event is saved for all 32 Crab observations. In figure 2.2 the co-added Compton pulse profile of all observations is shown in red.

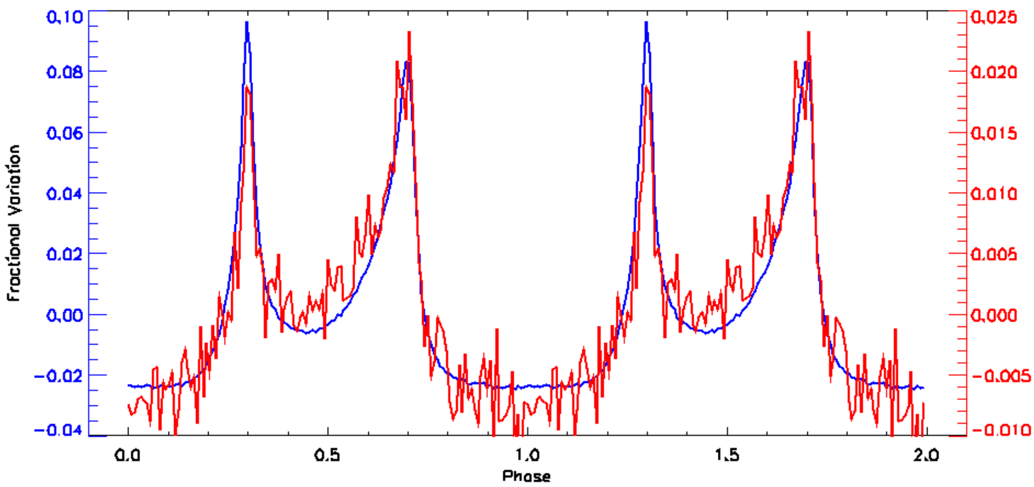

Figure 2.2: The pulse profile obtained by co adding 32 observations. The single event pulse profile is shown in blue which is overplotted with Compton events pulse profile in red. The amplitude of first pulse (MP) is higher than the second pulse (IP) in the single event pulse profile as it is expected in the hard X-ray range. In case of Compton event pulse profile, the IP has a higher amplitude. The pulse profile is distinctly seen in the Compton events, proving that the selection of Compton events is valid.

2.2.4 Polarization Estimation

The procedure to identify the Compton events and corresponding azimuthal scattering angle is explained in Section 2.2.1. From the histogram of the scattering angle of Compton events for both Crab and background data raw azimuthal distribution is obtained. Background subtraction is performed with the raw azimuthal histogram obtained for each Crab observation. Considering a 3 × 3 matrix of pixels with the center pixel being the scatterer, the solid angle covered by edge pixels is larger than that for corner pixels, and hence more photons are detected in edge pixels. Hence, the raw azimuthal distribution $\mathrm{M_{pol}}$ requires a correction for this geometric effect. The final geometry corrected modulation is obtained by following the equation 2.1. The modulation of unpolarized radiation $\mathrm{M_{unpol}}$ is obtained from the average counts in edge and corner pixels separately. The modulation curve $\mathrm{M_{corr}}$ is fitted with equation 2.2 and the best fit parameters give the modulation amplitude μ and PA. μ_{100} is the modulation amplitude corresponding to 100% polarized radiation. μ_{100} is obtained through Geant4 simulations using CZTI, where the incident radiation is a Power-law spectrum with α of -2.1, over an energy range 100 to 400 keV (mono energies 100 – 400 keV with 10 keV bin size) each for PA 0° – 45° (for every 5°). PF is calculated by dividing μ by μ_{100} corresponding to respective PAs.

$$M_{i,corr} = \frac{M_{i,pol}}{M_{i,unpol}} * \overline{M_{unpol}} \tag{2.1}$$

$$C = Acos(2(\phi - \phi_o + \pi/2) + B \tag{2.2}$$

It could be seen that PF is calculated from the modulation amplitude which is a positive definite quantity. Hence in case of low signal to noise, there are chances to measure definite polarization fraction even if the incoming radiation is unpolarized. Though, the polarization results obtained with high statistical significance are not affected by this. Polarization measurements follow the Rice distribution. Maier et al 2014 [75] followed the Bayesian approach in which the true polarization value is considered to be unknown and the higher and lower limit intervals are estimated based on real observed data. They provided a recipe for which the observationally obtained signal to noise is the input parameter. We use this recipe in to obtain the true PF, PA and the 1σ credibility intervals provide the errors of corresponding PF, PA.

2.3 Results

Polarization analysis of Crab is performed by following the procedure briefed in V18. Firstly, to ensure that the current analysis is definite, we re-analyze the $\sim$ 800 ks data used in V18. The results obtained are found to be matching well with the reported results and also results of the second set of data ($\sim$ 1000 ks observed post V18) are consistent with the results of the first set of data.

2.3.1 Phase averaged analysis

Phase averaged Crab is obtained by including all Compton events without dividing the data with respect to the pulse phase values. For the first set of data, in case of phase averaged Crab, we obtain a PF of 33.5$\pm$5.4 % and PA of 145.7$\pm$2.5 $^\circ$ at 6.2σ significance. The PF and PA reported by V18 for phase averaged Crab are 32.7$\pm$5.8 % and 143.5$\pm$2.8 $^\circ$ with more than 5σ confidence. Also by combining the data observed post V18 we obtain PF and PA of 33.4$\pm$4.1% and 143.6$\pm$1.7° at 8.1σ confidence level for the phase averaged Crab. Figure 2.3 shows the modulation corresponding to the total ∼1800 ks data.

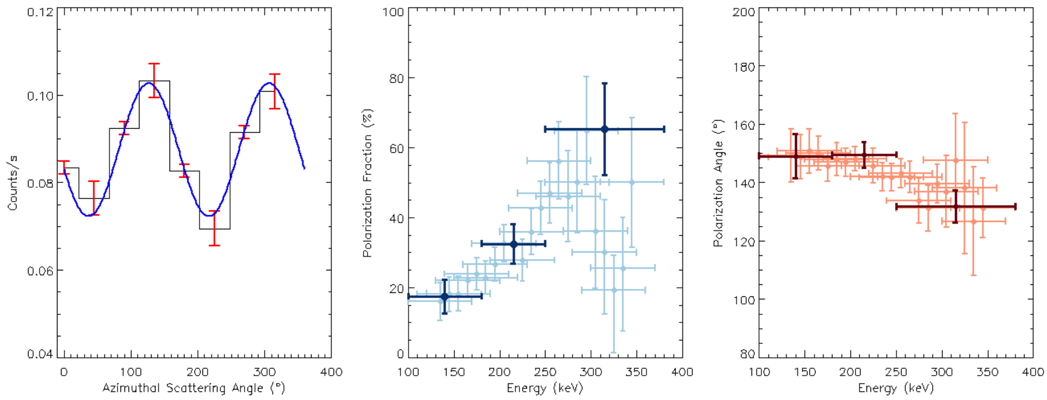

Figure 2.3: From the left: 1) The modulation curve obtained over 100 – 380 keV by using phase averaged data corresponding to 32 observations. This corresponds to a PF of 33.4±4.1 % and PA of 143.6±1.7 ° and 2) & 3) represents the energy dependence of PF and PA respectively for phase averaged Crab.

2.3.2 Phase resolved analysis

The phase values of Compton events corresponding to each observation are calculated and saved as mentioned in section 2.2.3. We select the Compton events corresponding to a given range of phase values from 0 to 1, each for a bin size is 0.1. The phase resolved polarization is performed by following dynamic binning of phases and a sliding window of phase value 0.01 is used. All Compton events corresponding to the total energy range of 100 – 380 keV are considered. Figure 2.4 shows the PF and PA obtained with respect to pulse phase. The flip in the PA at the middle of the off-pulse region which was reported in V18 could be prominently seen in figure 2.4. PA could be seen to increase at the rising edge of both the pulses and reaches a minimum in the falling edge of IP. PA rises at the off-pulse region and reaches the maximum in the middle of off-pulse region and starts to fall again from the middle. With respect to pulse phase a rise in PF is seen in the falling edge of IP, which reaches minimum in the middle of off-pulse region and starts to rise from the middle of off-pulse region. As shown in V18 the off-pulse region is found to be highly polarized. The off-pulse region (0.82 – 1.18) shows a PF of 35.2±7.4% and PA of 144.2±3.0° with 4.7σ confidence.

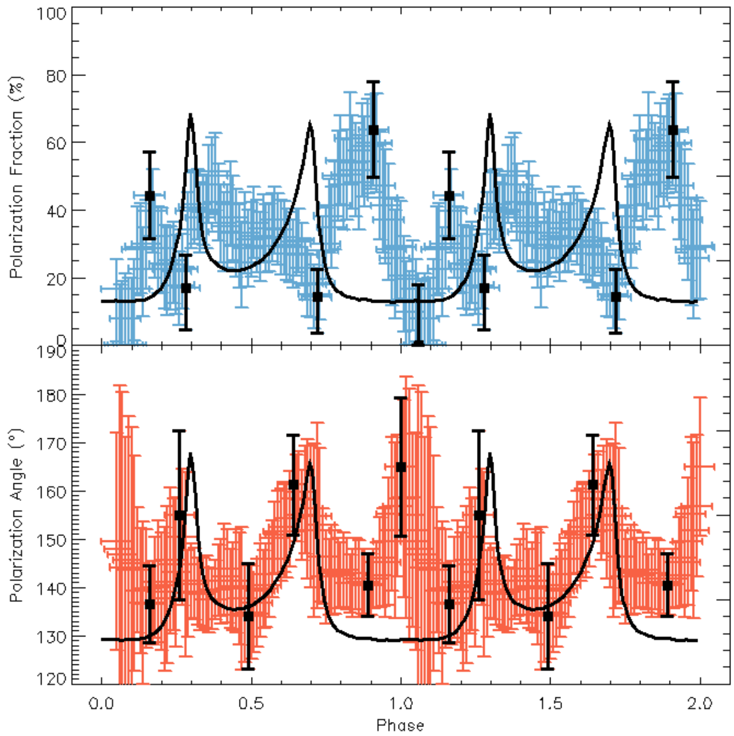

Figure 2.4: The figure shows the variation of PF and PA with respect to the dynamically binned pulse phase values of Crab pulsar. Each point is obtained for a phase width of 0.1 with a sliding window of 0.01. The black points represents the values where transition from maximum to minimum or vice verse happens. The PF reaches the minimum and PA reaches the maximum approximately at the middle of off-pulse region. The error bars in the data points are 1σ credibility intervals following Bayesian analysis.

2.3.3 Variation over time

The total ∼1800 ks of Crab CZTI data are observed over 32 observations. In order to check if there is any change in the polarization over the observed time, we analyzed the data with respect to the month of observation and co-added

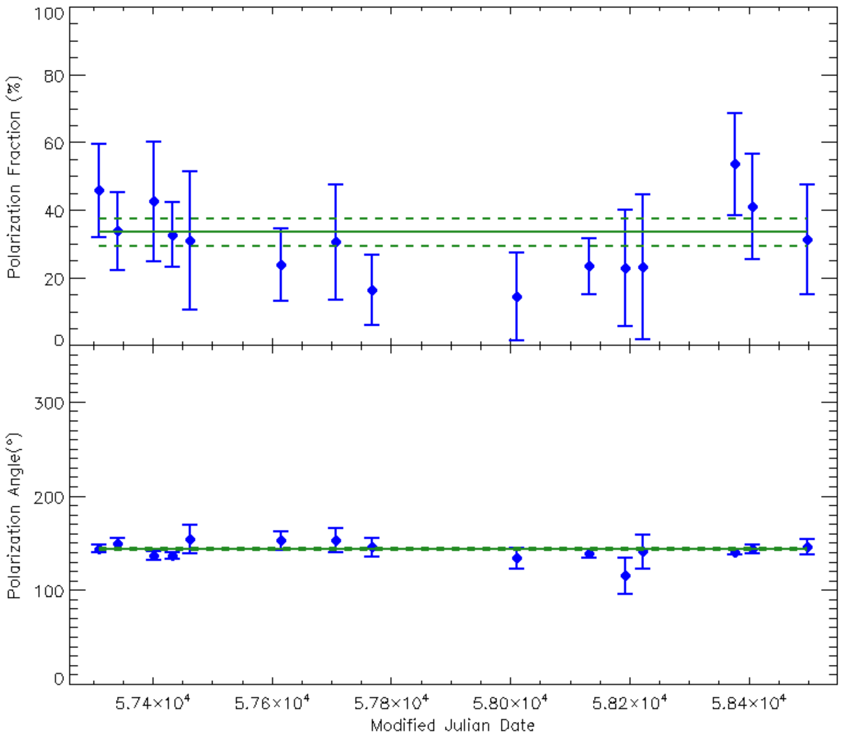

Figure 2.5: The plot shows the monthly average PF and PA values observed from 2015 to 2019 over 32 observations. The time in modified Julian date along the x-axis represents the middle of the month and multiple observations over a given month are added together. The solid horizontal green line represents the PF and PA value obtained for the total data, whereas the dotted lines shows the corresponding 1σ error bars.

multiple observations over a given month. Figure 2.5 shows the monthly averaged PF and PA values. The Modified Julian Date corresponding to the day 15 of each month is shown along the x-axis. The phase averaged PF and PA values obtained by co adding all observations are shown in horizontal green lines, along with the standard 1σ error bars shown in dotted lines.

2.3.4 Energy dependence

CZTI results of Crab polarization showed a swing in the PA and PF with respect to phase over the energy range 100 – 380 keV. Whereas PoGO+ [76] which works from 18 – 160 keV showed no change in the polarization in the off-pulse region.

Hence in order to verify if such change in polarization with respect to pulse phase has energy dependence, the phase resolved polarization should be performed over different energy ranges. Based on the data available we performed the phase resolved analysis with respect to energy in two ways: 1) Dynamic phase bins as followed in Section 2.3.2 over four independent energy bins 2) Dynamic energy bins from 100 – 380 keV with a bin size of 70 keV over a sliding window of 10 keV and independent phase bins, that is dividing the Crab into four regions MP, IP, Bridge, and Off-pulse region.

Independent energy bins, dynamic phase bins

In order to check if there is an energy dependence in polarization, as a first step we performed the phase resolved polarization as done in section 2.3.2 over multiple independent energy ranges. The dynamic binning of phase is done identical to the procedure mentioned in section 2.3.2. The PF and PA values obtained with respect to the pulse phase for energy bins are plotted in: 100 – 150 keV 2.6, 150 – 200 keV 2.7, 200 – 250 keV 2.8, and 250 – 380 keV 2.9. The variation of PF over 100 – 150 keV 2.6 is similar to the variation reported in V18, though the error bars are higher to due low detector sensitivity over that range. Though, no prominent variation of PA is seen in the off-pulse region. Figure 2.7 corresponding to 150 – 200 keV, shows a clear swing in PA at the middle of off-pulse region. PA at this energy range increases at the rising edge of MP, decreases to minimum at falling edge and increases towards the middle of the bridge region. Whereas at these respective pulse phase values an opposite trend is seen in the PF. That is PF decreases at the rising edge of MP, increases at the falling edge and reaches minimum at the centre of the bridge. Also the PF increases to $\sim$60% at the falling edge of IP and decreases till $\sim$60% at the middle of the off-pulse region where the

PA flips to reach ∼200° from ∼150°. The small error bars are due to the fact that the efficiency of CZTI is significantly better over the energy range 150 – 200 keV. In the energy range 200 – 250 keV 2.8 PF is high at the rising side of MP and low at the falling side. In the bridge region a swing of PF with respect to pulse phase is faintly seen. The PF swings from maximum to minimum at the middle of the bridge and increases again. Though there is no prominent change in PF at the bridge region, the PA clearly increases along the IP and reaches maximum at the peak. The two peak structure of PA is seen at the off-pulse region reaching a minimum at the centre of off-pulse region. The results for energy range 250 – 380 keV in figure 2.9 has large error bars because of the poor detector sensitivity.

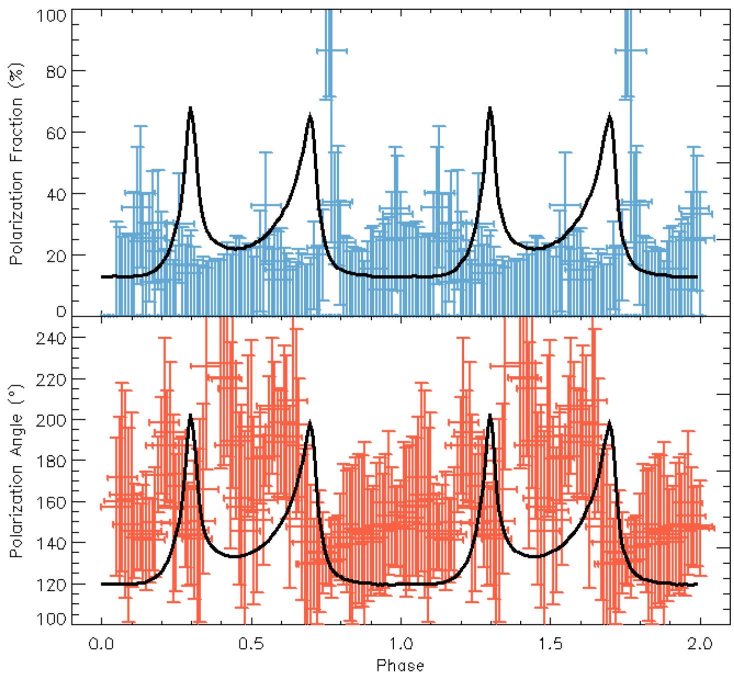

Figure 2.6: The figure shows the phase resolved polarization of Crab over an energy range of 100 – 150 keV

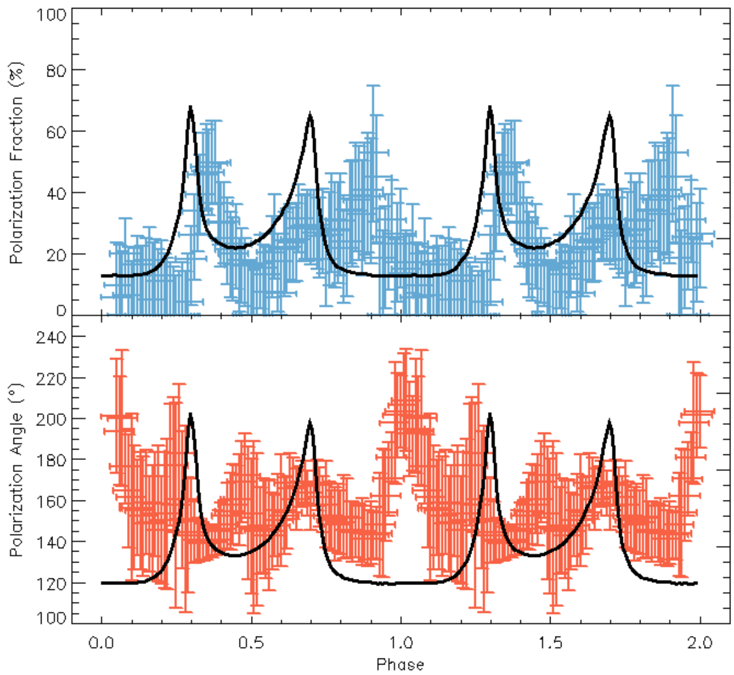

Figure 2.7: The figure shows the phase resolved polarization of Crab over an energy range of 150 – 200 keV

Independent phase bins, dynamic energy bins

The next step in the phase resolved polarization with respect to energy is to analyze total Crab data over dynamic energy bins. The total energy range 100 – 380 keV is divided into bins of 70 keV with a sliding window of 10 keV. Since the energy bin size is 70 keV, phase resolved analysis as performed in 2.3.4 would result in poor statistics. Hence we choose independent phase bins by dividing the Crab into four of its pulse profile features: 1) Main pulse, 2) Bridge, 3) Intermediate pulse, and 4) Off-pulse region. Each of these regions are divided into three equal parts in order to verify whether the energy dependence of PF and PA changes within a region of interest. The following subsections show the PF and PA variation with respect to energy for the phase averaged Crab, the four regions and each of the regions in three parts.

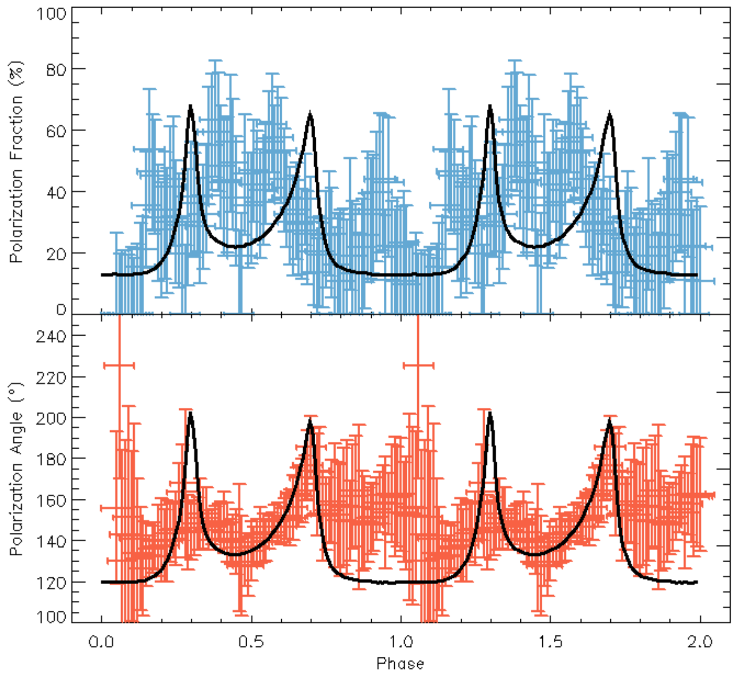

Figure 2.8: The figure shows the phase resolved polarization of Crab over an energy range of 200 – 250 keV

Table 2.2: Polarization results obtained for phase averaged Crab, off-pulse region, MP, IP, bridge over various energy ranges.

Source	Energy range (keV)	PF (%)	PA (°)	Significance (σ)
Phase averaged Crab	100 – 380	33.4±4.1	143.6±1.7	8.1
	100 – 180	18.1±4.7	149.1±4.6	3.9
	180 – 250	33.0±5.5	149.5±3.3	6.0
	250 – 380	66.5±12.9	131.8±2.9	5.2
Off-pulse region	100 – 380	35.2±7.4	144.2±3.0	4.7
	100 – 180	25.1±8.3	150.7±6.4	3.1
	180 – 250	23.5±9.5	150.8±8.5	2.5
	250 – 380	85.3±24.3	133.4±3.8	3.5
Main pulse	100 – 380	36.9±7.2	140.1±2.3	5.1
	100 – 180	13.4±7.7	147.1±9.4	1.7
	180 – 250	44.3±10.2	145.4±3.6	4.3
	250 – 380	78.1±21.9	124.9±5.3	3.6
Bridge	100 – 380	33.2±9.0	139.2±3.3	3.7
	100 – 180	13.2±10.9	149.1±14.7	1.2
	180 – 250	32.8±11.8	145.2±6.1	2.8
	250 – 380	81.8±27.5	126.6±5.8	3.0
Intermediate pulse	100 – 380	30.6±6.4	149.3±3.9	4.8
	100 – 180	17.3±7.5	147.7±7.1	2.3
	180 – 250	36.9±8.6	155.6±6.0	4.3
	250 – 380	41.0±20.0	143.2±7.9	2.1

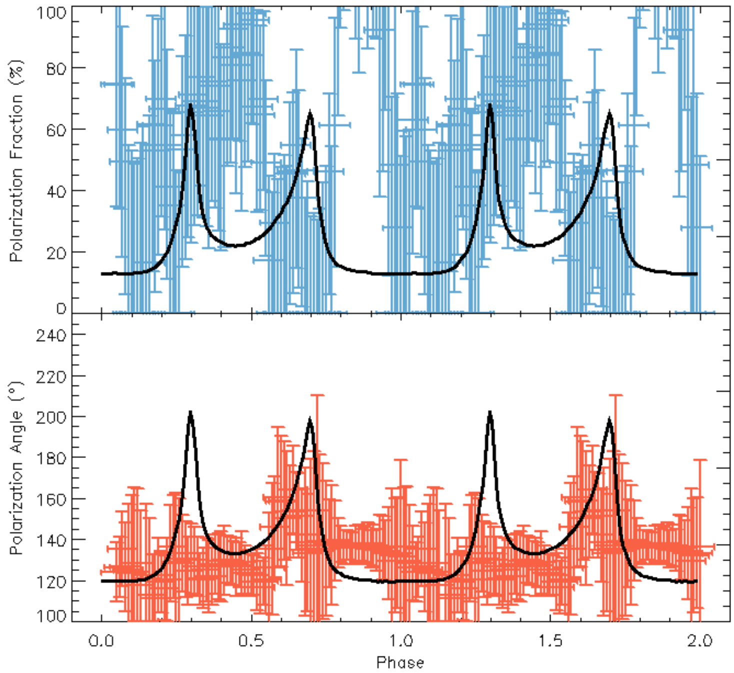

Figure 2.9: The figure shows the phase resolved polarization of Crab over an energy range of 250 – 380 keV

Phase averaged Crab

The energy dependence analysis is performed in the total phase averaged Crab data, without dividing it with respect to pulse phase. Figure 2.3 shows the PF and PA obtained for various energy ranges from 100 – 170 keV to 310 – 380 keV in blue and red points respectively, whereas the modulation curve corresponds to 100 – 380 keV. The three highlighted points of PF and PA corresponds to 100 – 180 keV, 180 – 250 keV and 250 – 380 keV. The PF and PA values obtained for Crab along with significance over independent energy ranges, 100 – 380 keV, 100 – 180 keV, 180 – 250 keV and 250 – 380 keV are listed in Table 2.2. We observe a linear increase in PF with respect to energy, while PA remains constant. Although the dynamic points in PF show a decreasing trend above ∼280 keV, for the energy range 250 – 380 keV the PF is still higher.

Main pulse

The phase range corresponding to the MP of Crab is 0.18 – 0.42. We divide the MP into three parts, 0.18 – 0.26, 0.26 – 0.34, and 0.34 – 0.42 and the modulation curves corresponding to 100 – 380 keV for all four cases are plotted in figure 2.10. In figure 2.10 each column represents a phase range which is marked by vertical red lines over the pulse profile. For the overall MP the PF is seen to be increasing with energy while the PA remains constant. We observed a linear increase in PF for the first and second part of MP, whereas for first part the PA follows an opposite trend to PF by decreasing from $\sim 200^{\circ} - 120^{\circ}$ and for the second part the PA remains constant. For the third part of MP the dynamic PF points increase till $\sim$250 keV, show a decreasing trend till $\sim$320 keV and increases again above 320 keV. While the PA for third part show a minor change from $\sim$130° to 150° till 250 keV and decreases towards higher energies. The PF and PA values corresponding to the three highlighted data points in each panel are listed in Table 2.2.

Bridge

The bridge region between both Crab pulses span over pulse phase values 0.42 – 0.56. the modulation curves corresponding to 100 – 380 keV for the bridge and for phase ranges 0.42 – 0.47, 0.47 – 0.51, and 0.51 – 0.56 which are three parts of bridge are plotted in figure 2.11. The phase range in each case are marked by vertical red lines over the pulse profile. As seen in MP, for the bridge the PF is seen to be increasing with energy while the PA remains constant. A linear increase in PF and decrease in PA is observed for the first part of bridge similar to the trend in first part of MP. The second part of bridge show a sharp decrease in PF till $\sim$220 keV and starts increasing towards higher energies. In the third part

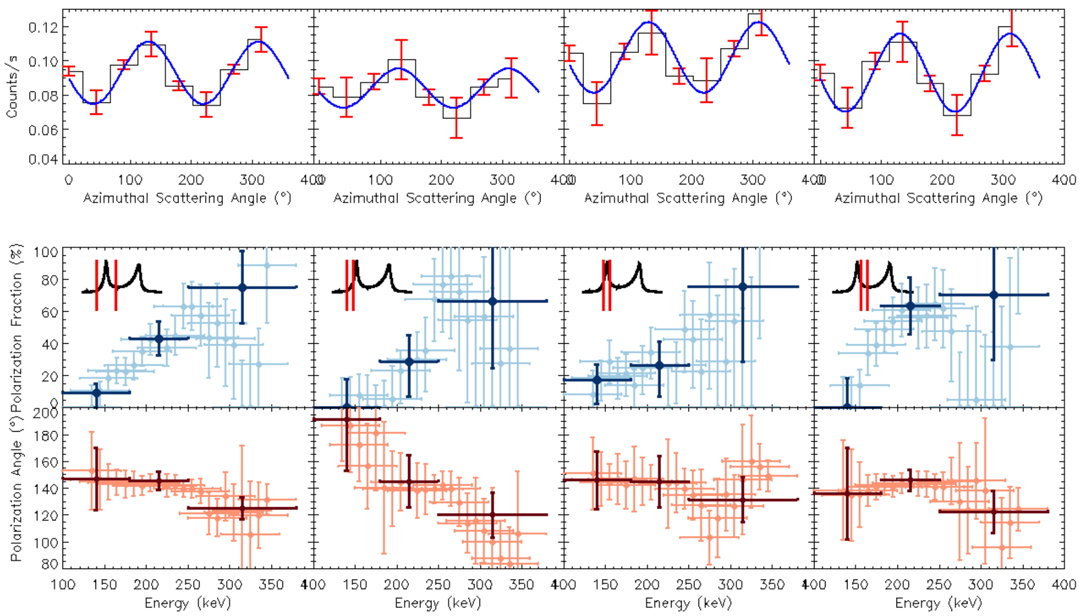

Figure 2.10: The figure corresponds to the polarization obtained for MP and three sections of MP(regions marked in pulse profile). The first row in the figure represents the modulation curve obtained for the MP and three parts of the MP. The second and third row represents the energy dependence of PF and PA respectively for the MP

of bridge the PF points increase with energy while the PA remains constant to be $\sim 140°$. The PF and PA values corresponding to the highlighted data points in each panel for three independent energy ranges defined earlier are listed in Table 2.2.

Intermediate pulse

The IP of Crab corresponds to phase range 0.56 – 0.82 which is divided equally as 0.56 – 0.65, 0.65 – 0.74, and 0.74 – 0.82. The modulation curves corresponding to 100 – 380 keV for all four cases are plotted in figure 2.12. For IP the PF is seen to have a slight increment with energy while the PA remains constant at around $\sim 150°$. For both first and second part of IP we see the variation of PF to be similar though the way PA varies is different. The PF in both the cases increase till $\sim$220 keV and show a slight decrease towards higher energies. In the first part

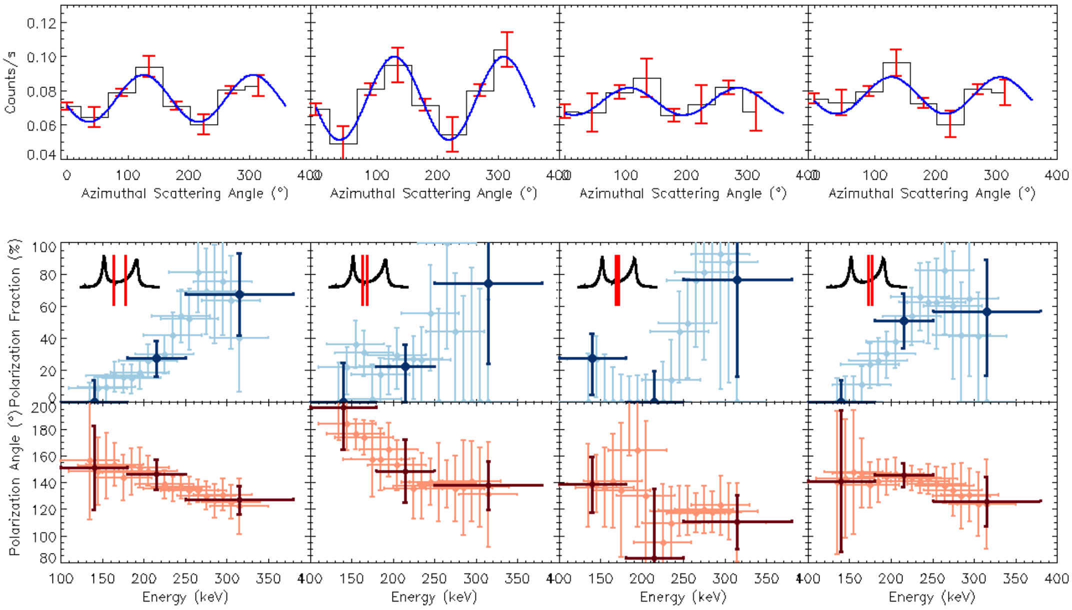

Figure 2.11: The figure corresponds to the polarization obtained for the bridge region and bridge in three sections (regions marked in pulse profile). The first row in the figure represents the modulation curve obtained for the bridge region and three parts of the bridge. The second and third row represents the energy dependence of PF and PA respectively for the bridge region

of IP the PA decreases from ∼200° to ∼140° till ∼220 keV and increases again, while in second part an opposite trend is seen. The PA increases from 100 keV to 220 keV (∼ 145° to ∼ 180°) and starts decreasing in the higher energy side (till ∼ 130°). For the third part of IP the dynamic PF points slightly decrease till ∼220 keV and increases above 220 keV. While the PA for third part remain constant at ∼140°. The PF and PA values corresponding to the three highlighted data points for IP, and its three independent parts are listed in Table 2.2.

Off-pulse region

The off-pulse region of Crab lies between pulse phase values 0.82 – 1.18. V18 showed that the off-pulse region is highly polarized with PF and PA of 39.0±10.0% and 140.9±3.7° at 4σ confidence. By using the data comprising 32 observations we obtain a PF of 35.2±7.4% and PA of 144.2±3.0° with 4.7σ significance. We

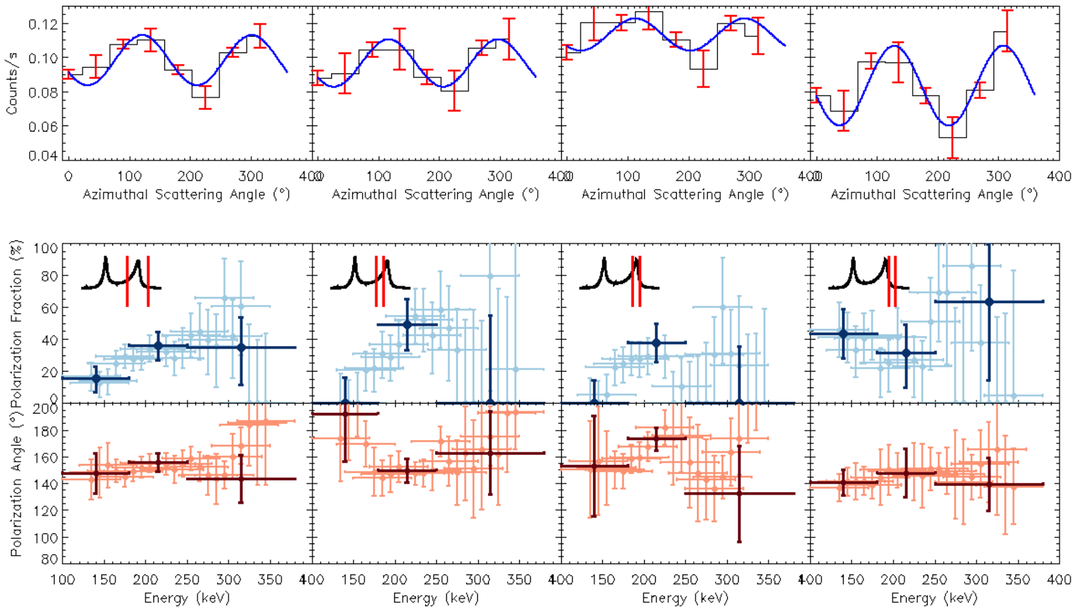

Figure 2.12: The figure corresponds to the polarization obtained for the IP and three sections of IP(regions marked in pulse profile). The first row in the figure represents the modulation curve obtained for the IP and three parts of the IP. The second and third row represents the energy dependence of PF and PA respectively for the IP

divide the off-pulse region into three parts, 0.82 – 0.95, 0.95 – 1.05, and 1.05 – 1.18 and the modulation curves corresponding to 100 – 380 keV for all four cases are plotted in figure 2.13. The PF for the entire off-pulse region remains almost constant at ∼30% till 220 keV and linearly increase above 220 keV, while the PA doesn't show significant change with respect to energy. The first part of off-pulse region shows increase in PF with respect to energy, whereas no change in PA is seen. The second part of off-pulse region doesn't show a significant change in PF with respect to energy. The PA in the second part increases from ∼150° at 100 keV to ∼200° at 220 keV, and decreases to ∼150° at 320 keV. The third part of off-pulse region shows no variation in PA and the PF increases above 220 keV. This correlates well with the results in section 2.3.4. The swing in the PA is seen only at the second part which lies at the middle of the off-pulse region. Also the PA swings above 160 keV at this region. Table 2.2 contains the values of PF and PA for the highlighted data points corresponding to the independent energy ranges.

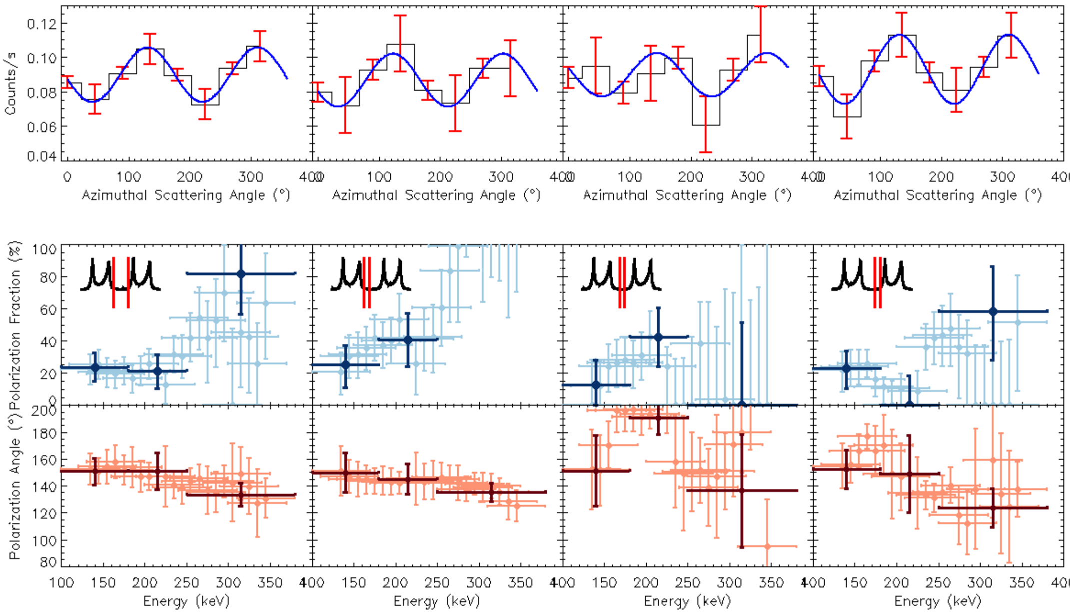

Figure 2.13: The figure corresponds to the polarization obtained for the off-pulse and off-pulse region in three sections (regions marked in pulse profile). The first row in the figure represents the modulation curve obtained for the off-pulse and three parts of the off-pulse region. The second and third row represents the energy dependence of PF and PA respectively for the off-pulse region

2.4 Discussion

Polarization analysis of Crab is performed using data obtained by CZTI over its four years of operation. We performed phase averaged and phase resolved polarization analysis both over various energy ranges between 100 – 380 keV. The phase averaged Crab for the overall energy range 100 – 380 keV is found to be polarized with a PF of 33.4±4.1% and an associated PA of 143.6±1.7°. The phase averaged polarization is obtained with 8.1σ confidence, which is the best statistical significance reported so far in X-ray regime. The off-pulse region for the same energy range is found to be highly polarized with PF and PA of

35.2±7.4% and 144.2±3.0° with 4.7σ confidence. Along with the off-pulse region we divide Crab pulse profile based on the pulse features into main pulse, bridge and intermediate pulse and performed polarization analysis over dynamic energy bins. From the results listed in table 2.2 it could be seen that for all the regions of the pulse profile the PF increases with respect to energy. Though there is no significant change in PA with respect to energy. The phase resolved polarization over 100 – 380 keV show clear swings in polarization at the peaks and off-pulse region. The change in PA in the off-pulse region reported by V18 is reconfirmed with better detection significance.

The polarization analysis with respect to pulse phase is performed over four independent energy ranges: 100 – 150 keV, 150 – 200 keV, 200 – 250 keV and 250 – 380 keV and we find no swing in PA in the off-pulse region for 100 – 150 keV while the swing is significantly seen over 150 – 200 keV. This shows that the change in polarization in the off-pulse region has a clear energy dependence. We further performed the energy resolved analysis following dynamic energy binning by dividing the four regions of Crab pulse profile each into three parts. This way of analysis shows clear change in polarization with respect to energy within each region of interest. More importantly, in the off-pulse region, all three sections of the region exhibit PA of ∼150° below 160 keV. However, over 180 – 250 keV energy range the PA swings from ∼150° in first section to ∼190° in middle section and changes back to ∼150° in the last section. This result is in accordance with the polarization report of PoGO+ where no swing in PA was observed over 18 – 160 keV.

Feng et al 2020 [74] reported change in polarization for on-pulse and phase averaged Crab during a glitch that happened on 23 July 2019. The CZTI data used in the current work are observed between 2015 – 2019 during when 5 glitches occurred in Crab. On-pulse, off-pulse and phase averaged polarization analysis are performed independently for seven observations which happened within 100 days of glitch occurrence. The results show no statistically significant variation in polarization over 100 – 380 keV before and after the occurrences of glitches. A detailed investigation on energy dependence of change in polarization during glitch necessitates prompt long exposure observations during glitch occurrence.

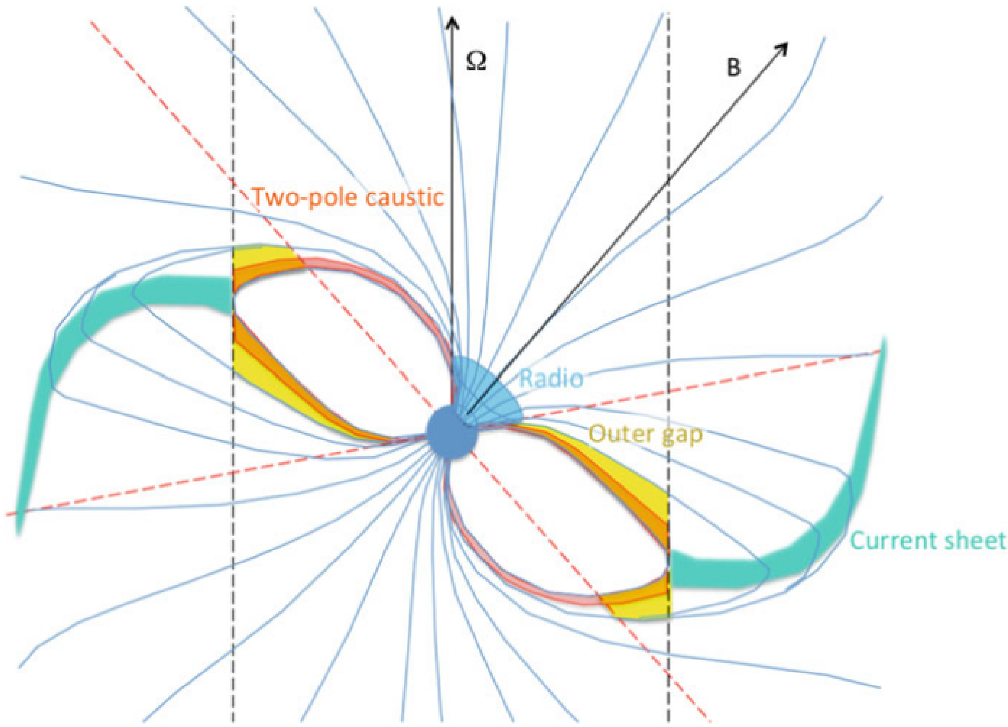

Figure 2.14: The figure illustrates the geometrical origin of high energy photons described by various models: polar cap, two-pole caustic, outer gap, and stripped wind models. Credits: Harding 2019 [77].

The polarization measurement of Crab is primarily important because these properties are related directly to the geometry, emission process and the nature of magnetic field which remain unknown. Multiple theoretical models are developed to explain the point of origin and corresponding radiation mechanism behind the high energy photons (>optical wavelengths) in rotation powered pulsars. The classical polar cap model (blue) states that the high energy photons originates closer to poles. The high electric field resulting due to the magnetic field of $\sim 10^{12-13}$ G, strips off electrons from the Neutron Star (NS) surface and these ultra relativistic electrons through curvature radiation along the open field lines emit high energy photons. According to the two-pole caustic model (red) the emission originates at a narrow region on last open field line from NS surface till the light cylinder while in the outer gap model (yellow) the narrow region on last open field line is between the null charge surface and end of light cylinder. These three models imply that the emission originates inside the light cylinder. In the stripped wind model (green) the emission is due to the escaping particles through open field lines outside the light cylinder. Figure 2.14 illustrates the geometrical representation of all the four models. However, the polarization predictions of all these models heavily rely on various parameters like viewing angle, inclination angle, pitch angle, light cylinder radius and even a small change in one of these parameters would change the polarization prediction drastically. In addition to that, the predictions of these models have not taken the off-pulse region into account still.

The current results of phase resolved polarization over various energy ranges imply the importance of development of theoretical models based on observations. The phase resolved polarization results is clearly seen to be differing between optical and hard X-ray regime, and also change within the hard X-ray regime. Harding et al 2017 reported that, the emission of high energy photons are expected to originate outside the light cylinder if there is no significant change in PA for phase averaged Crab over the electromagnetic spectrum. Though the present results along with the reports from literature hint the geometrical origin of the high energy photons outside the light cylinder, more advancement in theoretical models is still necessary. The clear change in polarization in the off-pulse region can not be explained by the current models where the off-pulse region is not taken into consideration. The work described in this chapter emphasize further exploration of theoretical models along with continuous observations to yield higher significance.

2.5 Summary

This chapter described the results of phase resolved polarization of Crab using CZTI data. The polarization analysis is performed over multiple energy ranges between 100 – 380 keV. The dynamic phase binning method is followed over four independent energy ranges and the dynamic energy binning is followed for the four regions of Crab pulse profile. The polarization of phase averaged Crab is reported with best statistical significance and the off-pulse region is found to be highly polarized over the energy range 100 – 380 keV. Though the swing in polarization at the middle of off-pulse region over 150 – 200 keV is prominent, no swing in PA is seen over 100 – 150 keV. The PF increases with respect to the photon energy over all regions of Crab. The energy dependence observed in the polarization of MP, IP, bridge, and off-pulse region strongly indicate development of theoretical models taking off-pulse region and energy of incoming photons into consideration.

Chapter 3

GRB polarization using AstroSat-CZTI

As discussed in chapter 2, CZTI provided interesting hard X-ray polarization results of Crab. Apart from Crab, CZTI is proposed on a regular basis to observe one of the the high mass X-ray binaries Cygnus X-1 and bright transient sources. CZTI can act as a GRB monitor since the collimators, other supporting structures of CZTI and satellite structure gets increasingly transparent at energies >100 keV. CZTI that could act as a GRB detector along with its capability to measure polarization provides a unique opportunity to measure GRB polarization. GRB polarimetry with CZTI is very similar to the on-axis polarimetry of persistent sources, but with the following advantages and limitations.

Advantages:

- Because CZTI polarimetric observations do not require any change in the hardware configuration, polarimetric analysis can be attempted from data obtained in the standard mode. CZTI detects 4–5 GRBs in a month. Polarimetric analysis can in principle be attempted for any detected GRB.

- GRB prompt emission is expected to be strongly polarized owing to its non-thermal origin and the involvement of high bulk Lorentz factors, thus making detection easier.

- Compared to bright persistent sources like Crab or Cygnus X-1, GRBs provide higher signal to noise ratio in Compton events resulting in a higher polarimetric sensitivity.

- Accurate polarimetric background measurements are available just before and after the GRB event.

Limitations:

- GRBs are isotropic events that occur for a very short time (fraction of seconds to a few tens of seconds). That is their occurrence is completely random in space and time.

- Owing to off-axis angle of incidence of incoming photons, the azimuthal angle distribution differ significantly from on-axis sources. For each GRB, the correction for geometric effect requires the modulation corresponding to 100% unpolarized radiation, by simulating the GRB with its observed spectral parameters and angle of incidence.

We performed polarization analysis for GRBs detected by CZTI from October 2015 to October 2016, and reported polarization results for 11 bright GRBs. Before AstroSat, polarization measurements existed only for tens of GRBs and CZTI over its one year of operation added 11 more GRBs to the list.

3.1 Introduction

The GRB polarimetric studies provide a unique opportunity to address the nature of the magnetic fields close to the relativistic jet launching site [47, 78]. Based on this promising capability of addressing the central engine of GRBs, there have been many attempts over the past decade to measure the polarization of prompt emission, both by using dedicated polarimeters as well as instruments primarily designed for non-polarimetric observations. The first polarization measurement of GRB prompt emission was made in 2004 with RHESSI instrument [79] designed for solar hard X-ray spectroscopy, though there has been some controversy about it [80, 81]. Subsequently there were reports of GRB polarization with INTEGRAL SPI [82, 83, 84] and IBIS [85, 86, 87]. The GAP instrument on board Japanese IKAROS mission was the first dedicated GRB polarimeter designed and calibrated for polarization measurements. GAP was launched in 2010 and detected polarization of three GRBs [88, 89]. The second dedicated GRB polarimeter, POLAR [90], was launched in 2016 on board Chinese space-station Tiangong 2, which measured polarization for five GRBs [91]. POLAR, however, stopped its operation on 2017 March 31. Hence, presently and in near future CZTI is one prolific GRB polarimeter in hard X-ray regime. Using CZTI, it is possible to have reliable polarization measurements of $\sim$10 GRBs per year.

This chapter discusses the detailed data analysis and the resulting polarization estimates for 11 CZTI GRBs. The details of preliminary processing of CZTI data and procedure to select Compton events are explained in detail in chapter 2 (section 2.2.1). Section 3.2 discusses the details of the GRBs in our sample. Section 3.3 discusses about the details of AstroSat mass model and in section 3.4 the procedure to obtain PF and PA are discussed. This is followed by the final results and discussions in sections 3.5 and 3.6 respectively.

3.2 GRB: Source and Background counts

Over its first year of operation, CZTI detected 47 GRBs [1] out of which 11 GRBs were selected which are bright enough to give sufficient number of Compton events (the number of double events satisfying the Compton criterion greater than 400) to attempt polarization analysis. Localization of these GRBs in CZTI co-ordinates was done using the position information available in the Swift and Fermi GRB data bases. Our choice of bright GRBs with sufficient Compton events corresponds to a limiting fluence of 10^{-5} erg cm^{-2}. A clear detection of the GRB in Compton events shows the pertinence of the event selection criteria. Figure 3.1 shows the light curve of GRB 160623A in single (blue line) and Compton events (black data points).

GRB polarization measurements are difficult due to the scarcity of flux in most cases and the extreme photon hungry nature of X-ray polarimetry. One major advantage in GRB polarization in comparison with Crab is the availability of precise background information. GRBs in general occur for a few seconds, and they are several Crab units brighter than background. For each GRB, data corresponding to a few hundred seconds before (pre-GRB) as well as after the occurrence of GRB (post-GRB), independently and together (pre-GRB+post-GRB) constitute accurate background. We have treated the statistical uncertainties and the possible sources of systematics which may introduce false polarimetric signature, with utmost care for each of the GRBs. The details of preliminary processing of CZTI data and procedure to select Compton events are explained in detail in chapter

[1] `http://astrosat.iucaa.in/czti/?q=grb`

2 (section 2.2.1).

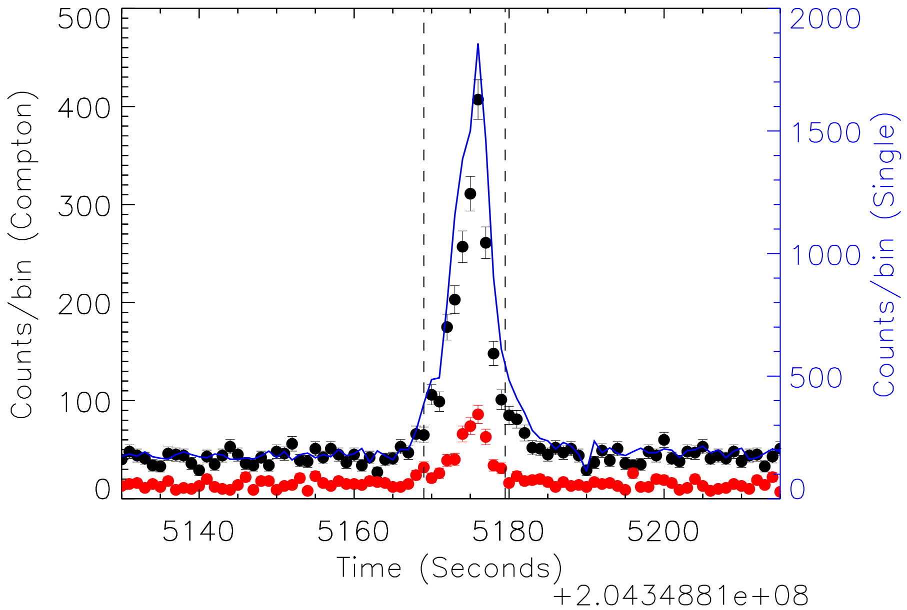

Figure 3.1: Observed rate of single and double events in CZTI during GRB 160623A. The blue solid line (plotted against the right axis) is obtained from the detected single events. The events satisfying the Compton criteria (plotted against the left axis) are shown in black and the red data points (plotted against the left axis) are double events not satisfying the Compton criteria. The region between the dashed vertical lines in the light curve marks the prompt emission phase of GRB 160623A. The Compton events within this region are used for further analysis.

3.3 AstroSat mass model

Polarization analysis of off-axis sources is challenging as the polarization properties of photons are affected due to the interactions with satellite elements and CZTI housing elements. These interactions are highly direction and energy dependent. To account for this we modelled the entire AstroSat with accurate chemical and geometrical properties inside Geant4 (GEometry ANd Tracking) simulation [68] including all the payloads of AstroSat: SSM, UVIT, SXT, LAXPC, CZTI and the satellite bus. The mass model is essential to model the effect of the surrounding material on unpolarized and polarized radiation. We modeled the payload and satellite bus geometries as accurately as possible. Some elements of the geometry are coded using the GEANT4 geometry classes while for the complex structure we used the Cadmesh interface [92] to import the CAD models into Geant4 detector construction. Figure 3.2 shows the mass model of AstroSat simulated in Geant4. The mass model of CZTI and the physics codes had been extensively validated during ground calibration of the CZTI pixels and polarization experiments with on-axis calibration sources [65]. The Geant4 geometry of other instruments (LAXPC, SXT, UVIT, SSM) and spacecraft were included at a later date after the launch of AstroSat. However, these geometries are based on the actual CAD models and hence are expected to be highly accurate.

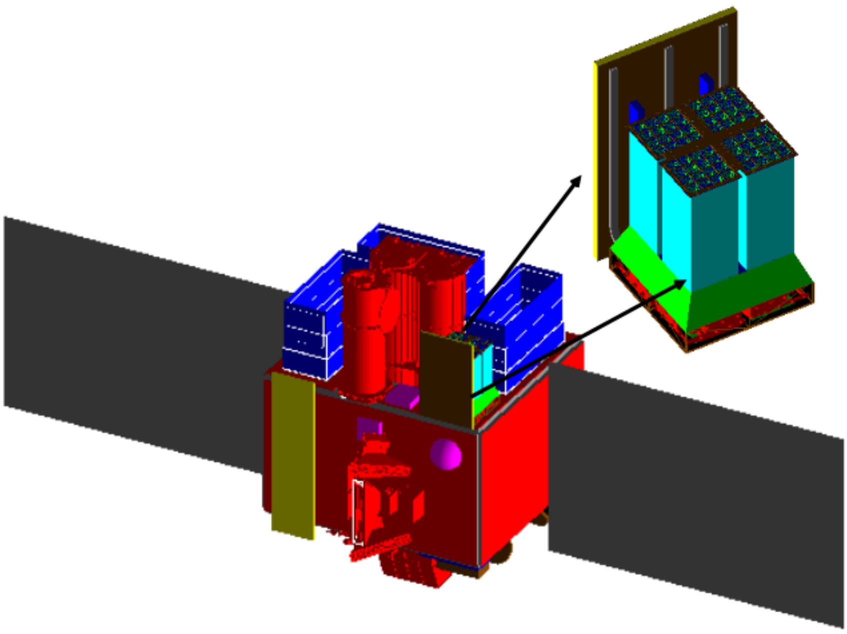

Figure 3.2: Mass model of AstroSat simulated in Geant4 with zoomed in view of CZT-Imager.

3.4 Polarization Estimation

In order to obtain the distribution of azimuthal scattering angles for the GRB photons, through which the polarization signature is derived, we first generate 8-bin azimuthal angle distributions for combined background and GRB events (e.g. the Compton events contained within the vertical dashed lines in Figure 3.1). The azimuthal angle distribution for background events alone is then subtracted from the total distribution to obtain the source distribution. The background distribution is obtained by averaging the pre-GRB and post-GRB azimuthal count distributions. The azimuthal angle for a given valid event is defined with respect to the X axis on the CZTI plane (perpendicular to the radiator plate) in anti-clockwise direction when viewed from the top. The background subtracted azimuthal angle histogram for GRB 160821A, as an example, is shown in Figure 3.3 (left) in black. We see a significant difference in the count rate detected by the edge pixels (angular bin 0°, 90°, 180° and 270°) and the corner pixels (angular bin 45°, 135°, 225° and 315°). This is due to the unequal solid angles subtended by the edge and corner pixels to the central pixel [66]. It is to be noted that the azimuthal angle distribution for any off-axis source is supposed to differ significantly from that for an on-axis source. This is because of the break in symmetry of the pixel geometry with respect to the incident photon direction. This complicates the overall shape of the azimuthal angle distribution. However both these effects can be taken care of by normalizing the azimuthal distribution of the GRB by that for a 100% unpolarized radiation, of the same spectrum and incident at the same off-axis angle as the source. The corrected distribution for the polarized photon count can be obtained using equation 2.1. We obtain U_i or the unpolarized distribution by simulating 100% unpolarized incident radiation with the AstroSat mass model at the same angle of incidence and with the same spectrum as the observed GRB. The red line in Figure 3.3 (left) shows the raw azimuthal unpolarized distribution, whereas the black histogram, in right panel, shows the modulation curve for the GRB following the geometry correction. The error bars in the modulation curve represent the 1σ uncertainties in each bin which are mostly dominated by the statistics of low photon counts during the GRB prompt emission and the uncertainty in estimating the background azimuthal distribution.

3.5 Results

The modulation curves for all GRBs are obtained in the energy range $\sim$100–300 keV. We see a clear polarization signature in most of the GRBs, while for a few GRBs, lack of sufficient number of photons leads to a large uncertainty in the estimated modulation amplitude and the polarization angle. The fitted values of the modulation amplitudes and polarization angles are given in the text inside the figures along with the estimated uncertainties. The green dashed lines are the simulated modulation for 100 % polarized radiation for the GRBs at the observed polarization angles respectively. Except for GRB 160325A and GRB 160802A, all the GRBs manifest a single broad pulse. These two GRBs show two clear pulses in their light curves. The modulation curves shown here are for the combined Compton events from the both the peaks in order to enhance the signal to noise ratio. However we have seen no significant change in the modulation amplitudes and polarization angles across the pulses in both the GRBs. It is to be noted that previously we presented polarization analysis for GRB 151006A in Rao et al 2016 [67]. The analysis was done without the use of detailed AstroSat mass model. With the implementation of the mass model the new result is more accurate and the estimated modulation amplitude is slightly less than that reported earlier. It

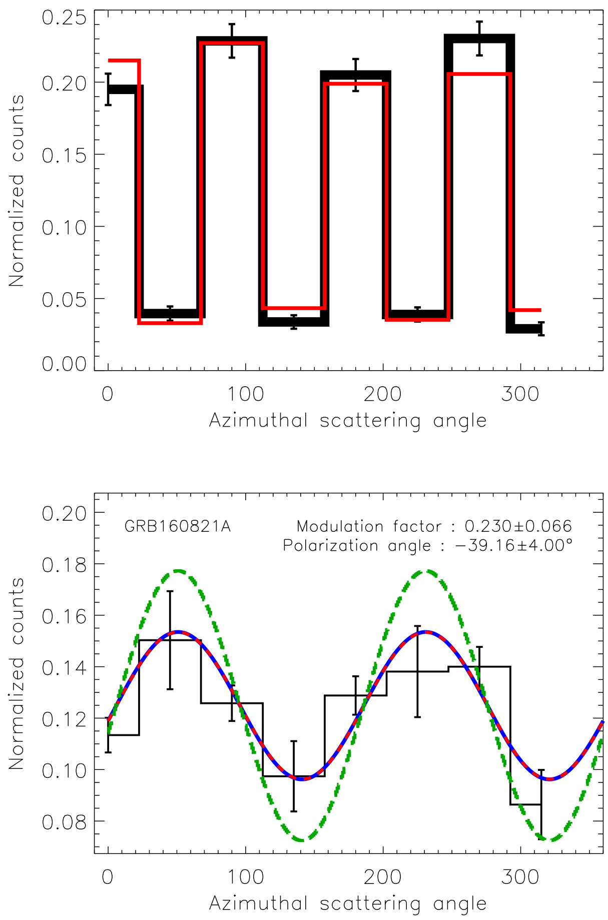

Figure 3.3: Left: background subtracted raw eight bin azimuthal angle distribution for GRB 160821A obtained from the Compton events (∼100–300 keV) are shown in black. The error bars are the Poisson error on each azimuthal bin for 68% confidence level. The azimuthal distribution shown in red is that obtained by simulating unpolarized incident radiation from the same GRB. Right: the geometrically corrected modulation curve for GRB 160821A. The blue solid line is the sinusoidal fit to the modulation curve while the red dashed line is obtained from an MCMC method for a modulation amplitude ∼0.23 with a detection significance $>3\sigma$ (one parameter of interest at 68% confidence level) and a polarization angle ∼-39° in the CZTI plane.

is to be noted that we do not see any significant modulation for GRB 160623A in the full energy range of 100–300 keV. The modulation amplitude is estimated to be low with large uncertainties on both modulation amplitude and polarization angle, signifying that the radiation is unpolarized or has low polarization in 100–300 keV band. Interestingly, at energies below 200 keV, we find significant modulation in the azimuthal angle distribution for GRB 160623A. It is either due to a change in the polarization angle or unpolarized nature of the radiation at higher energies, which leads to a net low polarization in the full 100–300 keV band. Currently, it is not possible to distinguish these two scenarios due to poor statistics at higher energies. Figure 3.4 shows the modulation curves for the remaining 10 GRBs.

Polarization fraction is estimated by normalizing the estimated modulation amplitude with μ_{100}. We estimate μ_{100} from the Geant4 simulations of AstroSat mass model. μ_{100} depends on the energy of the photons, polarization angle, and the incidence direction. Chattopadhyay et al 2014 [66] describe the dependence of μ_{100} on photon energy and polarization angle for on-axis sources. Higher values of μ_{100} are expected when the polarization is along the corner pixels, whereas μ_{100} is low when it is aligned along the edge pixels. For off-axis angles, we find that the dependence of μ_{100} on polarization angle is not as significant as for on-axis sources. μ_{100}, however, strongly depends on the incident direction of the photons. For larger off-axis angles, value of μ_{100} is found to be lower than those for smaller off-axis angles. In order to take these effects into account, we estimate μ_{100} by simulating the same GRB spectra at the same viewing angle for the observed polarization angle. Values of PF and PA for the 11 bursts (upper limit for 5 GRBs) are given in Table 3.1. We note that the sky polarization angles (after converting the polarization angles in CZTI plane to the sky frame) are randomly oriented in the full angle space of 0–180° as expected for a large sample. We see that most of the GRBs are highly polarized, corroborating earlier reports for a few GRBs by RHESSI, INTEGRAL and GAP. For GRB 160106A, GRB 160131A, GRB 160802A, GRB 160821A and GRB 160910A, the polarization fractions are estimated with $\gtrsim 3\sigma$ detection significance (for 1 parameter of interest at 68%

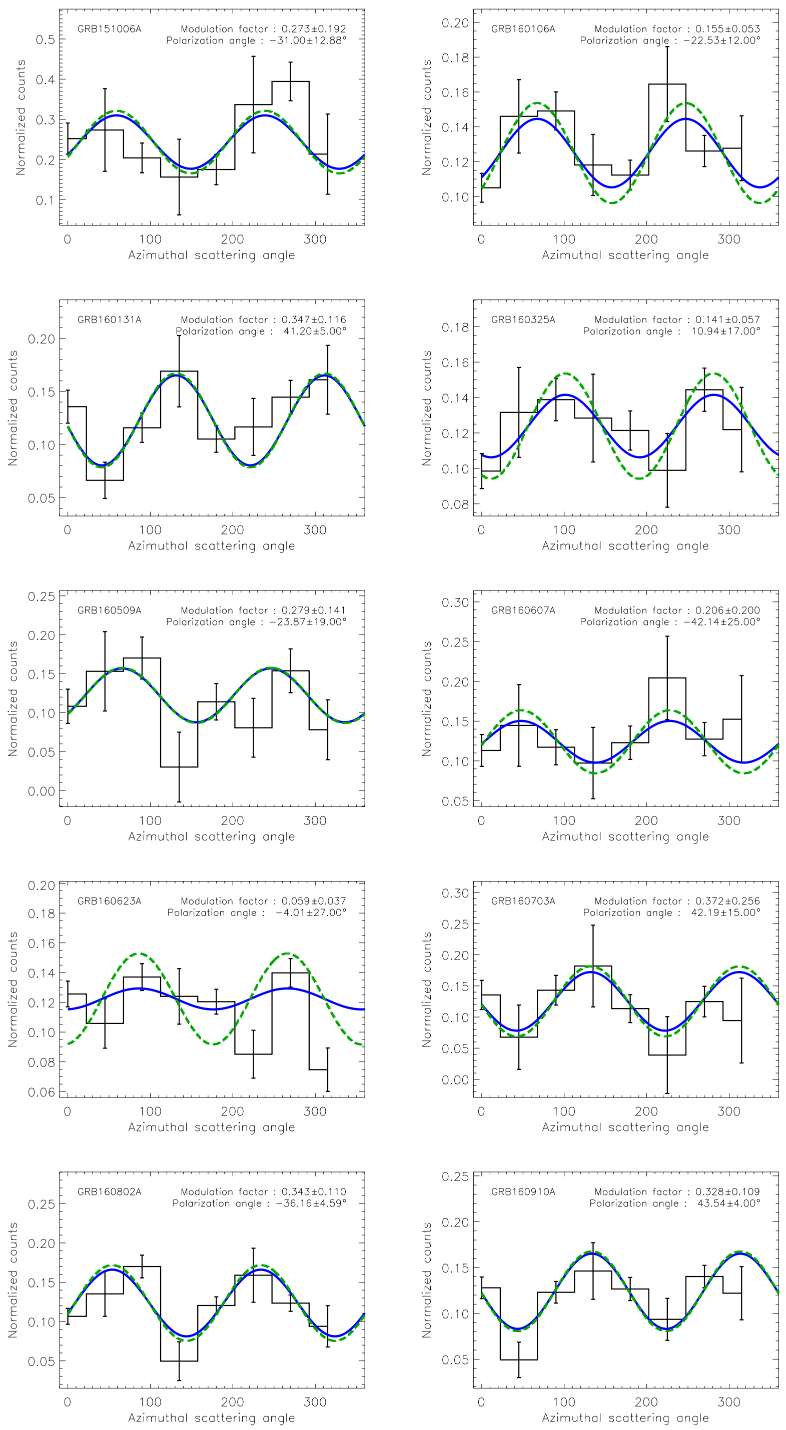

Figure 3.4: Geometrically corrected modulation curves (similar to 3.3 right panel) for the remaining 10 GRBs. The blue solid line is the sinusoidal fit to the modulation curve while the green dashed line is the simulated azimuthal distribution for 100 % polarized radiation for the same observed polarization angle. Values of modulation factor and polarization angle shown in text are obtained from MCMC simulations. The uncertainties are obtained for one parameter of interest at 68 % confidence level.

confidence level). On the other hand for GRB 160325A, polarization fraction is constrained within $\sim 2.2\sigma$ significance.

Table 3.1: Measured polarization fractions (PF) and position angles (PA) for the GRBs

GRB Name	N_{compt}	PF (%)	CZTI PA (°)	sky PA (°)
GRB 151006A	459	<84 ($\alpha = 0.05, \beta = 0.5$)	-	-
GRB 160106A	950	69±24	-23±12°	108±12°
GRB 160131A	724	94±33	41±5°	87±5°
GRB 160325A	835	59±28	11±17°	158±17°
GRB 160509A	460	<92 ($\alpha = 0.05, \beta = 0.5$)	-	-
GRB 160607A	447	<77 ($\alpha = 0.05, \beta = 0.5$)	-	-
GRB 160623A	1400	<46 ($\alpha = 0.05, \beta = 0.5$) <57 ($\alpha = 0.01, \beta = 0.5$)	-	-
GRB 160703A	448	<55 ($\alpha = 0.05, \beta = 0.5$) <68 ($\alpha = 0.01, \beta = 0.5$)	-	-
GRB 160802A	901	85±30	-36±5°	147±5°
GRB 160821A	2100	54±16	-39±4°	25±4°
GRB 160910A	832	94±32	44±4°	46±4°

3.6 Summary

This chapter described the polarimetric analysis method for GRBs using the CZTI instrument of AstroSat and presents the prompt emission polarization measurements for 11 bright GRBs detected during the first year of operation of CZTI. A good polarization measurement in hard X-rays is very difficult due to two reasons: firstly, the measurements are prone to high systematic errors and secondly, the measurement itself is of extreme photon starved nature. For the measurement of the polarization of the prompt emission of GRBs, both these aspects are significantly amplified due to the short duration of the prompt emission and the unknown position of the GRBs. These aspects are evident from the fact that despite multiple efforts for more than a decade and a half, there has not been any firm detection of polarization apart from a few measurements made by POLAR [91] and GAP [88, 89]. In most cases (about 10 GRBs), only some hints of polarization have been reported (RHESSI: [93], IBIS: [86, 87], SPI: [94, 95, 84], BATSE: [96], AstroSat: [67, 37, 97, 98], see review by [49]) and in many cases the measurements are of not very high significance. In this context, the present work is of considerable significance because it has almost doubled the number of GRBs with measured polarization in its first year of operation. Similar measurements have been carried out for a number of additional GRBs and will be reported later. It is to be noted that POLAR has stopped operating in 2017 and there are currently no GRB polarimetric mission scheduled in near future. This makes the measurements from CZTI even more important. An important point to note here is that the results presented here (or GRB polarization measurement with CZTI in general) critically depend on the simulation for unpolarized and polarized radiation through the AstroSat satellite. For this purpose, we have made the AstroSat mass model, painstakingly collecting the details of all parts and materials gone into making the satellite. This is implemented in the Geant4 code and the resultant products (DPH, spectra, localization) are shown to agree quite well with the real data. The residual systematics from the mass model might contribute towards the estimation of the μ_{100} but it may not have significant effect on the detection of polarization. We find most of the bursts to be highly polarized, implying either synchrotron emission in a time independent ordered magnetic field or Compton drag as the mechanism for the prompt emission. However, in order to draw such 'firm' conclusions, it is necessary to have much larger sample. Given the fact that most of the GRBs in the present sample are moderately bright, CZTI is expected to continue GRB polarization measurements at a similar rate for several years to come. Availability of a large number of such measurements from CZTI is likely to significantly enhance our understanding of the GRB prompt emission.

Chapter 4

Experimental verification of off-axis polarimetry with Cadmium Zinc Telluride detectors of AstroSat-CZTI

The polarization measurement capability of CZTI for on-axis sources was experimentally confirmed using polarized and unpolarized X-rays before launch [65]. This enhances the confidence in polarization measurements of pointed observations post launch. In chapter 2 we discussed the interesting results on the X-ray polarization of the Crab nebula and pulsar in the energy range of 100 – 380 keV. CZTI has also contributed to the measurement of prompt emission polarization for 11 GRBs, the results of which are discussed in chapter 3. However, polarization measurements of off-axis sources like GRBs are challenging and they significantly depend on simulations. Hence, it is important to ensure experimentally, that CZTI is sensitive to measure the polarization of X-rays (polarized and unpolarized) incident from a direction off-axis to the detector. Experimental confirmation for such off-axis polarimetric capability are not available for non-dedicated GRB polarimeters including AstroSat CZTI. Nevertheless, this is an essential factor in enhancing the credibility of the measurements. In this context, we report the verification of the off-axis polarimetric capability of pixelated CZT detectors through controlled experiments carried out with the qualification model (QM) of the CZTI instrument as well as extensive Geant4 simulations of the experimental setup. We have also employed an alternate goodness of fit reduced χ^2 method in the polarization analysis.

4.1 Introduction

For fast transient sources such as GRBs, sensitive X-ray polarization measurements are likely to remain impervious. In this case, the difficulties of polarization measurements are compounded due to multiple reasons - 1. They last only for a short duration ranging from few seconds to at the most few minutes. 2. Their occurrence is random both in space and time. All X-ray polarimeters measure the azimuthal distribution of scattered photons/electrons with respect to a reference direction. Since GRBs occur at varying angles with respect to the instrument reference direction, the polarization measurements are highly prone to the systematic effects. Besides, the short duration GRBs result in a limited number of photons. Thus, measuring polarization of the GRB prompt emission is a challenging task.

CZTI measured polarization of 11 GRBs during its first year of operation 3. Impact of the CZTI measurements can be seen from the fact that polarization measurements were available for only 10 GRBs before the launch of AstroSat.

One important objective of GRB polarimetry is to have a sufficiently large sample of GRBs with definite polarization measurements, which can then be used to distinguish between various prompt emission models [47]. In this context, continued GRB observations with CZTI are likely to play a significant role in the field. Since the launch of AstroSat in September 2015, CZTI has detected more than 250 GRBs [99]. Polarization analyses have been carried out for bright GRBs having a sufficiently large number of Compton events that is adjacent double pixel events satisfying Compton criteria [66]. Geant4 [68] simulations are used to obtain the geometric corrections based on the simulation for unpolarized photons as well as to estimate the polarization fraction based on the simulation for 100 % polarized photons, both incident from the direction of the GRB. The availability of accurate background measurements before and after the GRB emission is a major advantage in GRB polarization measurements. Further, GRBs are often detected well above the average background, and hence the signal to background ratio is much better during GRB compared to that of conventional X-ray source like Crab. However, unlike persistent sources, GRB polarization analysis rely more on Geant4 simulations. Hence it is important to verify the off-axis polarization capability of CZTI detectors experimentally.

In this chapter we present the experimental validation of hard X-ray off-axis polarization measurement capability of the pixelated CZT detectors as well as the efficacy of the Geant4 simulations that are required for the polarization analysis. Section 4.3 shows the implementation of the new goodness of fit method in the C19 reported sample of GRBs. Section 4.4.1 describes the experimental set up used for the off-axis validation, followed by section 4.4.2 that describes the Geant4 simulations used to obtain the reference grid (4.4.2) as well as the simulation of the experimental set up used for direct comparison with experimental modulations (4.4.2). Section 4.5 discusses the results of experiments and simulations. Finally, section 4.6 summarizes the key findings of the present work.

4.2 Polarization Analysis using χ^2 method

We follow the same procedure to identify the Compton events and respective azimuthal angles as described in section 2.2.1. Raw azimuthal distribution is obtained from the histogram of the scattering angle of Compton events. Background subtraction is performed with the raw azimuthal histogram obtained for each observation. Considering a 3×3 matrix of pixels with the center pixel being the scatterer, the solid angle covered by edge pixels is larger than that for corner pixels, and hence more number of photons are detected in edge pixels. Hence, the raw azimuthal distribution requires a correction for this geometric effect. One way of geometry correction is by using the modulation of unpolarized radiation, which can be obtained through simulations. This method is used in C19 to report polarization measurements of 6 GRBs and upper limits on 5 GRBs. But there have been some concerns about the geometry correction method as the off-axis modulation curves are not expected to be sinusoidal [100]. Hence, here we use an alternate goodness of fit χ^2 method of directly comparing the observed uncorrected azimuthal histograms with the expected uncorrected histograms obtained from Geant4 simulations for a grid of Polarization Fractions (PF) and Polarization Angles (PA), similar to that used for the analysis of GRB polarization from the POLAR experiment [91]. This method requires a library of azimuthal histograms for all possible PFs and PAs from a given incident direction, which is generated using Geant4 simulations, as discussed in section 4.4.2. The observed azimuthal histogram is directly compared with each of the 8 bin simulated azimuthal histograms of the library, to obtain the χ^2 value between the measured and simulated modulation as given by:

$$\chi^2 = \sum_{i=1}^{8} \frac{(M_{obs} - M_{sim})^2}{(\sigma_{obs}^2 + \sigma_{sim}^2)} \tag{4.1}$$

and $\Delta\chi^2$ is defined as,

$$\Delta\chi^2 = \chi^2 - \chi_{min}^2 \tag{4.2}$$

Here $\mathrm{M_{obs}}$ and $\mathrm{M_{sim}}$ are observed and simulated modulations respectively and σ_{obs} and σ_{sim} are the corresponding errors. The results are shown in the form of contour plots for PF and PA, and the minimum value of χ^2 over the full range of PF and PA gives the best estimate of the actual PF and PA. The error estimates for PF and PA are obtained from the two parameter confidence levels for the χ^2 distribution with $\Delta\chi^2 = 2.28$, 4.61 and 9.21 for the 1σ, 2σ and 3σ confidence levels.

4.3 GRB Polarimetry with CZTI using χ^2 method

In this section, a few bright CZTI GRBs are reanalyzed by following the χ^2 method. C19 reported polarization of a sample of 11 GRBs, detected by CZTI over the energy range of 100 – 350 keV. C19 followed the geometry correction method using unpolarized radiation (using photon indices of respective GRBs as input) obtained using the AstroSat mass model. From the sample of C19, few bright GRBs are chosen, and polarization analysis using the GRB and background time stamps used in C19 are performed by following the goodness of fit χ^2 method. The 100% polarized and unpolarized modulations are obtained by shining the photons following a power law over energy range 100 – 400 keV (with photon

Table 4.1: Measured PF and PA values for bright CZTI GRBs, following goodness of fit χ^2 method are listed in columns 2 and 3. Along with the current results, C19 and S19 reported PF and PA values are given for reference.

GRB	PF (%)	PA (°)	C19 PF [101] (%)	C19 PA [101] (°)
GRB160131A	98^{+2}_{-17}	81^{+5}_{-23}	94±33	87±5
GRB160325A	45^{+36}_{-38}	166^{+5}_{-45}	59±28	158±17
GRB160802A	78^{+19}_{-28}	157^{+3}_{-9}	85±30	147±5
GRB160910A	97^{+3}_{-15}	49^{+2}_{-2}	94±32	46±4
GRB	PF (%)	PA (°)	S19 PF [102] (%)	S19 PA [102] (°)
GRB160821A Time bin 1	86^{+14}_{-13}	137^{+12}_{-11}	71^{+29}_{-41}	110^{+14}_{-15}
GRB160821A Time bin 2	57^{+38}_{-34}	63^{+14}_{-4}	58^{+29}_{-30}	31^{+12}_{-10}
GRB160821A Time bin 3	66^{+34}_{-33}	117^{+14}_{-9}	61^{+39}_{-46}	110^{+25}_{-26}
GRB160821A Total	38^{+26}_{-26}	104^{+14}_{-41}	21^{+24}_{-19}	-

index and Epeak of corresponding GRB) over the AstroSat mass model. The library of PF - PA grid points (in detail in section 4.4.2) is obtained for each GRB using 10 million incident photons and following equations 4.1 and 4.2, $\Delta\chi^2$ grids are computed. The PF and PA values corresponding to the $\Delta\chi^2{}_{\mathrm{min}}$ value with 1σ error bars are listed in Table 5.1. GRB160821A is the brightest of the C19 sample of GRBs and showed a swing in the PA across the GRB time. S19 reported PA and PF by dividing the GRB time over three time bins (Time since GBM trigger 115-129 s, 131-139 s, 142-155 s), whereas the GRB is unpolarized for the overall time (115-155 s). Figure 5.1 shows the confidence contours obtained for three time bins of GRB160821A and for the total GRB time. PAs and PFs obtained match with S19 reported values and the PA of bin 2 matches with S19 within the 2σ confidence level. The polarization values obtained in the current work by following the goodness of fit method, match well with the results of C19 and S19 (Table 5.1).

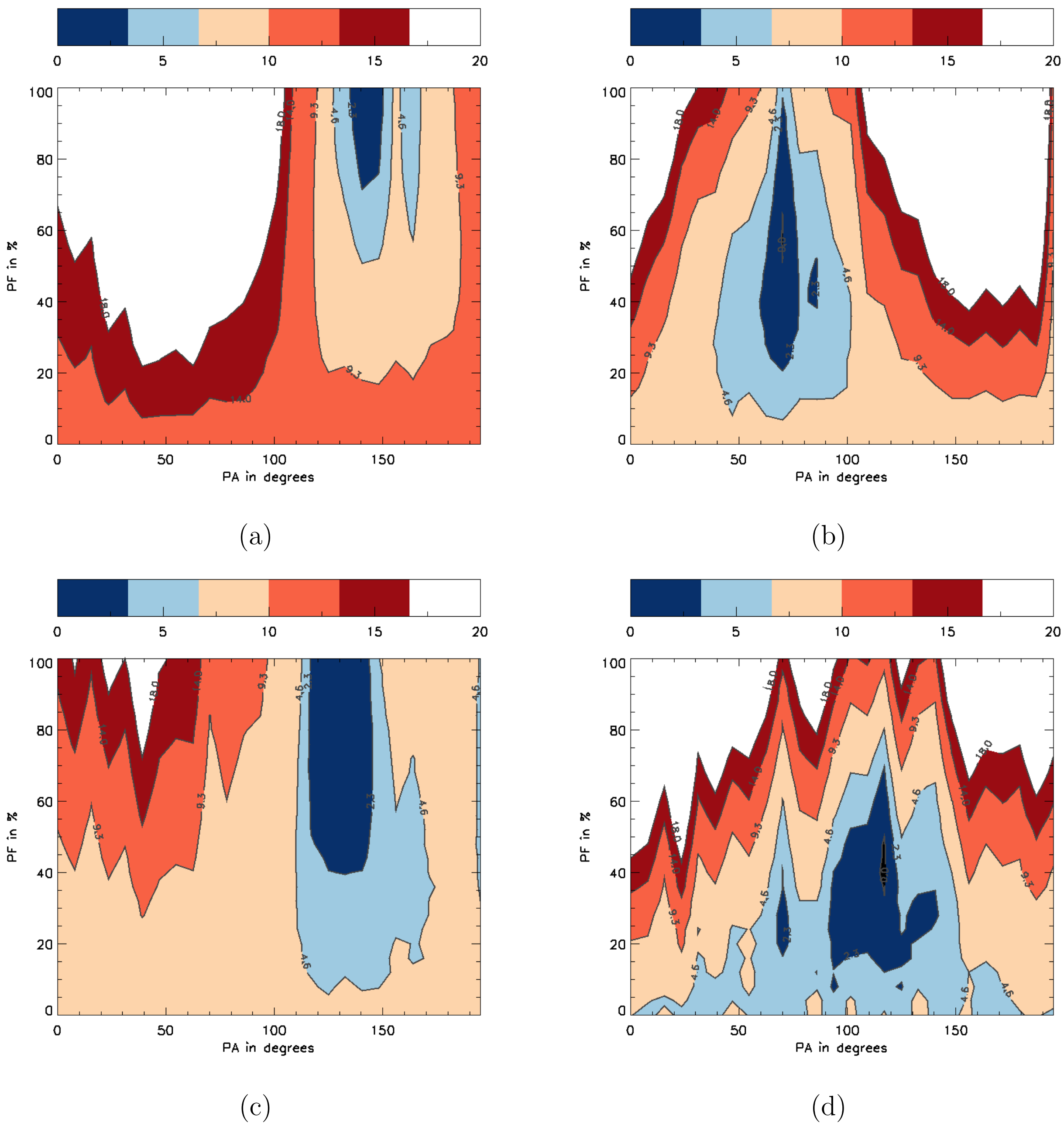

Figure 4.1: The plots represent the $\Delta\chi^2$ contours obtained for (a) GRB160821A Time bin 1 - PF = 86^{+14}_{-13}%, PA = 137^{+12}_{-11} ^{o} (b) GRB160821A Time bin 2 - PF = 57^{+38}_{-34}%, PA = 63^{+14}_{-4} ^{o} (c) GRB160821A Time bin 3 - PF = 66^{+34}_{-33}%, PA = 117^{+14}_{-9} ^{o} , and (d) GRB160821A Total - PF = 38^{+26}_{-26}%, PA = 104^{+14}_{-41} ^{o}

4.4 Off-axis polarization experiment using CZT detectors

CZT detectors are proven to measure polarization of on-axis sources over an energy range of 100 – 400 keV by V15 [65]. CZTI is composed of four identical quadrants, each having 16 CZT detector modules, and one of the modules of the CZTI flight model was used for the experimental verification of the on-axis polarimetric capability reported by V15 [65]. In this work, we extend this experimental validation to off-axis sources. Details of the experimental configuration and Geant4 simulations are discussed.

4.4.1 Off-axis polarization experimental setup

The qualification model (QM) of CZTI is used for the off-axis experiments. The CZTI QM is identical to the flight model with an exception that only one quadrant has active CZT detectors. Also, these detector modules are of slightly inferior quality, in terms of noisy pixels, energy resolutions, and so on; as the best ones were used for the flight model. The first task was to evaluate the performance of all 16 CZT modules to select the best module for further experiments. This was achieved by carefully measuring long duration background at a controlled temperature of 16°C as well as measuring gain and energy resolution for all pixels using radioactive sources ^{241}Am, ^{133}Ba and ^{57}Co. Based on these measurements, the best detector module was selected for all further polarization experiments. Partially polarized X-rays for the polarization experiment were produced by $\sim$90 degree scattering of 356 keV line from ^{133}Ba radioactive source. We used the same arrangement as that used in V15, where a 6 cm long aluminum cylinder inside a 4 cm thick lead enclosure was used as a scatterer. A slit of 5 cm length

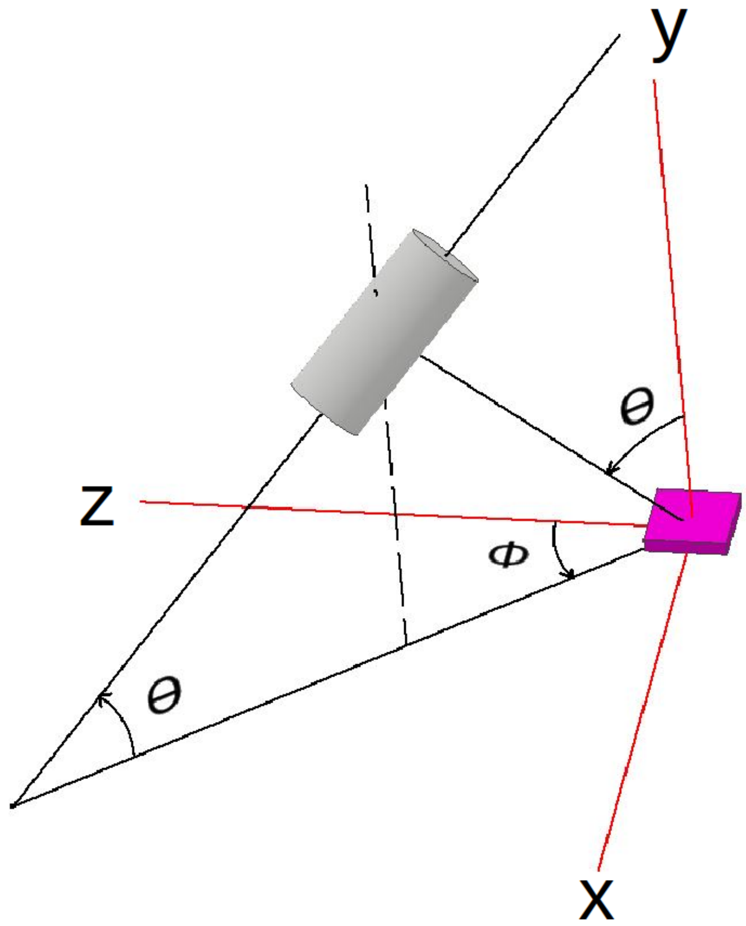

Figure 4.2: Definition of θ, ϕ of the source (grey) with respect to the detector (pink).

and 2 mm width allowed the partially polarized X-rays to exit the enclosure in one direction. The geometry of this arrangement allowed scattering of $90^{o} \pm 15^{o}$ resulting in the partially polarized X-rays with energy range of $\sim$190 keV to $\sim$240 keV.

First, we repeated the on-axis polarization measurement to ensure that the results reported by V15 can be reproduced. In these experiments, the lead cylinder was kept over the coded mask with the PA set to 0^{o}, 45^{o} as well as intermediate values of 10^{o} and -15^{o} with respect to the CZTI detector coordinates. The results were found to be consistent with V15. After end-to-end verification of the on-axis

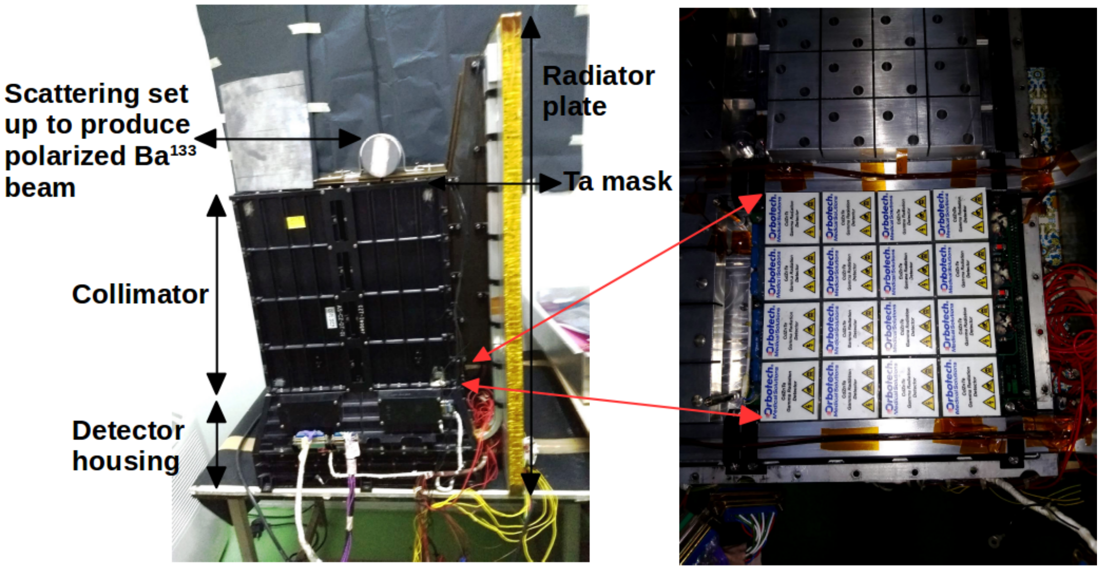

(a) (b)

Figure 4.3: The images depicts the experimental set up used for the off-axis validation. (a) shows a side view of CZTI QM with the partially polarized source configuration kept above the collimator for on-axis experiments (b) shows the top view of QM, 16 Orbotech CZT detectors after the removal of collimators.

polarization measurement, which included a completely independent implementation of the analysis software, we proceeded for the off-axis experiments. Here, the major challenge was to devise a method to place the heavy lead cylinder at a precise position and orientation to achieve the desired off-axis angles, the polar angle θ and the azimuthal angle ϕ (see figure 5.2 for definitions of these angles) while ensuring that the partially polarized X-ray beam is centered at the selected CZT detector module. A special setup as shown in figure 5.4 was fabricated surrounding the QM of CZTI, which allowed any required placement of the lead cylinder as well as in-place rotation of the cylinder to achieve different PAs. With this setup, we attempted the first round of off-axis measurements for three different values, each for θ and ϕ. A major problem encountered was the very low Compton count rate from the polarized X-ray source. The background count rate in the controlled laboratory conditions was $\sim$0.9 counts/s, whereas with the polarized source maximum count rate achieved was ∼1 count/s. Such a low signal-to-noise ratio was due to two reasons: 1. increased distance of the source and 2. possible attenuation of the incident X-rays in the collimator structure of the CZTI instrument. Since the main objective of our experiments was to verify the off-axis polarization measurement capability of the basic CZT detector modules, we decided to remove the collimator structure of the CZTI in order to mitigate both these issues. This resulted in good improvement in the source count rate to ∼15 counts/s. The exposure time required for a given θ and ϕ angle was of the order of 10 hours. As a result, and due to few other practical limitations, we obtained measurements for three polar angles ($\theta = 30^{o}$, 45^{o} and 60^{o}) for the azimuthal angle $\phi = 0^{o}$, but for each of these, we measured two different incident PAs of 0^{o} and 20^{o}. For $\theta = 45^{o}$, we also carried out measurement for $\phi = 45^{o}$ and PA of 45^{o}. It should be noted that the PA mentioned here is in the sky plane and not with respect to the CZT detector coordinates. For each measurement, data were recorded in the form of individual event list by the ground checkout system used to operate the CZTI QM. It was then converted into the standard CZTI level-0 format, and the regular CZTI data pipeline was used for further filtering to obtain clean event files.

4.4.2 Geant4 simulations

Geant4 simulations are an integral part of X-ray polarization analysis. The modulation factor μ_{100} for any X-ray polarimeter is typically obtained from the Geant4 simulations incorporating the exact instrument geometry. In the case of polarization analysis with CZTI for X-rays incident on-axis, the Geant4 analyses have been reported and extensively validated by C14 and V15. We use the same basic methodology for present simulations, including detector geometry, physics processes, event processing as well as further data analysis, to finally record the azimuthal histogram in detector plane. However, in terms of the overall experimental geometry and incident photon directions, we employ two different types of Geant4 simulations.

Generation of the modulation curve library

In the first set of Geant4 simulations, we generate a polarization grid of azimuthal histograms for comparison with the observed histogram by illuminating the CZT detector directly with 100% polarized and unpolarized X-rays. The incident X-ray photons are in the form of parallel beam from the direction given by polar and azimuthal angles θ and ϕ with respect to the detector plane. The energy of the individual photons is randomly sampled within an energy range of 190 keV to 240 keV, in case of simulations for analysis of experimental data. For each incident direction, the simulations are performed for 100% polarized beam, spanning PAs from 0^o – 180^o at steps of 5^o. In all cases, simulations are carried out for 10 million incident photons, and all resultant valid Compton events are used to obtain azimuthal histogram for 100% polarized X-rays. To obtain the azimuthal histograms for partially polarized X-rays, randomly selected Compton events from the fully polarized simulations are fractionally added to the unpolarized Compton events for every 1% polarization step. This results in a library consisting of 3636 (36 PA bins $\times$ 101 PF bins) raw azimuthal histograms for every incident direction. This library is then used to calculate χ^2 at each point in the PF - PA grid for the observed raw azimuthal histogram, as discussed in the previous section.

Simulation of the full experimental setup

The incident photons from astrophysical sources are in the form of a parallel beam. However, it is challenging to obtain such parallel beams in the laboratory experiments using radioactive sources. In our experiment, the divergence of incident X-ray beam is minimized by using appropriate collimators at the entry and exit points of aluminium scatterer. In order to fully validate through Geant4 simulations for off-axis incidence, it is necessary to include generation of the partially polarized X-rays within the Geant4 setup itself. In this context, we simulated the experimental setup, incorporating the disk type ^{133}Ba radioactive source. The hollow lead cylinder with cap and slit as well as the aluminium scatterer used to produce the partially polarized beam are defined in the exact dimensions by importing a CAD design (using Inventor 2017) using the CADMesh interface for Geant4 [103]. This direct import of the CAD design preserves the relative placement and orientation of various components of the source assembly. However, the placement of the complete source assembly is tricky, as it involves multiple coordinate transformations and rotation matrices. The placement coordinates and orientation of the source plane are calculated separately since it is implemented using General Particle Source (GPS). It has to be placed independent of the rest of the source assembly, with an additional rotation and translation. The energy of the source photons is fixed to 356 keV, which after scattering in the aluminum scatterer results in a partially polarized X-ray beam with appropriate energy range. For each case of θ, ϕ, and PA the simulations are run for $\sim 10^{10}$ photons, after verifying the geometry by visual inspection.

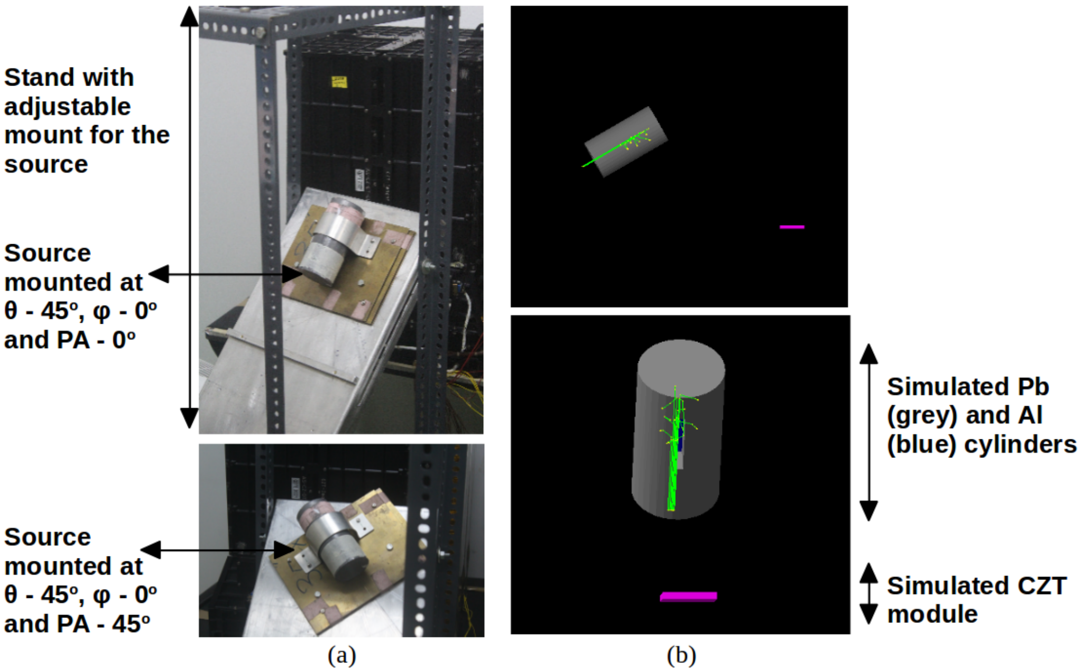

Figure 4.4: The images show the real experimental setup and the experimental setup constructed using Geant4. (a) shows the experimental setup. In the top is the source placed in the experimental setup, mounted over an aluminium slab to place the source at a desired θ and on the bottom is the source tilted for a PA of 45° and (b) shows the simulated CZT module (pink), the lead cylinder along with cap (grey) and the aluminium cylinder used for producing the polarized beam through scattering are constructed in the same dimensions as the ones used in the experiments. The images show the source kept at $\theta = 45^{\circ}$ and $\phi = 0^{\circ}$ with PA $= 0^{\circ}$. The incident 356 keV mono energetic beam (green) could be seen getting scattered by the aluminium cylinder (blue).

4.5 Results and Discussion

The off-axis experiments are performed for 4 sets of θ, ϕ each for 1-2 PAs. For each of these cases an array of 3636 $\Delta\chi^2$ values are calculated as discussed in section 4.2. A systematic error of 5% and 3% are used for the experimental and grid simulation results, respectively. The systematic error in the experiments include the uncertainty in the θ, ϕ arising due to both the errors in the vertical and horizontal distances and the alignment of the aluminium slab for a desired polar angle. The PF and PA values obtained for each configuration (PF_{expt} & PA_{expt}) corresponding to the $\Delta\chi^2{}_{min}$ are listed in Table 5.2. A typical error bar

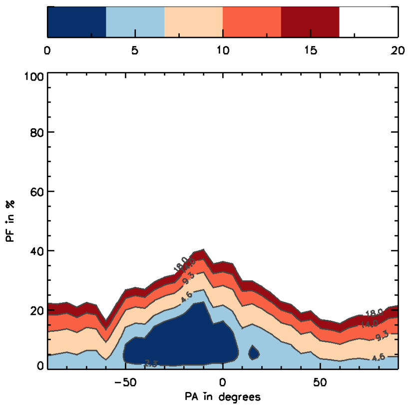

(a)

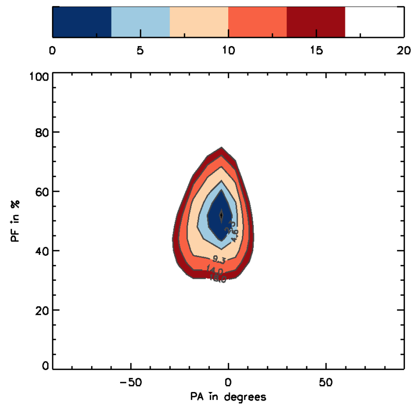

(b)

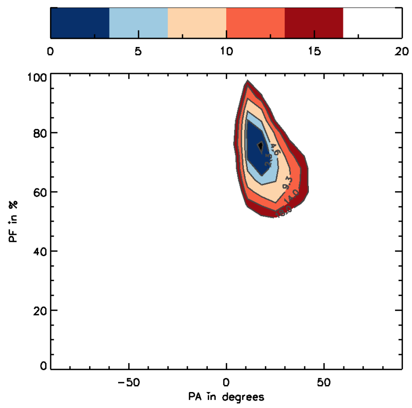

(c)

Figure 4.5: The plots show the confidence contours obtained for off-axis experimental data, where the source is kept at $\theta = 30^{o}$, $\phi = 0^{o}$. The nature of incident radiation are (a)unpolarized (b) polarized with a PA of 0^{o}, and (c) polarized with a PA of 20^{o}.

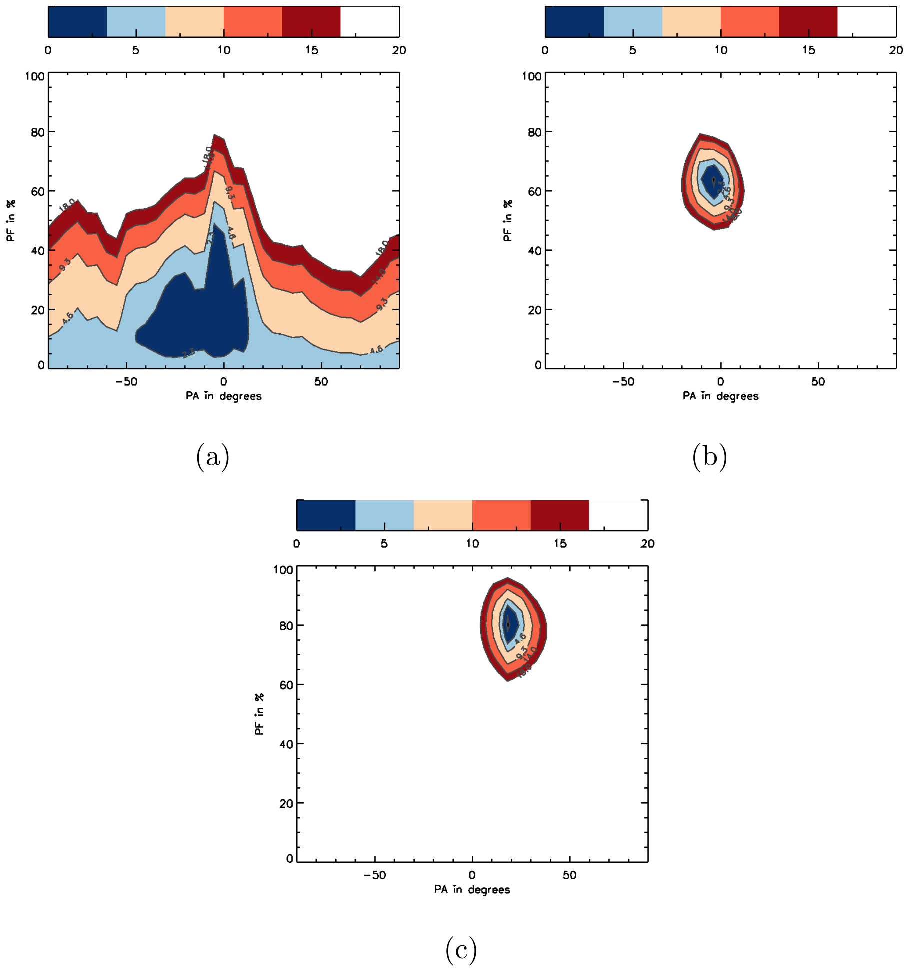

Figure 4.6: The plots show the confidence contours for the configuration $\theta = 45^o$, $\phi = 0^o$. The nature of incident radiation are (a)unpolarized (b) polarized with a PA of 0^o, and (c) polarized with a PA of 20^o.

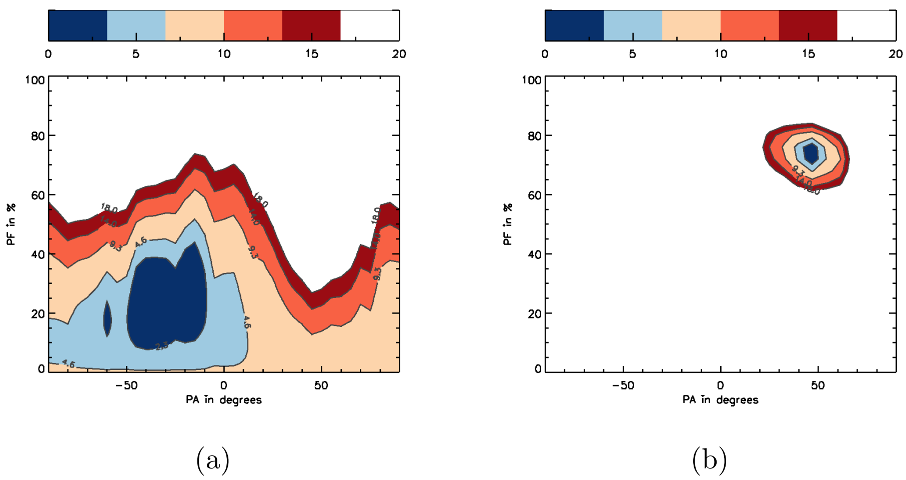

Figure 4.7: The plots show the confidence contours obtained for $\theta = 45^o$, $\phi = 45^o$. The nature of incident radiation are (a)unpolarized and (b) polarized with a PA of 45^o.

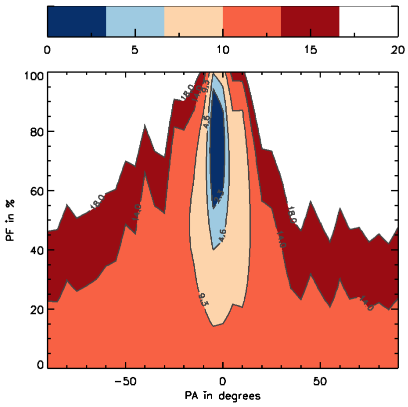

(a)

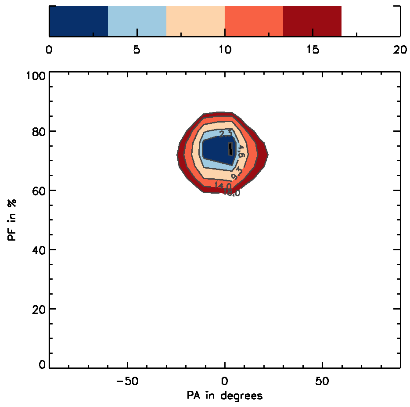

(b)

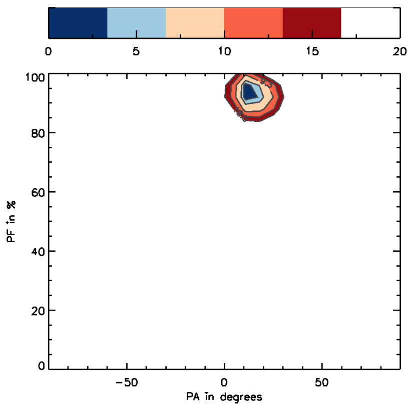

(c)

Figure 4.8: The plots show the confidence contours obtained for $\theta = 60^{o}$, $\phi = 0^{o}$. The nature of incident radiation are (a) unpolarized (b) polarized with a PA of 0^{o}, and (c) polarized with a PA of 20^{o}.

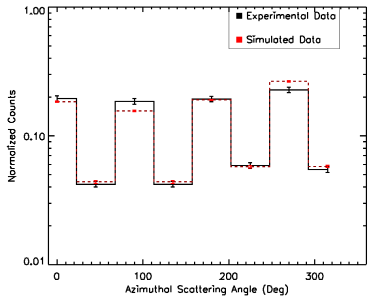

(a)

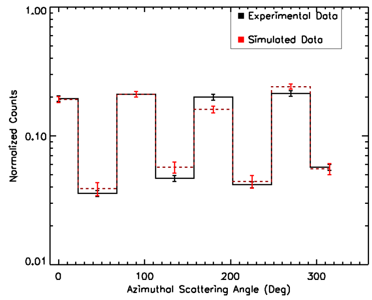

(b)

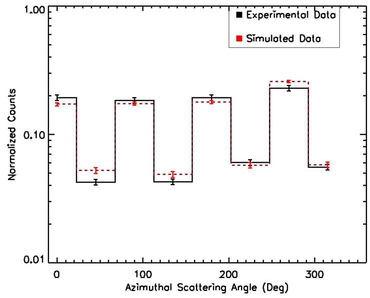

(c)

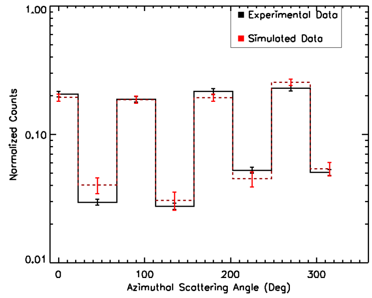

(d)

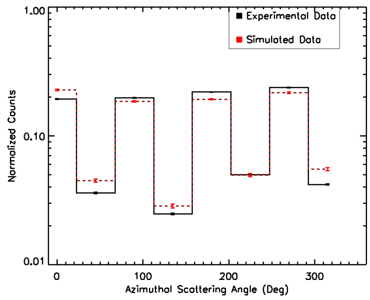

(e)

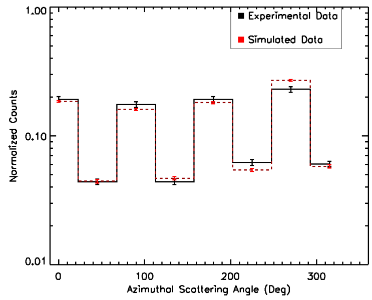

(f)

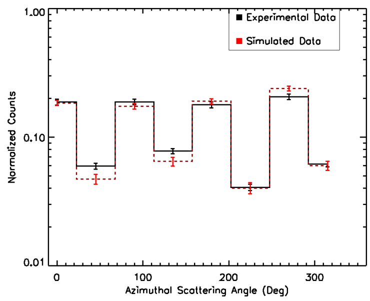

(g)

Figure 4.9: The plots show the comparison of experimental (black) and simulation of experimental set up (red) results for the configurations (a) $\theta = 30^o$, $\phi = 0^o$, PA $= 0^o$ (b) $\theta = 30^o$, $\phi = 0^o$, PA $= 20^o$ (c) $\theta = 45^o$, $\phi = 0^o$, PA $= 0^o$ (d) $\theta = 45^o$, $\phi = 0^o$, PA $= 20^o$ (e) $\theta = 45^o$, $\phi = 45^o$, PA $= 45^o$ (f) $\theta = 60^o$, $\phi = 0^o$, PA $= 0^o$, and (g) $\theta = 60^o$, $\phi = 0^o$, PA $= 20^o$. It could be seen the simulations performed matches well within the error bars for each of the experimental cases.

Table 4.2: The PF and PA values corresponding to the $\Delta\chi^2{}_{\mathrm{min}}$ obtained for off-axis experiments (PA_{expt} & PF_{expt}) and corresponding simulations of experimental set up (PA_{sim} & PF_{sim}).

θ (°)	ϕ (°)	Incident PA (°)	PA_{expt} (°)	PF_{expt} (%)	PA_{sim} (°)	PF_{sim} (%)
30	0	0	0^{+3}_{-8}	52^{+7}_{-8}	0^{+6}_{-3}	40^{+7}_{-8}
30	0	20	15^{+5}_{-5}	75^{+10}_{-8}	10^{+5}_{-5}	78^{+10}_{-11}
45	0	0	0^{+1}_{-5}	63^{+5}_{-5}	0^{+5}_{-6}	65^{+6}_{-7}
45	0	20	20^{+3}_{-5}	80^{+6}_{-5}	10^{+2}_{-8}	79^{+10}_{-12}
45	45	45	45^{+5}_{-2}	74^{+4}_{-4}	40^{+10}_{-10}	60^{+6}_{-6}
60	0	0	0^{+4}_{-6}	74^{+4}_{-5}	5^{+2}_{-5}	74^{+4}_{-3}
60	0	20	15^{+4}_{-5}	93^{+3}_{-3}	15^{+5}_{-5}	84^{+5}_{-3}

of 5° is expected to occur in the incident θ, ϕ and PA. Figures 5.5 and 5.6 show the confidence contours for $\theta = 30°$ and $\theta = 45°$ respectively both at $\phi = 0°$ for incident (a) unpolarized radiation and for polarized cases with (b) PA 0°, and (c) 20°. Figure 5.7 corresponds to incident position of $\theta = 45°$ and $\phi = 45°$ for (a) unpolarized and (b) polarized radiation for PA 45°. Figure 5.8 shows the contours for $\theta = 60°$ $\phi = 0°$ for (a) unpolarized radiation and polarized cases with (b) PA 0° and (c) 20°.

It could be seen from Table 5.2 that PF obtained from experiments are varying with different configurations. In order to validate this, simulations of the experimental set up are performed using Geant4 (section 4.4.2) for each of the experimental configurations (θ, ϕ, and PA). Figure 5.9 shows the 8 bin background subtracted raw azimuthal histogram obtained for each experimental configuration (solid black lines) over plotted with the modulation obtained from corresponding simulations of the experimental set up (dotted red lines). It could be seen from figure 5.9 that the results from simulations match with the experimental results well within the error bars. Similar to experiments, the 3636 $\Delta\chi^2$ values are cal-

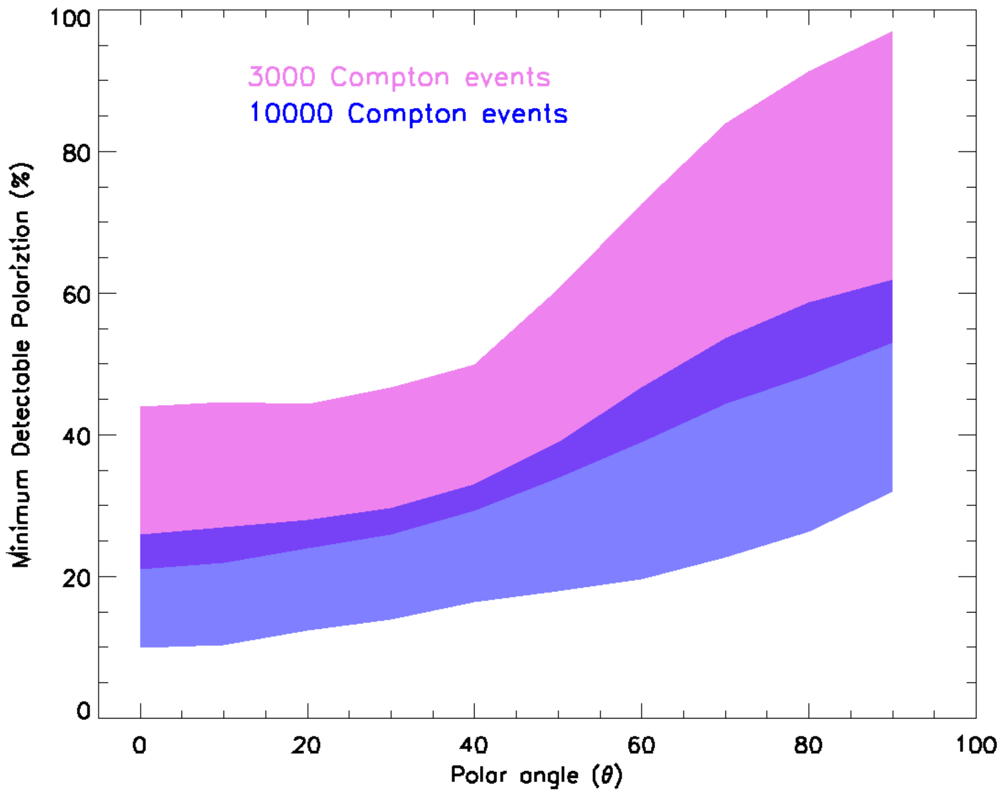

Figure 4.10: Minimum detectable polarization obtained for incident angles θ = 0^o – 90^o for two different cases of Compton events: 3000 (violet) and 10,000 (blue). In both cases, for all five PAs, the corresponding MDP values lie within the violet and blue bands.

culated for each simulated configuration by using corresponding PF - PA grid points. The results of each simulated configuration are listed in Table 5.2 and is found to be matching well with the experimental results. This verifies that the change in PF is not due to any experimental artifact, but could possibly because of varying geometry of the scattered photons reaching the detector in each case. It could also be seen that at larger angles, unpolarized radiation starts mimicking the polarized radiation. This is inherently expected as the detector is sensitive only to the component of polarization in the plane of the detector. The other component is determined by orthogonality condition. At higher incident angles, the component in the detector plane is less. Owing to experimental constraints the polarization capability for $\theta > 60^o$ could not be investigated. To get a quantitative limit on this, a set of simulations are performed using a single CZT module illuminated by 100% polarized and unpolarized beams, both over an energy range 100 – 400 keV with a power-law index of -1.0. The simulations are carried out for incidence angles $\phi = 0^o$ and θ ranging 0^o to 90^o for every 10^o each for 10 million incident photons. The simulations are performed for PA values = 0^o, 30^o, 45^o, 60^o, and 90^o. The total number of Compton events detected in all the cases is of the order of 10^4. To have a realistic scenario, two cases are considered for each simulation point, by randomly selecting 3000 and 10,000 Compton events (N_{comp}). For each polar angle, PA, and N_{comp} case, a grid of χ^2 values are calculated between the 101 polarized modulations and unpolarized radiation. The minimum PF corresponding to which the detected modulation is not unpolarized at a 99% confidence interval is the minimum detectable polarization (MDP). The MDP values are calculated for each θ and PA, corresponding to 3000 and 10,000 Compton events and are plotted in figure 5.10. For all five PAs, MDP values corresponding to 3000 Compton events lie within the violet band, and those corresponding 10,000 Compton events lie within the blue band. From figure 5.10 it is evident that, MDP increases significantly with θ above 60^o. However for $\theta < 60^o$, CZT detectors are well suited for polarization measurements. An ideal situation is to use multiple CZT detectors over a spherical or hemispherical arrangement (as in the proposed Indian mission Daksha, to detect GRB polarization) and using the data from respective detector(s) so that for a given GRB the relative θ lies between 0^o – 60^o.

4.6 Summary

The prompt emission polarization measurements have been carried out for a number of bright GRBs detected with AstroSat-CZTI. Since GRBs occur in random direction, and the polarization analysis involves significant use of Geant4 simulations, it is essential to have experimental verification of the off-axis polarization measurement capability of the pixelated CZT detectors as well as validation of the Geant4 simulations. In this context, we have carried out experiments to estimate the polarization of the partially polarized X-rays generated using laboratory radioactive source kept at different off-axis positions. We also carried out Geant4 simulations of the actual experimental setup, including the generation of the partially polarized beam by $\sim 90^o$ scattering of X-ray photons. The experimentally measured azimuthal histograms match reasonably well within the error bars with the simulated histograms, suggesting that the CZTI can measure polarization of the off-axis sources and that the Geant4 simulations reliably reproduce expected results. We estimated the polarization fraction and polarization angle using a different technique of goodness of fit. We also verified that this technique does reproduce the polarization results for GRBs reported in C19 and S19 and find that this method can be used for lower signal-to-noise ratio measurements as well. Our experiments show that pixelated CZT detectors can be used for measuring prompt emission polarization measurements for incident direction $\theta < 60^{\mathrm{o}}$ from the normal. The same detectors are being considered for a proposed mission called Daksha, which is dedicated to GRB and EM-counterparts of the gravitational wave sources. Daksha will have a significantly larger effective area than AstroSat-CZTI, and our results indicate highly promising prospects of polarization measurements of a large number of GRBs with such a dedicated mission.

Chapter 5

NICSPol: A Near Infrared polarimeter for the 1.2 m telescope at Mount Abu Infrared Observatory

In chapter, (2) polarization results of Crab in the hard X-ray regime with respect to phase values are discussed. Few reports of Crab polarization that exist so far are mentioned in section 2.1. Interestingly, it could be seen that there is no report of polarization of Crab in the infrared regime. Except for one far IR polarization measurement by Klaas et al 1999 [104] using ISOPHOT there are no detailed studies of IR polarization of the Crab pulsar and nebula. This provided motivation for the work reported in this chapter.

The Mount Abu InfraRed Observatory (MIRO), operated by Physical Research Laboratory since 1994, is located at the Gurushikhar peak ($\sim$1700 m) of Aravali ranges. Currently MIRO houses a 1.2 m telescope and a 50 cm telescope with a number of optical and infrared back end instruments to perform imaging photometry, spectroscopy and polarimetry. With an advantage of having a 1.2 m Cassegrain telescope at MIRO, we explored a possibility to develop an infrared polarimeter. Near Infrared Camera and Spectrograph (NICS) is one of the back end instruments for the 1.2 m telescope [70]. NICS is capable of doing both photometry and spectroscopy covering a wide range of 0.8 to 2.5 μm (Y, J, H, Ks) and has been serving as a work horse for the past several years to study diverse objects like AGN, galaxies, supernovae, novae and compact objects etc. We developed an imaging polarimeter NICSPol which consists of a rotating wire grid polarizer which is mounted between the telescope optics and NICS. The polarimetric observations are carried out by rotating the polarizer using a motorized mechanism to determine the Stokes parameters, which are then converted into the polarization fraction and polarization angle. A set of polarized and unpolarized standards were observed using NICSPol over J, H and Ks bands covering 0.8 to 2.5 μm. The observations of polarized standards using NICSPol show that, NICSPol can constrain polarization within $\sim$1% for sources brighter than $\sim$16 magnitude in JHKs bands. NICSPol is a general purpose instrument which could be used to study variety of astrophysical sources such as AGNs, Pulsars, XRBs, Supernovae, star forming regions etc. With a few NIR polarimeters available world-wide so far, NICSPol would be the first imaging NIR polarimeter in India.

We performed imaging polarimetry of Crab over J,H and Ks bands over multiple observation nights. We report the polarization map obtained over all three bands, while the interpretation of the results is a part of the future work. Here the NICSPol instrument design and its calibration results for IR polarimetric standards are discussed. Scientific prospects of NIR polarimetry are briefed in

Section 5.1 and NICSPol instrument specifications are given in Section 5.3. Sections 5.5 and 5.6 describe the observations and the data reduction. The results are discussed in Section 5.7, followed by the summary in Section 5.8.

5.1 Scientific Prospects of NIR Polarimetry

Polarization of light in infrared could be majorly due to scattering (e.g. polarization in comets, planets, asteroids etc are due to scattering by dust grains), and/or non thermal radiation (thermal radiation is unpolarized) (e.g. synchrotron radiation from AGN, XRBs). Extinction is when radiation from the source gets scattered and absorbed by the dust clouds they pass through. This decreases with increase in wavelength, and hence the sources which could not be studied in optical could be explored in infrared. Since scattering causes polarization, infrared polarization of such systems is the best possible way to study the dust and its properties. The following subsections briefs about various astrophysical systems and the problems which could be resolved using NIR polarimetry.

5.1.1 Pulsar Wind Nebulae

Pulsar Wind Nebulae are a type of supernova remnants also known as plerions. Plerions are powered majorly by the ultra relativistic particles from the pulsar and the radiation hence produced is the Pulsar Wind Nebula (PWN). Famous PWNe like Crab Nebula, 3C 58, W 44 and G21.5-0.9 etc could be studied in detail using NICSPol. The Crab pulsar and its nebula is one of the well studied sources among PWNe over all the ranges of the EM spectrum. Though Crab has been extensively studied over the past several decades there is no report on the NIR polarization of the Crab pulsar and the Nebula. In NIR both the thermal and synchrotron nebula and its features (wisps and knots) are bright. Hence the polarization at different parts and features of the synchrotron nebula could be studied. Along with the existing radio, optical and X-ray reports, NIR polarization of Crab Nebula can address energy dependence in polarization.

5.1.2 Stars and Star Forming Regions

Stars are formed from gas and dust, and throughout their evolutionary stages interact with their surroundings through circumstellar disks [105]. The proto starlight, hidden behind the dust gets extincted, hence the longer we go in wavelengths the deeper we are able to probe in the obscured area. With the help of IR wavelength and polarimetry as the technique the physical and chemical properties of the dust grains causing polarization could be studied. Nature of dust disk which are around young proto stars, their geometry, composition and physical properties could be revealed by the scattered polarized light.

5.1.3 Galactic Studies

Milky Way is broadly divided into a disk, bulge and halo. Star formation process dominates in the disk region leading to enrichment of the interstellar medium with sub-micron sized dust grains. The dust causes obscuration of the plane in the optical wavelength and is also responsible for the partial plane polarization of the star light. The galactic plane in IR reveals the stars hidden in and beyond the dust lanes. Using IR polarimetry the properties of the dust grains and the orientation of the magnetic field could be addressed and hence map the structure of dust in the line of sight [106]. This emphasizes on the need of IR polarimetry to study the dust and stellar polarization of the galactic plane region.

5.1.4 Extra Galactic Sources

Active Galactic Nuclei are galaxies with a super massive black hole surrounded by an accretion disk, dusty torus and jets. Even by using bigger telescopes spatially resolving this structure is impossible. Polarimetry in IR can reveal obscured AGN and also differentiate self luminous structures from those which are illuminated. NIR polarimetry can probe the dust near the torus. Apart from the disk and torus, the nature of jets, their emission mechanism and the role of magnetic field could be addressed using NIR polarimetry since that is the range of the electromagnetic spectrum where the synchrotron emission starts in the region where the jet is collimated and accelerated to relativistic speeds [107].

5.2 Instrumental Techniques

The Infrared regime of the EM spectrum helps in unveiling many embedded systems which could not be seen otherwise at optical wavelengths. The first measurement of IR polarization dates back to 1975 [108] and since then there have been several ground and space based instruments covering different regions from $\sim$0.8 μm in near IR to a few tens of μm in the far IR studying wide range of astronomical sources. Few well known near Infrared polarimeters are: SIRPOL at the 1.4 m IRSF [109], Mimir at the 1.8 m Perkins telescope [110], NICMOS at the 2.4 m HST [111], MMTPOL at the 6.5 m MMT Observatory [112], SOFI at the 3.58 m NTT telescope, La Silla Observatory [113], POLICAN at the 2.1 m telescope of the Guillermo Haro Astrophysical Observatory (OAGH) located in Cananea, Sonora, Mexico [114], TRISPEC as a visitor instrument at several facilities including UKIRT, UH, OAO, Subaru telescope [115], SPHERE at the

8.2 m VLT [116], HONIR at the 1.5-m Kanata telescope [117] etc. As mentioned earlier measurement of IR polarization require special optical components. The efficiency of the measurement method is one of the deciding factors in preferring a particular scheme. The following subsections briefly discuss a few of the popular techniques used in IR polarization measurement.

5.2.1 Wollaston prism with rotating half wave plate

In working with polarizers, one of the polarization state of the incident EM wave is either reflected or absorbed, so as to pass only one polarized state and hence reduces the efficiency by 50 percent. With the employment of Wollaston prisms, both the orthogonal polarization states i.e. the E-ray and O-ray are split and passed in different directions, building up on the total efficiency. The prism is fabricated by cementing calcite prism pairs, providing an extinction ratio of 100,000:1 [118]. As the polarization analysis requires the images to be taken at four position angles of the polarizer, while the use of wollaston will reduce this work by half, as two orthogonal angles could be captured together.

5.2.2 Wedged Double Wollaston (WeDoWo)

WeDoWo is a combination of two wollaston prisms and two wedges [119]. It helps in the simultaneous measurement of the polarization flux at four angles i.e. 0°, 45°, 90° and 135°. This provides more efficient observations as a single shot polarimetric measurement gives us all the three Stokes parameter elements.

5.2.3 Rotating Wire Grid Polarizer (WGP)

A WGP works on the principle of dichroism, and functions as an absorptive polarizer. The electromagnetic wave coming from the source is in mixed state of polarization, and only a selective direction is allowed to pass through the polarizer, while the rest is absorbed. A WGP consists of equally spaced grid of metallic wires placed in the plane of EM wave. As the EM wave is incident on the grid, the waves with polarization parallel to the wires are reflected back and the waves with polarization perpendicular to the wire grid is allowed to transmit. Thus, the selective direction in the case of WGP is perpendicular to the wire grids, with the resulting polarization to be linear. The choice of a WGP for a particular wavelength is dependant on the spacing and widths of the wires in the WGP [120]. The extinction ratio of polarizers is a measure of the ability to attenuate light in direction perpendicular to transmission axis of polarizer [121]. This is an important parameter which decides the efficiency of the polarizers. This ratio for WGP in infrared has a value of 1000:1. Compared to other polarization optical components, WGP can be made in larger sizes. Thus, the WGP work as effective polarizers with large field of view (FOV), are fairly compact, and have good stability [120]. Hence, they are used extensively in polarization measurements.

5.3 NICSPol Instrument description

NICSPol consists of a 25.0 x 25.0 mm WGP (WGP) commercially available from Thorlabs, which covers a wavelength range of 250 nm to 4 μm. The layout of the NICSPol instrument is shown in Figure 5.1. Figure 5.2 shows the instrument mounted on the Cassegrain plate of the MIRO telescope. The WGP mounting details are also shown in this figure. NICS is capable of doing both photometry and spectroscopy by the use of mirror and grating. The specifications of NICS are given in Table 5.1. NICS consists of a filter wheel with Y, J, H, K, Ks filters. The detector in NICS is Teledyne H1RG detector with 1024 x 1024 arrays which is cooled by using liquid Nitrogen and covers a FOV of 8 x 8 sq arc min [70]. At the top of NICS, the part which is attached to the instrument ring of the telescope is a 20 cm x 20 cm square box which contains a beam splitter. This essentially sends a fraction of the light from the source to a guiding ccd which helps in telescope tracking. The use of a warm WGP is necessitated by the requirement that the polarization module could be inserted in (or removed from) the light path without fully dismounting the entire instrument. The only drawback in this scheme (warm WGP) is the increased thermal background in the K band which restricts us to use only the Ks filter in the longer wavelength side.

Table 5.1: Specifications of NICSPol

Parameter	Specifications
Dimensions of WGP	WP25L-UB - 25.0 x 25.0 mm
Wavelength range	250 nm to 4 μm (useful range for NICS : 0.8 to 2.5 μm
Available NIR bands	Y (0.97 - 1.07 μm), J (1.17 - 1.33 μm), H (1.49 - 1.78 μm), K (2.03 - 2.37 μm), Ks(1.99 - 2.31 μm)
Detector	Teledyne H1RG detector with 1024 x 1024 arrays
Field of view	NICS - 8 x 8 sq arc min (imaging mode) NICSPol - 3.9 arc min dia (polarimetric imaging mode)
Pixel scale	0.5 arc sec per pixel
NICS optics and detector	Maintained at $\sim$ 77 K (Cooled by LN2)
WGP module	at ambient temperature
Limiting magnitudes	$\sim$ 16.8 in JHKs Typically with 30 - 40s per frame and a net exposure of 30 min

An Optec Pyxis LE Camera Field Rotator was found suitable to mount the

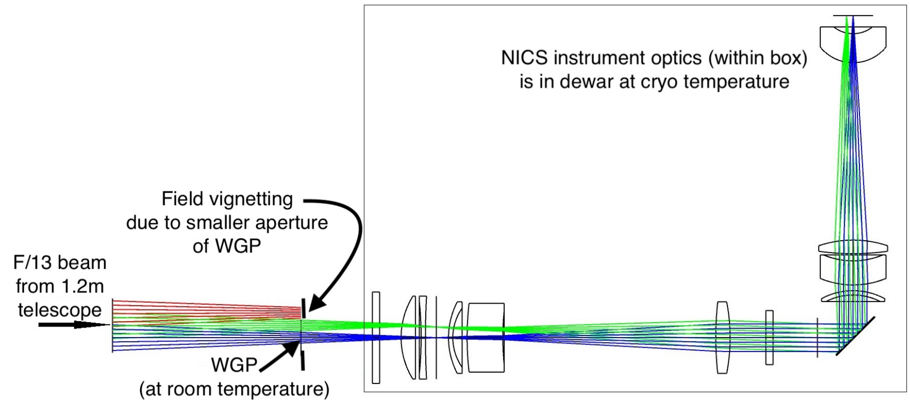

Figure 5.1: NICSPOL instrument with the WGP placed before the Cryostat window of NICS. From the ray diagram, its evident that the WGP position and size obscures part of the rays to reach the detector. The full FOV as covered by NICS, is thus reduced in NICSPOL (vignetting as seen by the extreme field rays not passing through the WGP to reach the detector). The different field projections on the detector plane are shown by rays of different colors.

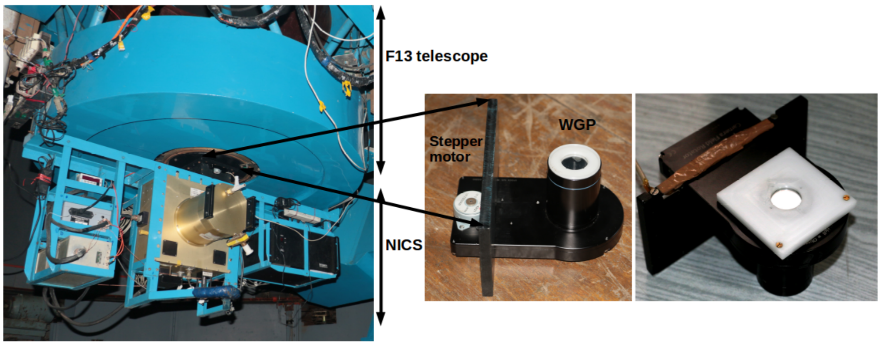

Figure 5.2: (a) NICS mounted on the f/13 telescope at MIRO along with the polarizer unit. (b) NICSPol unit with the 25 x 25 cm WGP (c) The second WGP mounted in NICSPol to polarize the incoming light to achieve 100% polarized radiation.

polarizer. The field rotator has a barrel which is rotated by a stepper motor with a step size of 1^{o} rotation. A delrin module was made to hold the polarizer firmly and the module was mounted in the barrel of the field rotator. A side of the beam splitter holder box was replaced by the module as in Figure 5.2 at a proper position so that the polarizer is exactly along the line through which the light from the secondary reaches the NICS optics. The polarimetry and imaging/spectroscopic modes are easily interchangeable. Since the size of the WGP

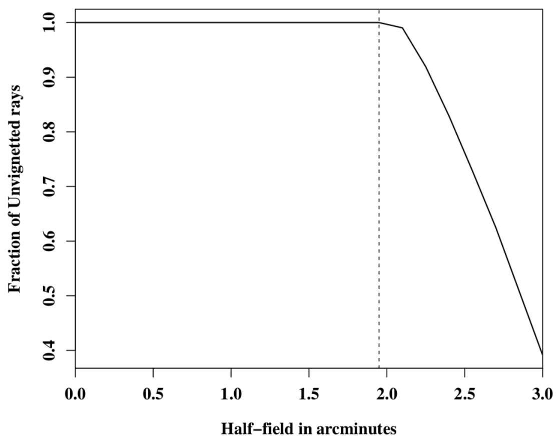

Figure 5.3: Field vignetting caused by the introduction of the WGP. It is seen that the vignetting starts beyond the dotted line (at 1.95 arcmin).

is such that it blocks some of the incoming beam, there is strong vignetting (see Figure 5.3) beyond half-field of 1.95 arcmin. This limits the useful FOV to 3.9 arc min (dia).

The faintest stars seen using NICS in J, H, Ks bands, using our 1.2 m telescope reach magnitudes of ∼17 with individual exposures of 30 to 40 sec per frame and a net exposure of 30 minutes. However, the introduction of the WGP will result in brighter detection limits, due to the ∼85% transmission of the WGP in NIR [121] making the NICSPol limiting magnitude ∼16.8. However in polarimetric mode we expect that these magnitudes might be achieved only under very stable skies.

5.4 Analysis Technique

The most preferentially used method in optical or IR to obtain PF and PA is the Stokes method. When a polarized beam passes through an analyzer which is rotating at discrete steps, the output beam gets modulated and follows a Cos2θ

distribution. A mathematical fit (equation 5.4) to the observed intensities provides the PF and PA. But getting intensities of a source at multiple steps over 0^o to 180^o is quite time consuming and in the case of the infrared domain the assumption that the sky has not changed over the observing period may not hold. The advantage of Stokes method is that, it requires intensities only at 3 (or 4) different orientations and effectively provides the PA and PF using any 3 (or all 4) of the I_0, I_{45}, I_{90}, I_{135} (intensities obtained by rotating the analyzer in steps of 45^o) measurements. Given by GG Stokes in 1852 [122] and introduced in astronomy by S Chandrasekhar in 1947, Stokes parameters I, Q, U, V describe the polarization state of a system in terms of intensities [123]. I (equation 5.1) represents the total intensity, Q (equation 5.2) and U (equation 5.3) represent linear polarization and V represents circular polarization. The Stokes parameters are calculated from the observations of flux measured at different orientations of the polarizer. The following equations give the relation between intensity and Stokes parameters [124].

$$I = \frac{1}{2}(I_0 + I_{45} + I_{90} + I_{135}) \tag{5.1}$$

$$Q = I_0 - I_{90} \tag{5.2}$$

$$U = I_{45} - I_{135} \tag{5.3}$$

Alternatively, Stokes parameters could be obtained by by fitting equation 5.4,

$$I_j = \frac{1}{2}[I_0 \pm Qcos2\theta_j \pm Usin2\theta_j] \tag{5.4}$$

The PF and PA are obtained from the Stokes parameters using equations 5.5 and 5.6.

$$PF = \sqrt{\frac{Q^2 + U^2}{I}} \tag{5.5}$$

$$PA = \frac{1}{2} tan^{-1} \frac{U}{Q} \tag{5.6}$$

5.5 Observations

This section describes the list of observations made to verify the instrument performance using lab and sky polarimetric standards. The instrument had to be checked with polarized and unpolarized standards for efficiency and instrumental polarization respectively. NICSPol was calibrated using both polarized and unpolarized stellar standards. A second WGP of same dimensions was also used to achieve 100 % polarized light. This WGP was mounted stationary in NICSPol in a way that light from the source would first pass through it, get polarized and pass through the rotating WGP resulting in a 100 % polarized light. For calibration with stellar sources both isolated stars and crowded fields were observed.

Table 5.2 shows the complete log of all the observations made for the calibration of NICSPol. A major issue faced was the small number of stellar polarimetric standards in NIR. The few available standards are polarized to a maximum of 3 - 4% in J band. 6 UKIRT polarimetric standards : HD 283809, HD 204827, HD 29333, HD 283725, HD 283855 and HD 283701 and four unpolarized standards : HD 202573, HD 212311, HD 103095 and HD 65583 (to check for instrumental polarization) [125],[126] were selected based on their availability at MIRO winter sky. The polarized standards were chosen such that they possess a degree of polarization of about 2 - 4 % and these were followed up over multiple nights from September to November 2017 and December 2018 to January 2019. A critical part of NIR observations is the removal of sky contribution, which is bright in infrared. For a particular source, for each filter the polarimetric images were taken

Table 5.2: Log of all Observations using NICSPol

Source	Observed Nights	Filter	Posi- -tions	Frames	Orient- -ations	Exposure /frame
HD 283809[a]	10 7 8	J H Ks	5 5 5	2 to 10 2 to 5 2	4 4 4	1 s 1 s 1 s
HD 204827[a]	5 4	J H	5 5	3 3	4 4	801 ms 801 ms
HD 29333[a]	5 2 1	J H Ks	4 4 4	2 2 2	4 4 4	1 s 1 s 1 s
HD 283725[a]	2	J	5	3	4	1 s
HD 283855[a]	2	J	5	3	4	1 s
HD 283701[a]	1	J	5	3	4	1 s
HD 56591[b]	1	J	3	3	11	2 s
HD 26212[b]	1 1 1 1 1	J H Ks K Y	3 3 3 3 3	3 3 3 3 3	4 4 4 4 4	2 s 2 s 2 s 2 s 2 s
NGC 2548[b]	1	J	5	5	4	20 s
M3[b]	1	J	3	5	4	30 s
HD 202573[c]	2 2 2 2	J H Ks K	5 5 5 5	2 2 2 3	4 4 4 4	1 s 1 s 1 s 1 s
HD 212311[c]	7 5 3	J H Ks	5 5 5	2 2 2	4 4 4	3 s 3 s 3 s
HD 103095[c]	3	J	4 to 8	5	4	801 ms
HD 65583[c]	1	J	7	5	4	801 ms
RA 07 - 08 h[d]	1	J	5	3	4	10 s

a - Polarized standards, b - Sources with WGP to check for 100 % polarization, c - Unpolarized standards, d - Photometric standard star field.

by dithering the source in minimum 5 positions and the sky frame was made from these multiple dithered frames of the source itself. In case of extended sources sky frames were taken separately by taking the source out of the field of detector for the same exposure as the source, assuming the sky to be constant over this dithering period. The source images were taken for 3 filters x 5 dithering positions (with 3 frames per position) x 4 orientations of the WGP. The exposure time varied from 801 ms in case of bright point sources (minimum achievable by NICS) to 20 s each for faint sources. Also to check how closely the results from 4 orientations would match with the result from data with multiple points fitted using equation 5.4, HD 56591 was observed with 2 WGPs (i.e. polarizing the light from the source), for 0 ^{o} to 150 ^{o} with 15 ^{o} angular step size.

5.6 Data Reduction and Analysis

As explained in Section 5.5 the Stokes method is followed to analyze the polarimetric data. The analysis was carried out using standard *IRAF* (Image Reduction and Analysis Facility) procedures along with a few *IDL* scripts to ease the analysis. The initial steps to analyze the polarized images in IR are the same as standard IR photometry. For a given source and a given band, the images had been taken by rotating the polarizer in four orientations, 0^o, 45^o, 90^o, 135^o and multiple frames are taken for each dithering position. And as mentioned earlier the IR sky is bright hence sky subtraction is a critical step in the analysis. Sky frames were constructed by median combining source frames taken at different dithering positions. This sky image obtained was subtracted from all the raw source images to get the sky subtracted frames. To improve the S/N ratio multiple frames of all the positions should be added up. Since the position of the source would be different in each frame, it was shifted to a common point with respect to a particular star and the shifted images were combined to give a final image for each orientation. The next step is to get the intensities of the source at the 4 orientations. Similar to photometry the magnitude of the source should be extracted and then converted into intensity. For this the *IRAF phot* procedure was used to do aperture photometry, where a range of apertures were defined for the source and using the curve of growth plot a suitable aperture size was considered for further analysis. The above procedures were repeated for all 4 orientations of observations hence giving 4 intensities I_0, I_{45}, I_{90}, I_{135}. The Stokes parameters were calculated from these intensities and the degree of polarization and the polarization angle are obtained from the Stokes parameters 5.4). The additional advantage of following Stokes method is that since normalization is done with Intensity (I) any systematic error in the parameters are cancelled out. In the case of extended sources a standard *IRAF* procedure, linpol, would directly give pixel by pixel information of PF, PA, I, Q, U.

5.7 Results

5.7.1 100 % Polarized Light

By mounting a second stationary WGP the incoming light from a source is polarized, using this the polarimetric efficiency of NICSPol was tested by observing HD 56591, HD 26212, NGC 2548 and M3. The obtained PF and PA are tabulated in Tables 5.3 and 5.4. The modulation curves for HD 56591 and HD 26212 are plotted in Figure 5.4. The reason behind the PF crossing 100% within the error bar is that, the intensity of the source at 135° and above is very less which increases the uncertainty in the photometric measurement. The fitted PA of both the sources are found to be consistent over all the bands and the error in PA is found to be only $\sim$ 0.1 - 0.2°. Figure 5.5 shows the NGC 2548 field marked with polarization vectors of all the sources whose details are tabulated in Table 5.4. It could be seen that the results are consistent over the entire FOV of the NICSPol module over the detector.

Table 5.3: Observed PF, PA for 100 % polarized standard stars.

Source	Band	Observed PF (%)	Obs PA (°)
HD 56591	J	100.75±0.52	-38.36±0.09
HD 26212	J	100.15±0.94	-38.45±0.24
	H	100.16±0.66	-38.37±0.18
	Ks	100.5±0.95	-38.21±0.24
	K	100.74±0.96	-38.20±0.20
	Y	100.58±1.22	-38.23±0.3

Table 5.4: Observed PF and PA for 100 % polarized light for the source NGC 2548.

Source	Obs PF (%)	Obs PA (°)
Star 1	100.45±0.62	15.24±0.16
Star 2	99.96±0.8	15.29±0.18
Star 3	100.66±1.67	15.43±0.39
Star 4	100.22±0.87	15.4±0.22
Star 5	99.66±0.36	15.49±0.10
Star 6	100.53±1.4	15.97±0.33
Star 7	100.44±0.8	15.53±0.21
Star 8	101.16±2.76	15.62±0.63
Star 9	99.57±0.27	15.44±0.07
Star 10	96.87±0.61	15.41±0.18
Star 11	96.12±1.37	14.21±0.35
Star 12	101.57±2.48	15.24±0.57
Star 13	100.9±1.15	15.49±0.29
Star 14	100.82±1.41	15.59±0.34
Star 15	99.04±3.63	14.88±0.83
Star 16	96.02±2.95	20.69±0.76
Star 17	98.00±2.85	18.57±0.73
Star 18	100.92±2.48	15.04±0.57

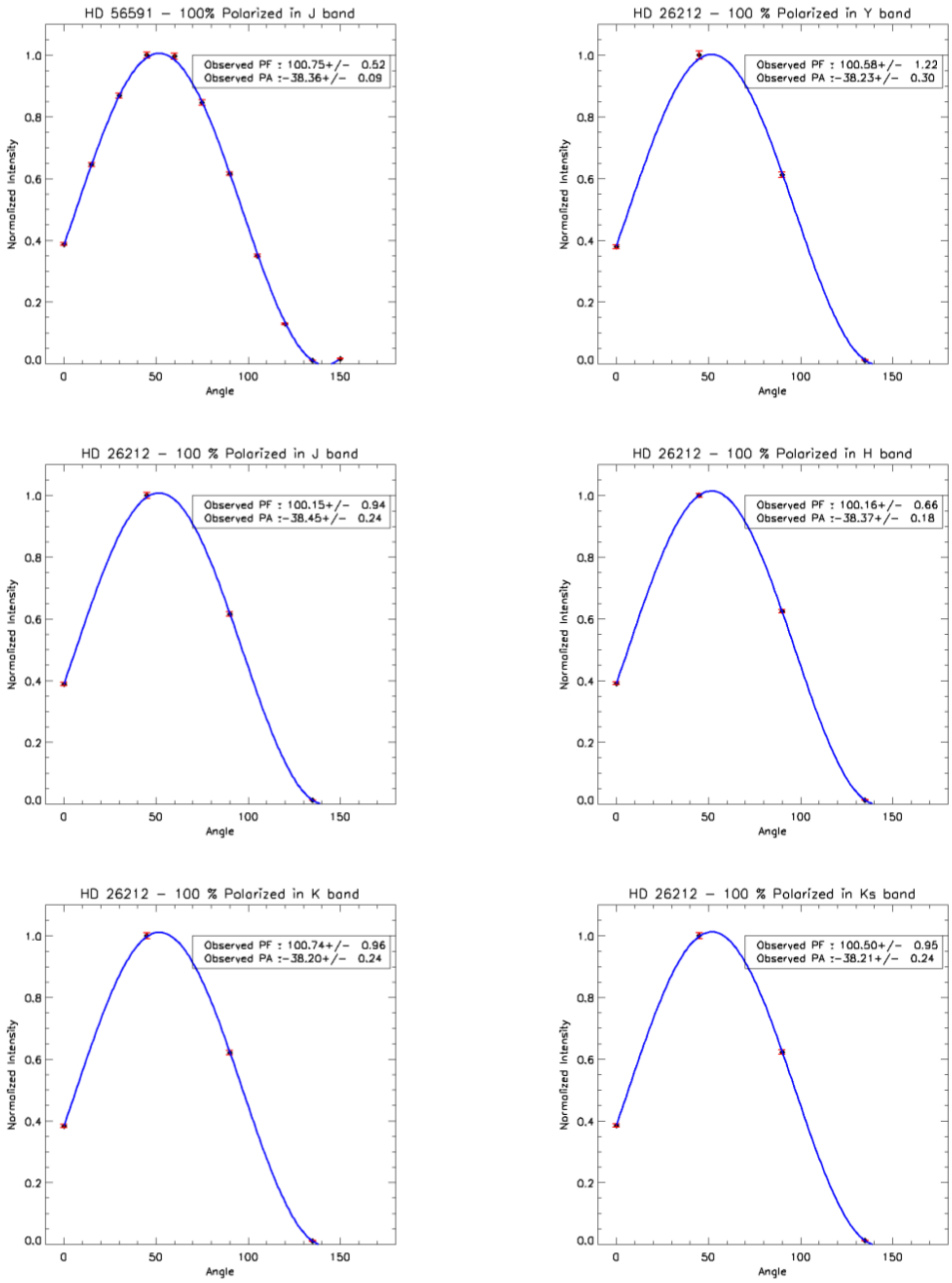

Figure 5.4: Modulation curves for 100 % polarized light for sources (a) HD 56591 in J band and (b)-(f) HD 26212 in Y, J, H, K, Ks bands with fitted PF and PA quoted inside.

5.7.2 Unpolarized Stars

Four unpolarized standards - HD 202573, HD 212311, HD 103095 and HD 65583 were observed using NICSPol and the obtained PF are tabulated in Table 5.5.

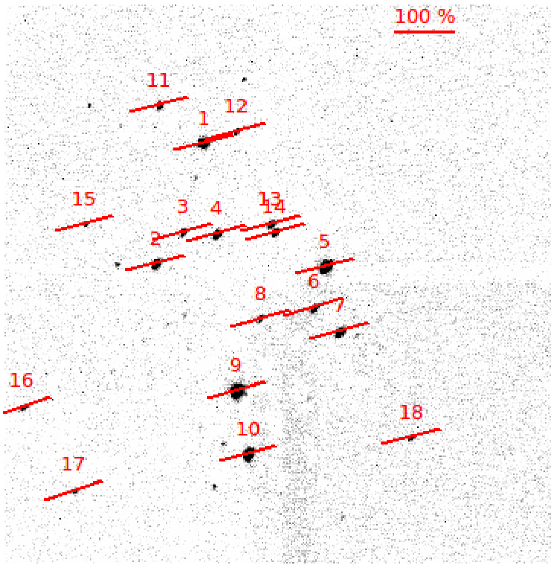

Figure 5.5: 100% polarized light using second WGP from NGC 2548, marked with polarization vectors using the PF and PA obtained.

HD 103095 and HD 65583 was also observed by dithering the source at multiple positions (8 positions). Figure 5.6 shows the PF and PA obtained over various positions in the FOV for both HD 103095 and HD 65583. The PFs at all the positions were lesser than 1%. and also the PAs over these positions were found to be random. Figure 5.7 shows the modulation of unpolarized standard HD 103095. Figure 5.8 shows the PF of one unpolarized standard HD 212311 observed over several nights which is found to be around 1%. From unpolarized standards it is seen that the uncertainty is around ∼1%.

5.7.3 Polarized Standard Stars

IR polarized standards are less in number and the degree of polarization is generally quite low compared to optical wavelengths. Six polarized standards - HD 283809, HD 204827, HD 29333, HD 283725, HD 283855 and HD 283701, were observed and a few of these were followed up during several observing nights. The obtained PF and PA along with standard reported values are tabulated in

Table 5.5: Observed PF for Unpolarized standard stars.

Source	Band	Observed PF (%)	Ref
HD 202573	J K	1.2±0.24 0.21±0.23	[126]
HD 212311	J H Ks	0.65±0.68 0.52±0.49 1.37±0.81	[127]
HD 103095	J	0.39±0.23	[126]
HD 65583	J	0.07±0.52	[126]

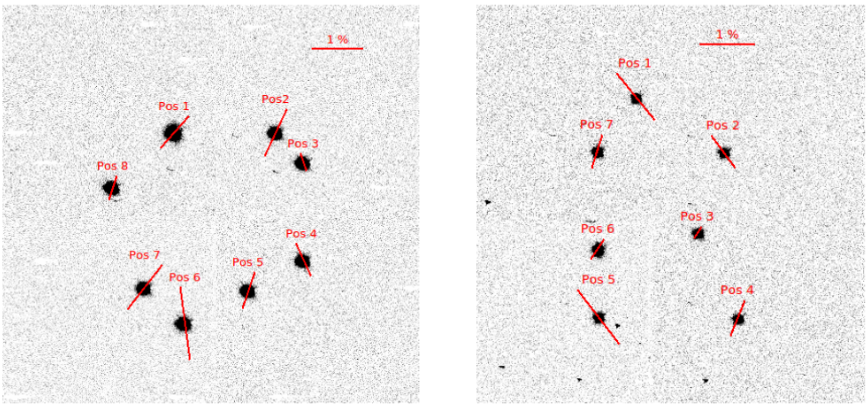

Figure 5.6: Unpolarized standards (a) HD 103095 and (b) HD 65583 over different positions in the FOV marked with polarization vectors using the PF and PA obtained.

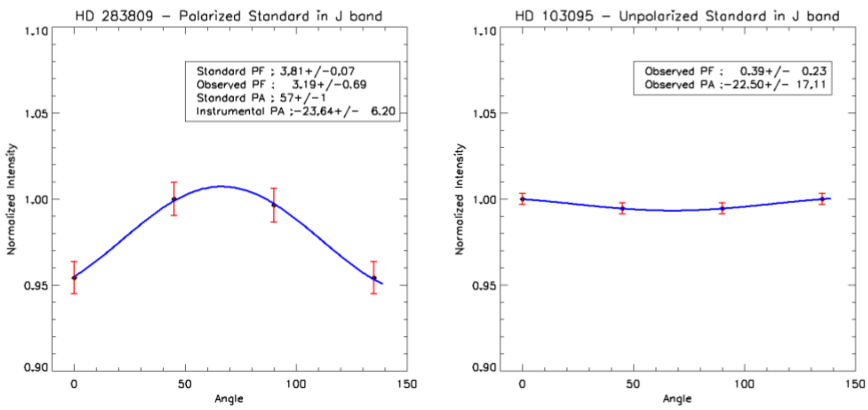

Figure 5.7: Modulation curves fitted over 4 phase angles for (a) polarized standard HD 283809 and (b) unpolarized standard HD 103095.

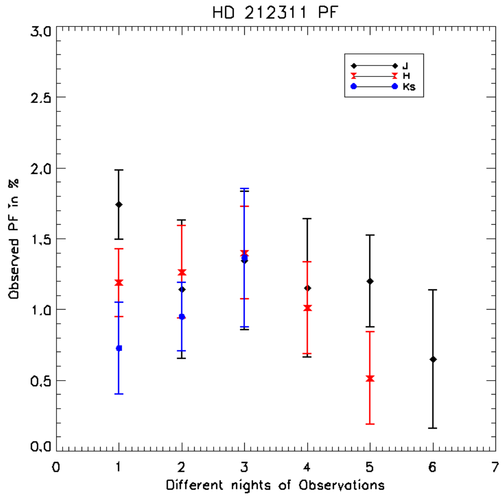

Figure 5.8: Observed PF for an unpolarized source HD 212311 over J, H, Ks bands at different nights.

Table 5.6. The references of reported PF, PA of chosen standards are given in Ref column. The instrumental polarization angle obtained by fitting Equation 5.4 has to be converted into the standard polarization angle with reference to the local North in the equatorial coordinate system. Over a given observation night the difference between the instrumental PA and Standard PA is expected to be same for different sources and by implementing this correction factor Observed PA is obtained. Figure 5.9 shows the difference between the instrument and standard PA for all the sources over all observation nights. It could be seen that the observed values match with the standard values well within the error bar for sources HD 283809, HD 204827, HD 29333 and HD 283725. Figure 5.10 shows the PF and PA values obtained for HD 283809 with the standard values quoted inside for J, H and Ks bands and modulation curve of one observation is given in Figure 5.7. The observed PF and PA for HD 283809 and HD 29333 were found to be consistent when focused over different positions of the detector FOV. For sources HD 283855 and HD 283701 although the Observed PF match the

Standard PF, the Observed PAs are different from the reported values. It should be noted that at least for HD 283701, different PA values of $42^o \pm 5^o$ (Whittet et al. 1992 [125]) to $33^o \pm 1.3^o$ (Whittet et al. 2001 [128]) are reported in literature. This indicates the possibility that the PA change could be real, which can only be confirmed by further observations that we plan to continue. Figure 5.11 shows the obtained PF and PA plotted with respect to the reported values of PF PA. MIMIR instrument reported the PF and PA of standard stars with small error bars [110]. The reason for our relatively large errors in comparison with MIMIR is, in MIMIR's case the observations are taken for 32 half wave plate position angles, i.e. for every 11.25^o. Also MIMIR is at 1.8 m Perkins telescope hence has large number of photons available therefore less photon noise. These result in higher precision in the measurements. For e.g. in one of our 100% polarization observations (5.7.1), one set of observations were made for every 15^o position angle covering 0^o - 165^o (Figure 5.4). From these 11 position angles of the WGP PF = 100.75%±0.52%, PA = $-38.36^o \pm 0.09^o$ are obtained. Whereas when only 4 position angles from these with a step size of 45^o was used the values obtained are PF = 100.8%±0.9%, PA = $-38.49^o \pm 0.2^o$. The increase in errors due to the smaller number of position angles is evident in the case of 100% polarized light and this would affect the sources with low polarization. Hence in the case of NICSPol it is preferable to go for more position angles while observing sources with low PF, while 4 positions angles would be sufficient to study highly polarized sources.

Table 5.6: Standard PF, PA and Observed PF, PA for Polarized standard stars.

Source	Band	Std PF (%)	Obs PF (%)	Std PA (°)	Obs PA (°)	Ref
HD 283809	J H Ks	3.81±0.07 2.59±0.07 1.71±0.11	3.19±0.69 2.12±0.33 1.53±0.49	57±1 58±1 55±1	49.52±6.2 56.29±4.4 59.04±9.18	[125] [125] [125]
HD 204827	J H	2.83±0.07	2.12±0.49 1.71 ±0.33	61.1±0.8	63.85±6.55 60.45±5.47	[129]
HD 29333	J H Ks	2.88±0.03 1.81±0.04 1.19±0.08	2.47±0.49 1.81±0.49 1.14±0.49	69±1 68±1 73±1	69.2±5.67 70.57±7.73 66.46±12.3	[125] [125] [125]
HD 283725	J	2.5±0.3	2.49±0.33	66±1	62.44±5.61	[125]
HD 283855	J	2.58±0.03	2.27±0.33	46±1	172.16±14.4	[125]
HD 283701	J	1.68±0.12	1.65±0.33	33±1.3	7.16±11.31	[128]

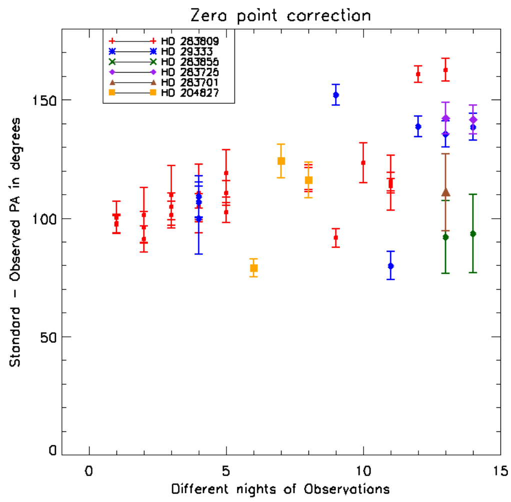

Figure 5.9: Difference between Standard PA and instrumental PA over different observation nights.

5.7.4 Polarization Measurement of a Photometric Standard Field

Landolt, A. U. in 1992 [130] listed photometric standards around the celestial equator whose V band magnitudes range between ∼ 11 - 16. RU 149 a blue star,

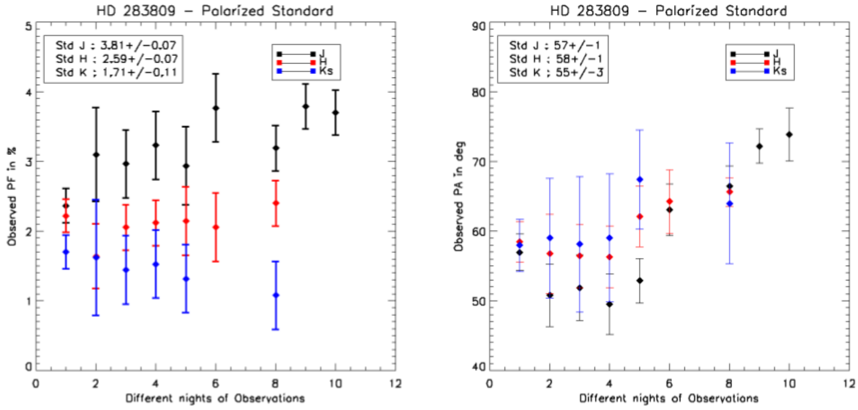

Figure 5.10: Observed (a) PF and (b) PA for a polarized source HD 283809 over J, H, Ks bands at different nights with standard values quoted inside.

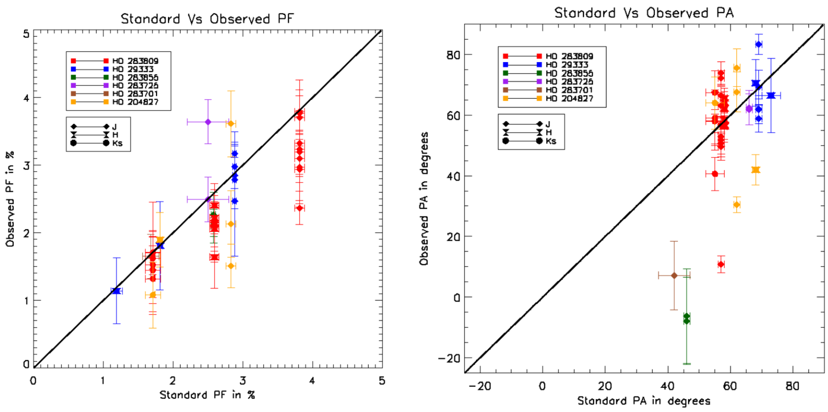

Figure 5.11: (a) Observed PF Vs Standard PF and (b) Observed PA Vs Standard PA values for all polarized standards (color coded) at different nights. Different symbols are used for J, H and Ks bands as labelled inside.

and other surrounding stars (RU 149 A - G) in the field which are in RA 07 - 08 h was observed using NICSPol. Figure 5.12 shows the field observed and by comparing with the standard 2mass image, the magnitudes of the stars in J band were obtained which are marked in the figure. To estimate the limiting magnitude which could be achieved using NICSPol, polarization analysis of all the stars in the field was carried out. The exposure time per frame was 10 s (5 positions, 3 frames each, 4 angles) which resulted in a net exposure of 10 min for the complete observation. It could be seen that with this net exposure it is possible to measure polarization for stars as faint as ∼15 mag in J. Hence with a higher exposure it is possible to reach up to ∼16.5 (fainter stars seen in the field) using NICSPol. This matches very well with the number quoted earlier in Section 5.3 (∼16.8). Since the observed field is closer to the Galactic plane the stars in the field can not be concluded as unpolarized.

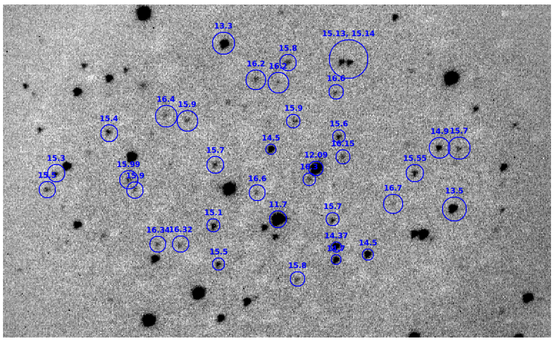

Figure 5.12: Stars in the photometric standard field RU 149 marked with their respective magnitudes in J band.

5.7.5 Preliminary results of NIR polarization of Crab

NICSPol is used to perform imaging polarimetry of the Crab pulsar and nebula. In case of extended sources like Crab, it is not possible to obtain the sky frames from dithered source observations. In order to perform sky subtraction, independent observations of a region closer to the source for the same exposure as the source is necessary. Crab nebula and the sky background region are observed over J band for 6 dithered positions with an exposure time of 20 s per frame (5 frames per position). The source and background observations are performed for four position angles of WGP (0°, 45°, and 90°, and 135°). Figure 5.13 shows the false color composite (FCC) of Crab observed at 0°, 45°, and 90° WGP positions along with the image (photometry) of Crab observed in J, H, and K bands. The image clearly represents that the nebula is strongly polarized in the infrared regime.

A detailed interpretation of the results of Crab NIR polarimetry obtained using NICSPol is a part of the future work.

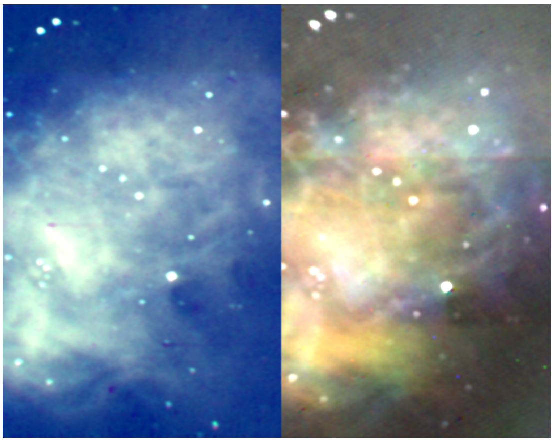

Figure 5.13: From the left: The FCC image (H - red, J - green, K - blue) of Crab using NICS and the FCC image obtained using NICSPol in J band (0° - red, 45° - green, 90° - blue)

5.8 Summary

This chapter described the design and test results of NICSPol, an NIR polarimeter add-on for NICS instrument covering wavelength range of 0.8 - 2.5 μm for the 1.2 m telescope at MIRO. NICSPol is the first imaging polarimeter in India and covers a FOV of 3.9 arc min dia and has a pixel scale of 0.5 arc sec per pixel. The polarization analysis is performed using IRAF and IDL following the standard Stokes methodology to obtain the degree of polarization and the polarization angle. Observations of NIR polarimetric standards as well as unpolarized stars using NICSPol show that the polarization degree and angle can be accurately determined within 1% and a few degrees, respectively. This shows that NICSPol is suitable to carry out NIR polarization of sources with magnitudes brighter than $\sim$16 over J, H, Ks bands and polarization greater than $\sim$1%. As discussed in section 5.7.4, for highly polarized sources, observations with large step angles would be sufficient, however for sources with low polarization, more steps should be used to fill the modulation curve and achieve higher accuracy. NICSPol is a general purpose instrument at MIRO and can be used for observations of both point and extended sources. NICSPol could be simultaneously with the optical polarimeter available at the 50 cm telescope at Mt Abu to study wide variety of galactic and extra galactic sources and hence many more scientific results are expected in near future.

Chapter 6

Conclusions

The thesis summarizes the results of polarimetry in hard X-ray and near infrared regimes. The first part of the dissertation describes the hard X-ray polarization of Crab using AstroSat CZTI which drives the motivation for the thesis in two branches: 1) Exploring hard X-ray polarimetry of other transient sources (Gamma-ray bursts) using CZTI, 2) Exploring Crab polarization in infrared regime with the advantage of accessibility to the Mt Abu Infrared Observatory,

6.1 Summary of Results

Chapter 1 briefly introduces the astrophysical targets for which polarization studies are performed in the thesis. It also discusses the basics of X-ray polarimetry and its types followed by a brief description of CZTI as a hard X-ray polarimeter. Chapter 2 describes the results of phase averaged and phase resolved polarization of the Crab pulsar and nebula using CZTI data observed for a net exposure of $\sim$1800 ks. Polarization analysis is performed over different energy ranges by following dynamic binning within 100 – 380 keV. The change in polarization corresponding to the two pulses, bridge, and off-pulse regions with respect to energy of incoming photon are reported for the first time. The results discussed in this chapter clearly imply the need to probe further in theoretical development in order to explain the change in polarization signatures both with respect to phase and energy of incoming photons.

CZTI, on its first day of operation (October 06, 2015) detected a Gamma-ray burst GRB151006A and over a year 47 GRBs were detected by CZTI. This advantage of CZTI being a GRB detector along with its polarization capability provides an opportunity to measure polarization of GRBs above 100 keV. Chapter 3 describes the polarization analysis of 11 bright GRBs detected by CZTI between October 2015 – October 2016. From the results it could be observed that most of the GRBs are highly polarized indicating the emission mechanism behind prompt emission to be either synchrotron in an ordered magnetic field or Compton drag. However, in order to constrain the degeneracy in the geometry and emission mechanism polarization measurements of a large number of GRBs are required. CZTI is expected to provide polarization measurements of $\sim$10 GRBs per year and could substantially help in improving the current understanding of prompt emission.

CZTI emerged to be a prolific GRB polarimeter post launch of AstroSat. In order to enhance the credibility of polarization results of CZTI for off-axis sources like GRBs, a set of controlled experiments and simulations are performed which are discussed in detail in chapter 4. For various off-axis configurations the polarization results obtained from experiments are found to be matching quite well with the Geant4 simulations. Through a set of independent Geant4 simulations, the MDP for incident polar angles $0° - 90°$ each for polarization angles $0° - 90°$ corresponding to two cases of number of Compton events (3000 and 10000) are evaluated. As a result of this study it could be interpreted that

CZT detectors are suitable to measure polarization of GRBs for which the incident direction $\theta < 60^{\circ}$ from the normal.

The successful measurement of Crab polarization in hard X-rays provides motivation to study the polarization of Crab in other wavelengths. Interestingly, polarization of Crab in the infrared regime is not reported so far. Since there are no IR polarimeters in India we developed NICSPol, a near IR imaging polarimeter as an add-on to an existing back end instrument NICS at the MIRO. Chapter 5 discusses NICSPol instrument and the calibration results of NICSPol by observing a set of polarized and unpolarized standards over multiple observation nights. NICSPol covers a wavelength range of 0.8 - 2.5 μm and is suitable to measure polarization of sources with magnitudes brighter than $\sim$16. We used NICSPol to perform NIR polarization of Crab and the results imply strong polarization signatures of nebula that needs further investigation.

6.2 Future Outlook

The work presented in this thesis embarks scope for a few interesting scientific studies which can be followed up in future.

6.3 Phase resolved polarization of Crab in optical, NIR, hard X-rays

We carried out phase resolved polarization of Crab over 100 – 380 keV using CZTI and phase averaged polarization of Crab pulsar and nebula together over 0.8 - 2.5 μm using NICSPol. The current read out time of NICS is not feasible to perform phase resolved polarimetry. However, NICS could be customized to observe a smaller FOV with a fast read out time. In addition to this, a Near-Infrared Imager, Spectrometer & Polarimeter (NISP), one of the back end instruments for the upcoming 2.5 m telescope at MIRO, is currently under development. The advent of these facilities in IR along with CZTI could provide a unique opportunity to have a multiwavelength measurement of phase resolved Crab polarization. Also, the polarization of the nebula in infrared regime is expected to provide many interesting insights. For example, in the current results of Crab polarization using NICSPol it could be seen that few bright filaments in thermal part of nebula posses low polarization while the regions that have low intensity have high polarization fraction. With the current measurements of phase resolved polarization in optical and hard X-rays, measurement of phase resolved polarization in infrared could lead to further developments in theoretical models based on multiwavelength polarization.

6.4 Polarization of five years GRB sample using CZTI

We have already reported the polarization of 11 GRBs from its first year sample. CZTI has detected 306 GRBs between October 2015 – June 2020. From this large five year sample of GRBs, polarization of ∼60 GRBs is expected to be measured. A statistical study of such large number of GRBs with polarization measurement could help in constraining existing conflicts in the prompt emission mechanism. Further, we have achieved few improvements in the polarization analysis technique: better noise clean algorithm, gain correction to spectroscopically bad pixels, using Compton events detected in next neighbor pixels. These could enhance the number of Compton events detected and there by improving the signal to noise. Since each GRB is unique, probing individual bright GRBs to perform time resolved and energy independent polarization analysis could provide more understanding about the radiation process and nature of magnetic field in the jet.

Publications

Publications included in thesis

- "NICSPol, A Near Infrared polarimeter for the 1.2 m telescope at Mount Abu Infrared Observatory", **E. Aarthy**, A. Rai, S. Ganesh, S. Vadawale, Published in Journal-ref: J. Astron. Telesc. Instrum. Syst. 5(3), 035006 (2019) DOI: 10.1117/1.JATIS.5.3.035006.

- "Prompt emission polarimetry of Gamma Ray Bursts with AstroSat CZT-Imager", T. Chattopadhyay, S. V. Vadawale, **E. Aarthy**, N. P. S. Mithun, V. Chand, R. Basak, A. R. Rao, S. Mate, V. Sharma, V. Bhalerao and D. Bhattacharya, Astrophysical Journal, vol. 884, p. 123, Oct 2019.

- "Experimental verification of off-axis polarimetry with Cadmium Zinc Telluride detectors of AstroSat-CZT Imager", **E. Aarthy**, S. V. Vadawale, N. P. S. Mithun, N. R. Navale, T. Chattopadhyay, A. R. Rao, V. Bhalerao, D. Bhattacharya, Under review JATIS , 2020.

- "Energy dependent phase resolved Crab polarimetry using AstroSat CZT-Imager", **E. Aarthy**, S. V. Vadawale, N. P. S. Mithun, A. Ratheesh, T. Chattopadhyay, A. R. Rao, V. Bhalerao, D. Bhattacharya, Under preparation, To be submitted in MNRAS, 2020.

Publications not included in thesis

- "A tale of two transients: GW170104 and GRB170105A", V. Bhalerao, M. M. Kasliwal, D. Bhattacharya, A. Corsi, **E. Aarthy**, S. M. Adams et al The Astrophysical Journal, Volume 845, Issue 2, article id. 152, 10 pp. (2017).

- "Violation of Synchrotron Line of Death by the Highly Polarized GRB 160802A",

V. Chand, T. Chattopadhyay, S. Iyyani, R. Basak, **E. Aarthy**, A. R. Rao, S. V. Vadawale, D. Bhattacharya,V. Bhalerao, The Astrophysical Journal, Volume 862, Issue 2, article id. 154, 11 pp. (2018).

- "Time varying polarized gamma-rays from GRB 160821A: evidence for ordered magnetic fields", V. Sharma, S. Iyyani, D. Bhattacharya, T. Chattopadhyay, A. R. Rao, **E. Aarthy**, S. V. Vadawale, N. P. S. Mithun, V. B. Bhalerao, F. Ryde and A. Pe'er, Accepted in APJ Letters.

Workshops, Schools, Conferences and Seminars

- Attended the conference on “Wide band spectral and timing studies of Cosmic X-ray sources” held at TIFR, Mumbai during Jan 2017.

- Delivered a talk entitled “GRB Polarization using AstroSat CZTI” in ASI - 2017 held at Jaipur during March 2017.

- Delivered a talk entitled “Measuring GRB Polarization using AstroSat CZTI” in the Workshop on Gamma Ray Bursts: Prompt to Afterglow held at NCRA, Pune during July 2017.

- Presented a poster entitled “Near Infrared Polarimetry – an add on to NICS at MIRO” in ASI - 2018 held at Hyderabad during February 2018.

- Delivered a talk entitled “Experimental verification of off axis polarization of AstroSat CZTI” at the conference Hard X-ray polarization from black hole sources held at Pachgani during 29 - 30 March 2018.

- Attended the summer school “Looking at Cosmic sources in polarized light” held at the Asiago Observatory, Italy during 18 - 26 June 2018.

- As a member of the Organizing Committee actively took part in organizing and conducting the Young Astronomer’s Meet during September 24 - 28, 2018 at Physical Research Laboratory, Ahmedabad.

addcontentslinetocchapterBibliography

Bibliography

[1] D. K. Aitken, “Infrared polarimetry,” *Vistas in Astronomy*, vol. 31, pp. 755–762, 1988.

[2] Y. N. Gnedin, G. G. Pavlov, and Y. A. Shibanov, “The effect of vacuum birefringence in a magnetic field on the polarization and beaming of X-ray pulsars,” *Soviet Astronomy Letters*, vol. 4, pp. 117–119, 1978.

[3] P. Meszaros, W. Nagel, and J. Ventura, “Exact and approximate solutions for the one-dimensional transfer of polarized radiation, and applications to X-ray pulsars,” *Astrophysical Journal*, vol. 238, pp. 1066–1080, June 1980.

[4] J. J. Hester, “The Crab Nebula : an astrophysical chimera.,” *Annual Rev. Astron. Astrophys*, vol. 46, pp. 127–155, Sept. 2008.

[5] R. Bühler and R. Blandford, “The surprising Crab pulsar and its nebula: a review,” *Reports on Progress in Physics*, vol. 77, p. 066901, June 2014.

[6] M. C. Weisskopf, E. H. Silver, H. L. Kestenbaum, K. S. Long, and R. Novick, “A precision measurement of the X-ray polarization of the Crab Nebula without pulsar contamination,” *Astrophysical Journal Letter*, vol. 220, pp. L117–L121, Mar. 1978.

[7] M. A. Ruderman and P. G. Sutherland, “Theory of pulsars: polar gaps, sparks, and coherent microwave radiation.,” *Astrophysical Journal*, vol. 196, pp. 51–72, Feb. 1975.

[8] J. Arons and E. T. Scharlemann, "Pair formation above pulsar polar caps: structure of the low altitude acceleration zone.," *Astrophysical Journal*, vol. 231, pp. 854–879, Aug. 1979.

[9] R. W. Romani and I.-A. Yadigaroglu, "Gamma-ray pulsars: Emission zones and viewing geometries," *Astrophysical Journal*, vol. 438, pp. 314–321, Jan. 1995.

[10] A. K. Harding, J. V. Stern, J. Dyks, and M. Frackowiak, "High-Altitude Emission from Pulsar Slot Gaps: The Crab Pulsar," *Astrophysical Journal*, vol. 680, pp. 1378–1393, June 2008.

[11] J. Dyks and B. Rudak, "Two-Pole Caustic Model for High-Energy Light Curves of Pulsars," *Astrophysical Journal*, vol. 598, pp. 1201–1206, Dec. 2003.

[12] J. Dyks, A. K. Harding, and B. Rudak, "Relativistic Effects and Polarization in Three High-Energy Pulsar Models," *Astrophysical Journal*, vol. 606, pp. 1125–1142, May 2004.

[13] J. Pétri and J. G. Kirk, "The Polarization of High-Energy Pulsar Radiation in the Striped Wind Model," *Astrophysical Journal Letter*, vol. 627, pp. L37–L40, July 2005.

[14] A. K. Harding and C. Kalapotharakos, "Multiwavelength Polarization of Rotation-powered Pulsars," *Astrophysical Journal*, vol. 840, p. 73, May 2017.

[15] F. G. Smith, D. H. P. Jones, J. S. B. Dick, and C. D. Pike, "The optical polarization of the Crab Pulsar," *MNRAS*, vol. 233, pp. 305–319, July 1988.

[16] P. Ubertini, F. Lebrun, G. Di Cocco, A. Bazzano, A. J. Bird, K. Broenstad, A. Goldwurm, G. La Rosa, C. Labanti, P. Laurent, I. F. Mirabel, E. M. Quadrini, B. Ramsey, V. Reglero, L. Sabau, B. Sacco, R. Staubert, L. Vigroux, M. C. Weisskopf, and A. A. Zdziarski, "IBIS: The Imager on-board INTEGRAL," *Astronomy & Astrophysics*, vol. 411, pp. L131–L139, Nov. 2003.

[17] A. J. Dean, D. J. Clark, J. B. Stephen, V. A. McBride, L. Bassani, A. Bazzano, A. J. Bird, A. B. Hill, S. E. Shaw, and P. Ubertini, "Polarized Gamma-Ray Emission from the Crab," *Science*, vol. 321, pp. 1183–, Aug. 2008.

[18] M. Forot, P. Laurent, I. A. Grenier, C. Gouiffès, and F. Lebrun, "Polarization of the Crab Pulsar and Nebula as Observed by the INTEGRAL/IBIS Telescope," *Astrophysical Journal Letter*, vol. 688, pp. L29–L32, Nov. 2008.

[19] P. Moran, A. Shearer, C. Gouiffes, and P. Laurent, "INTEGRAL/IBIS and optical observations of the Crab nebula/pulsar polarisation," *ArXiv e-prints*, Feb. 2013.

[20] A. Słowikowska, G. Kanbach, M. Kramer, and A. Stefanescu, "Optical polarization of the Crab pulsar: precision measurements and comparison to the radio emission," *MNRAS*, vol. 397, pp. 103–123, July 2009.

[21] S. V. Vadawale, T. Chattopadhyay, N. P. S. Mithun, A. R. Rao, D. Bhattacharya, A. Vibhute, V. B. Bhalerao, G. C. Dewangan, R. Misra, B. Paul, A. Basu, B. C. Joshi, S. Sreekumar, E. Samuel, P. Priya, P. Vinod, and S. Seetha, "Phase-resolved X-ray polarimetry of the Crab pulsar with the AstroSat CZT Imager," *Nature Astronomy*, vol. 2, pp. 50–55, Jan. 2018.

[22] W. S. Paciesas, G. N. Pendleton, J. P. Lestrade, G. J. Fishman, C. A. Meegan, R. B. Wilson, T. A. Parnell, R. A. Austin, J. Berry, Fred A., J. M. Horack, and S. D. Storey, "Performance of the large-area detectors for the Burst and Transient Source Experiment on the Gamma Ray Observatory," in *Proceedings of Society of Photo-Optical Instrumentation Engineers (SPIE) Conference Series* (C. J. Hailey and O. H. W. Siegmund, eds.), vol. 1159 of *Society of Photo-Optical Instrumentation Engineers (SPIE) Conference Series*, pp. 156–0, Nov. 1989.

[23] C. Kouveliotou, C. A. Meegan, G. J. Fishman, N. P. Bhat, M. S. Briggs, T. M. Koshut, W. S. Paciesas, and G. N. Pendleton, "Identification of Two Classes of Gamma-Ray Bursts," *Astrophysical Journal Letters*, vol. 413, p. L101, Aug. 1993.

[24] N. Gehrels, L. Piro, and P. J. T. Leonard, "The Brightest Explosions in the Universe," *Scientific American*, vol. 287, pp. 84–91, Dec. 2002.

[25] D. Eichler, M. Livio, T. Piran, and D. N. Schramm, "Nucleosynthesis, neutrino bursts and γ-rays from coalescing neutron stars," *Nature*, vol. 340, pp. 126–128, July 1989.

[26] R. Narayan, B. Paczynski, and T. Piran, "Gamma-Ray Bursts as the Death Throes of Massive Binary Stars," *Astrophysical Journal Letters*, vol. 395, p. L83, Aug. 1992.

[27] S. E. Woosley, "Gamma-Ray Bursts from Stellar Mass Accretion Disks around Black Holes," *Astrophysical Journal*, vol. 405, p. 273, Mar. 1993.

[28] K. Iwamoto, P. A. Mazzali, K. Nomoto, H. Umeda, T. Nakamura, F. Patat, I. J. Danziger, T. R. Young, T. Suzuki, T. Shigeyama, T. Augusteijn, V. Doublier, J. F. Gonzalez, H. Boehnhardt, J. Brewer, O. R. Hainaut, C. Lidman, B. Leibundgut, E. Cappellaro, M. Turatto, T. J. Galama, P. M. Vreeswijk, C. Kouveliotou, J. van Paradijs, E. Pian, E. Palazzi, and F. Frontera, "A hypernova model for the supernova associated with the γ-ray burst of 25 April 1998," *Nature*, vol. 395, pp. 672–674, Oct. 1998.

[29] A. I. MacFadyen and S. E. Woosley, "Collapsars: Gamma-Ray Bursts and Explosions in "Failed Supernovae"," *Astrophysical Journal*, vol. 524, pp. 262–289, Oct. 1999.

[30] T. Piran, "The physics of gamma-ray bursts," *Reviews of Modern Physics*, vol. 76, pp. 1143–1210, Oct. 2004.

[31] P. Mészáros, "Gamma-ray bursts," *Reports on Progress in Physics*, vol. 69, pp. 2259–2321, Aug. 2006.

[32] N. Gehrels, G. Chincarini, P. Giommi, K. O. Mason, J. A. Nousek, A. A. Wells, N. E. White, S. D. Barthelmy, D. N. Burrows, L. R. Cominsky, K. C. Hurley, F. E. Marshall, P. Mészáros, P. W. A. Roming, L. Angelini, L. M. Barbier, T. Belloni, S. Campana, P. A. Caraveo, M. M. Chester, O. Citterio, T. L. Cline, M. S. Cropper, J. R. Cummings, A. J. Dean, E. D. Feigelson, E. E. Fenimore, D. A. Frail, A. S. Fruchter, G. P. Garmire, K. Gendreau, G. Ghisellini, J. Greiner, J. E. Hill, S. D. Hunsberger, H. A. Krimm, S. R. Kulkarni, P. Kumar, F. Lebrun, N. M. Lloyd-Ronning, C. B. Markwardt, B. J. Mattson, R. F. Mushotzky, J. P. Norris, J. Osborne, B. Paczynski, D. M. Palmer, H.-S. Park, A. M. Parsons, J. Paul, M. J. Rees, C. S. Reynolds, J. E. Rhoads, T. P. Sasseen, B. E. Schaefer, A. T. Short, A. P. Smale, I. A. Smith, L. Stella, G. Tagliaferri, T. Takahashi, M. Tashiro, L. K. Townsley, J. Tueller, M. J. L. Turner, M. Vietri, W. Voges, M. J. Ward, R. Willingale, F. M. Zerbi, and W. W. Zhang, "The Swift Gamma-Ray Burst Mission," *Astrophysical Journal*, vol. 611, pp. 1005–1020, Aug. 2004.

[33] S. D. Barthelmy, L. M. Barbier, J. R. Cummings, E. E. Fenimore, N. Gehrels, D. Hullinger, H. A. Krimm, C. B. Markwardt, D. M. Palmer, A. Parsons, G. Sato, M. Suzuki, T. Takahashi, M. Tashiro, and J. Tueller, "The Burst Alert Telescope (BAT) on the SWIFT Midex Mission," *Space Science Reviews*, vol. 120, pp. 143–164, Oct. 2005.

[34] C. Meegan, G. Lichti, P. N. Bhat, E. Bissaldi, M. S. Briggs, V. Connaughton, R. Diehl, G. Fishman, J. Greiner, A. S. Hoover, A. J. van der Horst, A. von Kienlin, R. M. Kippen, C. Kouveliotou, S. McBreen, W. S. Paciesas, R. Preece, H. Steinle, M. S. Wallace, R. B. Wilson, and C. Wilson-Hodge, "The Fermi Gamma-ray Burst Monitor," *Astrophysical Journal*, vol. 702, pp. 791–804, Sept. 2009.

[35] P. Kumar and B. Zhang, "The physics of gamma-ray bursts relativistic jets," *Physics Reports*, vol. 561, pp. 1–109, Feb. 2015.

[36] J. Hakkila and R. D. Preece, "Gamma-Ray Burst Pulse Shapes: Evidence for Embedded Shock Signatures?," *Astrophysical Journal*, vol. 783, p. 88, Mar. 2014.

[37] R. Basak, S. Iyyani, V. Chand, T. Chattopadhyay, D. Bhattacharya, A. R. Rao, and S. V. Vadawale, "Surprise in simplicity: an unusual spectral evolution of a single pulse grb???151006a," *Monthly Notices of the Royal Astronomical Society*, vol. 472, no. 1, pp. 891–903, 2017.

[38] M. J. Rees and P. Meszaros, "Unsteady outflow models for cosmological gamma-ray bursts," *Astrophysical Journal Letters*, vol. 430, pp. L93–L96, Aug. 1994.

[39] R. Sari, T. Piran, and R. Narayan, "Spectra and Light Curves of Gamma-Ray Burst Afterglows," *Astrophysical Journal Letters*, vol. 497, pp. L17–L20, Apr. 1998.

[40] G. Ghisellini and A. Celotti, "Quasi-thermal Comptonization and Gamma-Ray Bursts," *Astrophysical Journal Letters*, vol. 511, pp. L93–L96, Feb. 1999.

[41] G. Ghisellini, D. Lazzati, A. Celotti, and M. J. Rees, "Compton dragged gamma-ray bursts: the spectrum," *MNRAS*, vol. 316, pp. L45–L49, Aug. 2000.

[42] D. Lazzati, E. Rossi, G. Ghisellini, and M. J. Rees, "Compton drag as a mechanism for very high linear polarization in gamma-ray bursts," *MNRAS*, vol. 347, pp. L1–L5, Jan. 2004.

[43] F. Ryde, "The Cooling Behavior of Thermal Pulses in Gamma-Ray Bursts," *Astrophysical Journal*, vol. 614, pp. 827–846, Oct. 2004.

[44] A. Pe'er and F. Ryde, "A Theory of Multicolor Blackbody Emission from Relativistically Expanding Plasmas," *Astrophysical Journal*, vol. 732, p. 49, May 2011.

[45] R. Basak and A. R. Rao, "Thermal Emissions Spanning the Prompt and the Afterglow Phases of the Ultra-long GRB 130925A," *Astrophysical Journal*, vol. 807, p. 34, July 2015.

[46] S. Iyyani, F. Ryde, B. Ahlgren, J. M. Burgess, J. Larsson, A. Pe'er, C. Lundman, M. Axelsson, and S. McGlynn, "Extremely narrow spectrum of GRB110920A: further evidence for localized, subphotospheric dissipation," *MNRAS*, vol. 450, pp. 1651–1663, June 2015.

[47] K. Toma, T. Sakamoto, B. Zhang, J. E. Hill, M. L. McConnell, P. F. Bloser, R. Yamazaki, K. Ioka, and T. Nakamura, "Statistical Properties of Gamma-Ray Burst Polarization," *Astrophysical Journal*, vol. 698, pp. 1042–1053, June 2009.

[48] S. Covino and D. Gotz, "Polarization of prompt and afterglow emission of Gamma-Ray Bursts," *Astronomical and Astrophysical Transactions*, vol. 29, pp. 205–244, 2016.

[49] M. L. McConnell, "High Energy Polarimetry of Prompt GRB Emission," *ArXiv e-prints*, Nov. 2016.

[50] M. Weisskopf, "An Overview of X-Ray Polarimetry of Astronomical Sources," *Galaxies*, vol. 6, p. 33, Mar 2018.

[51] H. Krawczynski, A. Garson, Q. Guo, M. G. Baring, P. Ghosh, M. Beilicke, and K. Lee, "Scientific prospects for hard X-ray polarimetry," *Astroparticle Physics*, vol. 34, pp. 550–567, Feb. 2011.

[52] Q. Guo, M. Beilicke, A. Garson, F. Kislat, D. Fleming, and H. Krawczynski, "Optimization of the design of the hard X-ray polarimeter X-Calibur," *Astroparticle Physics*, vol. 41, pp. 63–72, Jan. 2013.

[53] T. Kamae, V. Andersson, M. Arimoto, M. Axelsson, C. Marini Bettolo, C.-I. Björnsson, G. Bogaert, P. Carlson, W. Craig, and T. Ekeberg, "PoGOLite A high

sensitivity balloon-borne soft gamma-ray polarimeter," *Astroparticle Physics*, vol. 30, pp. 72–84, Sep 2008.

[54] M. Friis, M. Kiss, V. Mikhalev, M. Pearce, and H. Takahashi, "The PoGO+ Ballon-Borne Hard X-ray Polarimetry Mission," *Galaxies*, vol. 6, p. 30, Mar 2018.

[55] E. Jourdain, J. P. Roques, M. Chauvin, and D. J. Clark, "Separation of Two Contributions to the High Energy Emission of Cygnus X-1: Polarization Measurements with INTEGRAL SPI," *Astrophysical Journal*, vol. 761, p. 27, Dec. 2012.

[56] M. C. Weisskopf, B. Ramsey, S. O'Dell, A. Tennant, R. Elsner, P. Soffitta, R. Bellazzini, E. Costa, J. Kolodziejczak, and V. Kaspi, "The Imaging X-ray Polarimetry Explorer (IXPE)," in *Space Telescopes and Instrumentation 2016: Ultraviolet to Gamma Ray*, vol. 9905 of *Society of Photo-Optical Instrumentation Engineers (SPIE) Conference Series*, p. 990517, Jul 2016.

[57] S. V. Vadawale, B. Paul, J. Pendharkar, and S. Naik, "Comparative study of different scattering geometries for the proposed Indian X-ray polarization measurement experiment using Geant4," *Nuclear Instruments and Methods in Physics Research A*, vol. 618, pp. 182–189, June 2010.

[58] C. Maitra and B. Paul, "Prospect of polarization measurements from black hole binaries in their thermal state with a scattering polarimeter," *MNRAS*, vol. 414, pp. 2618–2628, Jul 2011.

[59] S. L. O'Dell, L. Baldini, R. Bellazzini, E. Costa, R. F. Elsner, V. M. Kaspi, J. J. Kolodziejczak, L. Latronico, H. L. Marshall, G. Matt, F. Mulieri, B. D. Ramsey, R. W. Romani, P. Soffitta, A. F. Tennant, M. C. Weisskopf, D. Z. Allen, F. Amici, S. Antoniak, P. Attina, M. Bachetti, M. Barbanera, W. H. Baumgartner, J. Bladt, S. D. Bongiorno, F. Borotto, T. Brooks, S. Bussinger, H. K. Bygott,

E. Cavazzuti, M. Ceccanti, S. Citraro, W. D. Deininger, E. Del Monte, K. L. Dietz, N. Di Lalla, G. Di Persio, I. Donnarumma, J. Erickson, Y. Evangelista, S. Fabiani, R. Ferrazzoli, M. Foster, M. Giusti, S. Gunji, L. Guy, S. Johnson, W. Kalinowski, A. R. Kelley, K. Kilaru, C. Lefevre, S. Maldera, A. Manfreda, M. Marengo, J. Masciarelli, M. McEachen, P. Mereu, M. Minuti, M. A. Mitchell, S. Mitchell, I. Mitsuishi, A. Morbidini, F. Mosti, H. Nasimi, B. Negri, L. Orsini, D. Osborne, S. D. Pavelitz, C. Pentz, M. Perri, M. Pesce-Rollins, C. Peterson, R. Piazzolla, S. Pieraccini, M. Pilia, M. Pinchera, S. Puccetti, J. Ranganathan, T. Read, A. Rubini, F. Santoli, P. Sarra, S. Schindhelm, A. Sciortino, C. Seckar, C. Sgrò, B. T. Smith, C. O. Speegle, T. Tamagawa, M. Tardiola, A. Tobia, A. Tortosa, A. Trois, B. Weddendorf, J. Wedmore, and D. Zanetti, "The Imaging X-ray Polarimetry Explorer (IXPE): technical overview," in *Proceedings of Society of Photo-Optical Instrumentation Engineers (SPIE) Conference Series*, vol. 10699 of *Society of Photo-Optical Instrumentation Engineers (SPIE) Conference Series*, p. 106991X, Aug 2018.

[60] T. Chattopadhyay, S. V. Vadawale, and J. Pendharkar, "Compton polarimeter as a focal plane detector for hard X-ray telescope: sensitivity estimation with Geant4 simulations," *Experimental Astronomy*, vol. 35, pp. 391–412, Apr. 2013.

[61] V. Bhalerao, D. Bhattacharya, A. Vibhute, P. Pawar, A. R. Rao, M. K. Hingar, R. Khanna, A. P. K. Kutty, J. P. Malkar, M. H. Patil, Y. K. Arora, S. Sinha, P. Priya, E. Samuel, S. Sreekumar, P. Vinod, N. P. S. Mithun, S. V. Vadawale, N. Vagshette, K. H. Navalgund, K. S. Sarma, R. Pandiyan, S. Seetha, and K. Subbarao, "The Cadmium Zinc Telluride Imager on AstroSat," *Journal of Astrophysics and Astronomy*, vol. 38, p. 31, June 2017.

[62] T. Chattopadhyay, S. Vadawale, S. Goyal, M. P. S., A. Patel, R. Shukla, T. Ladiya, M. Shanmugam, V. Patel, and G. Ubale, "Development of a hard x-ray focal plane compton polarimeter: a compact polarimetric configuration

with scintillators and si photomultipliers," *Experimental Astronomy*, pp. 1–18, 2015.

[63] R. P. Lin, B. R. Dennis, G. J. Hurford, D. M. Smith, A. Zehnder, P. R. Harvey, D. W. Curtis, D. Pankow, P. Turin, M. Bester, A. Csillaghy, M. Lewis, N. Madden, H. F. van Beek, M. Appleby, T. Raudorf, J. McTiernan, R. Ramaty, E. Schmahl, R. Schwartz, S. Krucker, R. Abiad, T. Quinn, P. Berg, M. Hashii, R. Sterling, R. Jackson, R. Pratt, R. D. Campbell, D. Malone, D. Landis, C. P. Barrington-Leigh, S. Slassi-Sennou, C. Cork, D. Clark, D. Amato, L. Orwig, R. Boyle, I. S. Banks, K. Shirey, A. K. Tolbert, D. Zarro, F. Snow, K. Thomsen, R. Henneck, A. McHedlishvili, P. Ming, M. Fivian, J. Jordan, R. Wanner, J. Crubb, J. Preble, M. Matranga, A. Benz, H. Hudson, R. C. Canfield, G. D. Holman, C. Crannell, T. Kosugi, A. G. Emslie, N. Vilmer, J. C. Brown, C. Johns-Krull, M. Aschwanden, T. Metcalf, and A. Conway, "The Reuven Ramaty High-Energy Solar Spectroscopic Imager (RHESSI)," *Solar Physics*, vol. 210, pp. 3–32, Nov. 2002.

[64] G. Vedrenne, J. P. Roques, V. Schönfelder, P. Mand rou, G. G. Lichti, A. von Kienlin, B. Cordier, S. Schanne, J. Knödlseder, G. Skinner, P. Jean, F. Sanchez, P. Caraveo, B. Teegarden, P. von Ballmoos, L. Bouchet, P. Paul, J. Matteson, S. Boggs, C. Wunderer, P. Leleux, G. Weidenspointner, P. Durouchoux, R. Diehl, A. Strong, M. Cassé, M. A. Clair, and Y. André, "SPI: The spectrometer aboard INTEGRAL," *Astronomy and Astrophysics*, vol. 411, pp. L63–L70, Nov. 2003.

[65] S. V. Vadawale, T. Chattopadhyay, A. R. Rao, D. Bhattacharya, V. B. Bhalerao, N. Vagshette, P. Pawar, and S. Sreekumar, "Hard X-ray polarimetry with Astrosat-CZTI," *Astronomy & Astrophysics*, vol. 578, June 2015.

[66] T. Chattopadhyay, S. V. Vadawale, A. R. Rao, S. Sreekumar, and D. Bhattacharya, "Prospects of hard X-ray polarimetry with Astrosat-CZTI," *Experimental Astronomy*, vol. 37, pp. 555–577, Nov. 2014.

[67] A. R. Rao, V. Chand, M. K. Hingar, S. Iyyani, R. Khanna, A. P. K. Kutty, J. P. Malkar, D. Paul, V. B. Bhalerao, D. Bhattacharya, G. C. Dewangan, P. Pawar, A. M. Vibhute, T. Chattopadhyay, N. P. S. Mithun, S. V. Vadawale, N. Vagshette, R. Basak, P. Pradeep, E. Samuel, S. Sreekumar, P. Vinod, K. H. Navalgund, R. Pandiyan, K. S. Sarma, S. Seetha, and K. Subbarao, "AstroSat CZT Imager Observations of GRB 151006A: Timing, Spectroscopy, and Polarization Study," *ApJ*, vol. 833, p. 86, Dec. 2016.

[68] S. Agostinelli, J. Allison, K. Amako, J. Apostolakis, H. Araujo, P. Arce, M. Asai, D. Axen, S. Banerjee, G. Barrand, F. Behner, L. Bellagamba, J. Boudreau, L. Broglia, A. Brunengo, H. Burkhardt, S. Chauvie, J. Chuma, R. Chytracek, G. Cooperman, G. Cosmo, P. Degtyarenko, A. Dell'Acqua, G. Depaola, D. Dietrich, R. Enami, A. Feliciello, C. Ferguson, H. Fesefeldt, G. Folger, F. Foppiano, A. Forti, S. Garelli, S. Giani, R. Giannitrapani, D. Gibin, J. J. Gómez Cadenas, I. González, G. Gracia Abril, G. Greeniaus, W. Greiner, V. Grichine, A. Grossheim, S. Guatelli, P. Gumplinger, R. Hamatsu, K. Hashimoto, H. Hasui, A. Heikkinen, A. Howard, V. Ivanchenko, A. Johnson, F. W. Jones, J. Kallenbach, N. Kanaya, M. Kawabata, Y. Kawabata, M. Kawaguti, S. Kelner, P. Kent, A. Kimura, T. Kodama, R. Kokoulin, M. Kossov, H. Kurashige, E. Lamanna, T. Lampén, V. Lara, V. Lefebure, F. Lei, M. Liendl, W. Lockman, F. Longo, S. Magni, M. Maire, E. Medernach, K. Minamimoto, P. Mora de Freitas, Y. Morita, K. Murakami, M. Nagamatu, R. Nartallo, P. Nieminen, T. Nishimura, K. Ohtsubo, M. Okamura, S. O'Neale, Y. Oohata, K. Paech, J. Perl, A. Pfeiffer, M. G. Pia, F. Ranjard, A. Rybin, S. Sadilov, E. Di Salvo, G. Santin, T. Sasaki, N. Savvas, Y. Sawada, S. Scherer, S. Sei, V. Sirotenko, D. Smith, N. Starkov, H. Stoecker, J. Sulkimo, M. Takahata, S. Tanaka, E. Tcherniaev, E. Safai Tehrani, M. Tropeano, P. Truscott, H. Uno, L. Urban, P. Urban, M. Verderi, A. Walkden, W. Wander, H. Weber, J. P. Wellisch, T. Wenaus, D. C. Williams, D. Wright, T. Yamada, H. Yoshida, D. Zschiesche, and G EANT4 Col-

laboration, "GEANT−4, a simulation toolkit," *Nuclear Instruments and Methods in Physics Research A*, vol. 506, pp. 250–303, 2003.

[69] S. Ganesh, K. S. Baliyan, S. Chandra, U. C. Joshi, A. Kalyaan, and S. N. Mathur, "Automated telescope for variability studies," in *Astronomical Society of India Conference Series*, vol. 9 of *Astronomical Society of India Conference Series*, 2013.

[70] B. Anandarao, E. H. Richardson, A. Chakraborty, and H. Epps, "A wide-field near-infrared camera and spectrograph for the Mt. Abu 1.2 m telescope," in *Ground-based and Airborne Instrumentation for Astronomy II*, vol. 7014 of *Society of Photo-Optical Instrumentation Engineers (SPIE) Conference Series*, p. 70142Y, July 2008.

[71] M. Chauvin, H. G. Florén, M. Friis, M. Jackson, T. Kamae, J. Kataoka, T. Kawano, M. Kiss, V. Mikhalev, T. Mizuno, N. Ohashi, T. Stana, H. Tajima, H. Takahashi, N. Uchida, and M. Pearce, "Shedding new light on the Crab with polarized X-rays," *Scientific Reports*, vol. 7, p. 7816, Aug. 2017.

[72] M. Chauvin, J. P. Roques, D. J. Clark, and E. Jourdain, "Polarimetry in the Hard X-Ray Domain with INTEGRAL SPI," *Astrophysical Journal*, vol. 769, p. 137, June 2013.

[73] E. Jourdain and J. P. Roques, "2003-2018 Monitoring of the Crab Nebula Polarization in Hard X-Rays with INTEGRAL SPI," *Astrophysical Journal*, vol. 882, p. 129, Sept. 2019.

[74] H. Feng, H. Li, X. Long, R. Bellazzini, E. Costa, Q. Wu, J. Huang, W. Jiang, M. Minuti, W. Wang, R. Xu, D. Yang, L. Baldini, S. Citraro, H. Nasimi, P. Soffitta, F. Muleri, A. Jung, J. o. Yu, G. Jin, M. Zeng, P. An, A. r. Brez, L. Latronico, C. Sgro, G. Spandre, and M. Pinchera, "Re-detection and a possible time

variation of soft X-ray polarization from the Crab," *Nature Astronomy*, vol. 4, pp. 511–516, May 2020.

[75] D. Maier, C. Tenzer, and A. Santangelo, "Point and Interval Estimation on the Degree and the Angle of Polarization: A Bayesian Approach," *PASP*, vol. 126, p. 459, May 2014.

[76] M. Chauvin, H. G. Florén, M. Friis, M. Jackson, T. Kamae, J. Kataoka, T. Kawano, M. Kiss, V. Mikhalev, T. Mizuno, H. Tajima, H. Takahashi, N. Uchida, and M. Pearce, "The PoGO+ view on Crab off-pulse hard X-ray polarization," *MNRAS*, vol. 477, pp. L45–L49, June 2018.

[77] R. Mignani, A. Shearer, A. Słowikowska, and S. Zane, *Astronomical Polarisation from the Infrared to Gamma Rays*, vol. 460. 2019.

[78] C. Lundman, I. Vurm, and A. M. Beloborodov, "Polarization of Gamma-Ray Bursts in the Dissipative Photosphere Model," *Astrophysical Journal*, vol. 856, p. 145, Apr 2018.

[79] M. L. McConnell, J. M. Ryan, D. M. Smith, R. P. Lin, and A. G. Emslie, "RHESSI as a Hard X-Ray Polarimeter," *Solar Physics*, vol. 210, pp. 125–142, Nov. 2002.

[80] R. E. Rutledge and D. B. Fox, "Re-analysis of polarization in the γ-ray flux of GRB 021206," *MNRAS*, vol. 350, pp. 1288–1300, June 2004.

[81] C. Wigger, W. Hajdas, K. Arzner, M. Güdel, and A. Zehnder, "Gamma-Ray Burst Polarization: Limits from RHESSI Measurements," *Astrophysical Journal*, vol. 613, pp. 1088–1100, Oct. 2004.

[82] E. Kalemci and J. L. Matteson, "Investigation of charge sharing among electrode strips for a CdZnTe detector," *Nuclear Instruments and Methods in Physics Research A*, vol. 478, pp. 527–537, Feb. 2002.

[83] S. McGlynn, D. J. Clark, A. J. Dean, L. Hanlon, S. McBreen, D. R. Willis, B. McBreen, A. J. Bird, and S. Foley, “Polarisation studies of the prompt gamma-ray emission from GRB 041219a using the spectrometer aboard INTEGRAL,” *Astronomy & Astrophysics*, vol. 466, pp. 895–904, May 2007.

[84] S. McGlynn, S. Foley, B. McBreen, L. Hanlon, S. McBreen, D. J. Clark, A. J. Dean, A. Martin-Carrillo, and R. O’Connor, “High energy emission and polarisation limits for the INTEGRAL burst GRB 061122,” *Astronomy & Astrophysics*, vol. 499, pp. 465–472, May 2009.

[85] D. Götz, P. Laurent, F. Lebrun, F. Daigne, and Ž. Bošnjak, “Variable Polarization Measured in the Prompt Emission of GRB 041219A Using IBIS on Board INTEGRAL,” *Astrophysical Journal Letter*, vol. 695, pp. L208–L212, Apr. 2009.

[86] D. Götz, S. Covino, A. Fernández-Soto, P. Laurent, and Ž. Bošnjak, “The polarized gamma-ray burst GRB 061122,” *MNRAS*, vol. 431, pp. 3550–3556, June 2013.

[87] D. Götz, P. Laurent, S. Antier, S. Covino, P. D’Avanzo, V. D’Elia, and A. Melandri, “GRB 140206A: the most distant polarized gamma-ray burst,” *MNRAS*, vol. 444, pp. 2776–2782, Nov 2014.

[88] D. Yonetoku, T. Murakami, S. Gunji, T. Mihara, K. Toma, T. Sakashita, Y. Morihara, T. Takahashi, N. Toukairin, H. Fujimoto, Y. Kodama, S. Kubo, and IKAROS Demonstration Team, “Detection of Gamma-Ray Polarization in Prompt Emission of GRB 100826A,” *Astrophysical Journal Letter*, vol. 743, p. L30, Dec. 2011.

[89] D. Yonetoku, T. Murakami, S. Gunji, T. Mihara, K. Toma, Y. Morihara, T. Takahashi, Y. Wakashima, H. Yonemochi, T. Sakashita, N. Toukairin, H. Fujimoto, and Y. Kodama, “Magnetic Structures in Gamma-Ray Burst Jets Probed by

Gamma-Ray Polarization," *Astrophysical Journal Letter*, vol. 758, p. L1, Oct. 2012.

[90] S. Orsi and Polar Collaboration, "POLAR: A Space-borne X-Ray Polarimeter for Transient Sources," *Astrophysics and Space Sciences Transactions*, vol. 7, pp. 43–47, Feb. 2011.

[91] S.-N. Zhang, M. Kole, T.-W. Bao, T. Batsch, T. Bernasconi, F. Cadoux, J.-Y. Chai, Z.-G. Dai, Y.-W. Dong, and N. Gauvin, "Detailed polarization measurements of the prompt emission of five gamma-ray bursts," *Nature Astronomy*, vol. 3, pp. 258–264, Jan 2019.

[92] C. M. Poole, I. Cornelius, J. V. Trapp, and C. M. Langton, "A CAD Interface for GEANT4," *ArXiv e-prints*, May 2011.

[93] W. Coburn and S. E. Boggs, "Polarization of the prompt γ-ray emission from the γ-ray burst of 6 December 2002," *Nature*, vol. 423, pp. 415–417, May 2003.

[94] S. McGlynn, D. J. Clark, A. J. Dean, L. Hanlon, S. McBreen, D. R. Willis, B. McBreen, A. J. Bird, and S. Foley, "Polarisation studies of the prompt gamma-ray emission from GRB 041219a using the spectrometer aboard INTEGRAL," *Astronomy & Astrophysics*, vol. 466, pp. 895–904, May 2007.

[95] E. Kalemci, S. E. Boggs, C. Kouveliotou, M. Finger, and M. G. Baring, "Search for Polarization from the Prompt Gamma-Ray Emission of GRB 041219a with SPI on INTEGRAL," *Astrophysical Journals*, vol. 169, pp. 75–82, Mar. 2007.

[96] D. R. Willis, E. J. Barlow, A. J. Bird, D. J. Clark, A. J. Dean, M. L. McConnell, L. Moran, S. E. Shaw, and V. Sguera, "Evidence of polarisation in the prompt gamma-ray emission from GRB 930131 and GRB 960924," *Astronomy & Astrophysics*, vol. 439, pp. 245–253, Aug 2005.

[97] V. Chand, T. Chattopadhyay, S. Iyyani, R. Basak, E. Aarthy, A. R. Rao, S. V. Vadawale, D. Bhattacharya, and V. B. Bhalerao, "Violation of Synchrotron Line

of Death by the Highly Polarized GRB 160802A," *Astrophysical Journal*, vol. 862, p. 154, Aug 2018.

[98] V. Chand, T. Chattopadhyay, G. Oganesyan, A. R. Rao, S. V. Vadawale, D. Bhattacharya, V. B. Bhalerao, and K. Misra, "AstroSat-CZTI Detection of Variable Prompt Emission Polarization in GRB 171010A," *Astrophyscial Journal*, vol. 874, p. 70, Mar 2019.

[99] "CZTI GRB monitor page." `http://astrosat.iucaa.in/czti/?q=grb`.

[100] F. Muleri, "On the Operation of X-Ray Polarimeters with a Large Field of View," *Astrophysical Journal*, vol. 782, p. 28, Feb 2014.

[101] T. Chattopadhyay, S. V. Vadawale, E. Aarthy, N. P. S. Mithun, V. Chand, A. Ratheesh, R. Basak, A. R. Rao, V. Bhalerao, S. Mate, B. Arvind, V. Sharma, and D. Bhattacharya, "Prompt Emission Polarimetry of Gamma-Ray Bursts with the AstroSat CZT Imager," *Astrophysical Journal*, vol. 884, p. 123, Oct 2019.

[102] V. Sharma, S. Iyyani, D. Bhattacharya, T. Chattopadhyay, A. R. Rao, E. Aarthy, S. V. Vadawale, N. P. S. Mithun, V. B. Bhalerao, F. Ryde, and A. Pe'er, "Time-varying Polarized Gamma-Rays from GRB 160821A: Evidence for Ordered Magnetic Fields," *Astrophysical Journal Letters*, vol. 882, p. L10, Sep 2019.

[103] C. M. Poole, I. Cornelius, J. V. Trapp, and L. C. M, "A CAD Interface for GEANT4," *Australasian Physical and Engineering Science in Medicine*, Sep 2012.

[104] U. Klaas, T. G. Muller, R. J. Laureijs, J. Clavel, J. S. V. Lagerros, R. J. Tuffs, A. Moneti, E. Kreysa, and W. Kratschmer, "Polarization measurements with ISOPHOT: performance and first results," in *The Universe as Seen by ISO* (P. Cox and M. Kessler, eds.), vol. 427 of *ESA Special Publication*, p. 77, Mar. 1999.

[105] S. Trippe, "[Review] Polarization and Polarimetry," *Journal of Korean Astronomical Society*, vol. 47, pp. 15–39, Feb. 2014.

[106] D. P. Clemens, A. F. Pinnick, M. D. Pavel, and B. W. Taylor, "The Galactic Plane Infrared Polarization Survey (GPIPS)," *Astrophysical Journal*, vol. 200, p. 19, June 2012.

[107] D. C. Hines, C. C. Packham, A. Adamson, B.-G. Andersson, R. Antonucci, D. Axon, J. de Buizer, A. Cellino, D. Clemens, J. L. Hoffman, M. Kishimot, T. J. Jones, A. Lazarian, A. M. Megalhaes, J. Masiero, E. S. Perlman, M. Perrin, C. V. Rodrigues, H. Shinnaga, and W. W. Sparks, Doug, "O/IR Polarimetry for the 2010 Decade (CGT): Science at the Edge, Sharp Tools for All," in *astro2010: The Astronomy and Astrophysics Decadal Survey*, vol. 2010 of *ArXiv Astrophysics e-prints*, 2009.

[108] P. G. Martin, "Some implications of 10-micron interstellar polarization," *Astrophysical Journal*, vol. 202, pp. 393–399, Dec. 1975.

[109] R. Kandori, N. Kusakabe, M. Tamura, Y. Nakajima, T. Nagayama, C. Nagashima, J. Hashimoto, J. Hough, S. Sato, T. Nagata, A. Ishihara, P. Lucas, and M. Fukagawa, "SIRPOL: a JHK $_s$-simultaneous imaging polarimeter for the IRSF 1.4-m telescope," in *Society of Photo-Optical Instrumentation Engineers (SPIE) Conference Series*, vol. 6269 of *Society of Photo-Optical Instrumentation Engineers (SPIE) Conference Series*, p. 626951, June 2006.

[110] D. P. Clemens, D. Sarcia, A. Grabau, E. V. Tollestrup, M. W. Buie, E. Dunham, and B. Taylor, "Mimir: A Near-Infrared Wide-Field Imager, Spectrometer and Polarimeter," *Publications of the astronomical society of the pacific*, vol. 119, pp. 1385–1402, Dec. 2007.

[111] A. B. Schultz, M. Sosey, L. M. Mazzuca, H. A. Bushouse, M. Dickinson, T. Boeker, D. Calzetti, S. Arribas, L. E. Bergeron, W. Freudling, S. T. Holfeltz,

S. Malhotra, B. Mobasher, K. Noll, E. Roye, and C. Xu, "Post-NCS Performance of the HST NICMOS," in *IR Space Telescopes and Instruments* (J. C. Mather, ed.), vol. 4850 of *Society of Photo-Optical Instrumentation Engineers (SPIE) Conference Series*, pp. 858–866, Mar. 2003.

[112] T. J. Jones and C. C. Packham, "MMTPol, A High Precision Imaging Polarimeter for the MMT," in *American Astronomical Society Meeting Abstracts*, vol. 39 of *Bulletin of the American Astronomical Society*, p. 748, Dec. 2007.

[113] S. Wolf, L. Vanzi, and N. Ageorges, "Technical report on the polarimetric mode of SOFI." `https://www.eso.org/sci/facilities/lasilla/instruments/sofi/doc/manual/sofiman_1.6.pdf`, Aug. 2002. [Online; accessed 18-Oct-2018].

[114] R. Devaraj, A. Luna, L. Carrasco, M. A. Vázquez-Rodríguez, Y. D. Mayya, J. G. Tánori, and E. O. Serrano Bernal, "POLICAN: A Near-infrared Imaging Polarimeter at the 2.1m OAGH Telescope," *Publications of the astronomical society of the pacific*, vol. 130, p. 055002, May 2018.

[115] M. Watanabe, H. Nakaya, T. Yamamuro, T. Zenno, M. Ishii, M. Okada, A. Yamazaki, Y. Yamanaka, M. Kurita, M. Kino, R. Ijiri, T. Hirao, T. Nagata, S. Sato, T. Kawai, Y. Nakamura, T. Sato, N. Ebizuka, J. H. Hough, and A. Chrysostomou, "TRISPEC: A Simultaneous Optical and Near-Infrared Imager, Spectrograph, and Polarimeter," *Publications of the astronomical society of the pacific*, vol. 117, pp. 870–884, Aug. 2005.

[116] J.-L. Beuzit, "SPHERE: a Planet Finder Instrument for the VLT," *European Planetary Science Congress*, vol. 8, pp. EPSC2013–954, Sept. 2013.

[117] H. Akitaya, Y. Moritani, T. Ui, T. Urano, Y. Ohashi, K. S. Kawabata, A. Nakashima, M. Sasada, K. Sakimoto, T. Harao, H. Miyamoto, R. Matsui, R. Itoh, K. Takaki, I. Ueno, T. Ohsugi, H. Nakaya, T. Yamashita, and M. Yoshida, "HONIR: an optical and near-infrared simultaneous imager, spectrograph, and

polarimeter for the 1.5-m Kanata telescope," in *Ground-based and Airborne Instrumentation for Astronomy V*, vol. 9147 of *Society of Photo-Optical Instrumentation Engineers (SPIE) Conference Series*, p. 91474O, Aug. 2014.

[118] "Wollastron Polarizing Prisms." `https://www.newport.com/f/wollaston-polarizing-prisms`.

[119] E. Oliva, "Wedged double Wollaston, a device for single shot polarimetric measurements." `http://citeseerx.ist.psu.edu/viewdoc/download?doi=10.1.1.868.880&rep=rep1&type=pdf`, Oct. 1996.

[120] "Wire Grid Polarizers." `https://www.nilt.com/files/pdf/app_note_wire_grid_polarizers.pdf`, June 2009.

[121] "Thorlabs." `https://www.thorlabs.com/newgrouppage9.cfm?objectgroup_id=5510`.

[122] G. G. Stokes, "On the Composition and Resolution of Streams of Polarized Light from different Sources," *Transactions of the Cambridge Philosophical Society*, vol. 9, p. 399, 1851.

[123] S. Chandrasekhar, *Radiative transfer.* 1960.

[124] J. E. Frecker and K. Serkowski, "Linear polarimeter with rapid modulation, achromatic in the 0.3-1.1-micron range," *Applied Optics*, vol. 15, p. 605, Mar. 1976.

[125] D. C. B. Whittet, P. G. Martin, J. H. Hough, M. F. Rouse, J. A. Bailey, and D. J. Axon, "Systematic variations in the wavelength dependence of interstellar linear polarization," *Astrophysical Journal*, vol. 386, pp. 562–577, Feb. 1992.

[126] K. Serkowski, "Polarimeters for Optical Astronomy," in *IAU Colloq. 23: Planets, Stars, and Nebulae: Studied with Photopolarimetry* (T. Gehrels, ed.), p. 135, 1974.

[127] D. A. Turnshek, R. C. Bohlin, R. L. Williamson, II, O. L. Lupie, J. Koornneef, and D. H. Morgan, "An atlas of Hubble Space Telescope photometric, spectrophotometric, and polarimetric calibration objects," *Astrophysical Journal*, vol. 99, pp. 1243–1261, Apr. 1990.

[128] D. C. B. Whittet, P. A. Gerakines, J. H. Hough, and S. S. Shenoy, "Interstellar Extinction and Polarization in the Taurus Dark Clouds: The Optical Properties of Dust near the Diffuse/Dense Cloud Interface," *Astrophysical Journal*, vol. 547, pp. 872–884, Feb. 2001.

[129] A. Schulz and R. Lenzen, "New polarization measurements of HD 183143, HD 204827, and CYG OB 2 Sch. No. 12," *AAP*, vol. 121, pp. 158–161, May 1983.

[130] A. U. Landolt, "UBVRI photometric standard stars in the magnitude range 11.5-16.0 around the celestial equator," *Astronomical Journal*, vol. 104, pp. 340–371, July 1992.